Ph. D. DISSERTATION

A Study on the Physical Properties of Carbon-doped Silicon Oxide Low-*k* Thin Films with Nano-pore Structure for ULSI Interconnect Application

DEPARTMENT OF PHYSICS

GRADUATE SCHOOL
CHEJU NATIONAL UNIVERSITY

Kyoung-Suk Oh

December 2005

ULSI 적용을 위한 나노 기공 구조를 지닌 Carbon-Doped Silicon Oxide 저유전 박막의 물리적 특성 연구

吳 景 淑

(指導敎授 催 致 圭)

이 論文을 理學 博士學位 論文으로 提出함

2005年 12月

吳景淑의 理學博士 論文을 認准함

審査委員長 ________________

委　　　員 ________________

委　　　員 ________________

委　　　員 ________________

委　　　員 ________________

濟州大學校 大學院

2005년 12월

A Study on the Physical Properties of Carbon-doped Silicon Oxide Low-*k* Thin Films with Nano-pore Structure for ULSI Interconnect Application

Kyoung-Suk Oh

(Supervised by Profession Chy Kyu Choi)

A thesis submitted in partial fulfillment of the requirement for the degree of doctor of science

2005. 12.

This thesis has been examined and approved.

제주대학교 중앙도서관
JEJU NATIONAL UNIVERSITY LIBRARY

____

____

____

____

____

____

Date

Department of Physics

GRADUATE SCHOOL

CHEJU NATIONAL UNIVERSITY

Table of Contents

List of Tables ······ iv
List of Figures ······ vi
Abstract ······ xiv

Ⅰ. Introduction ······ 1
Ⅱ. Overview of the Low Dielectric Materials ······ 5
1. Background of Interconnection ······ 6
1) Interconnection ······ 6
2) RC Delay ······ 8
3) Cross-Talk ······ 13
4) Power Dissipation ······ 16
2. Requirements for Interlayer Dielectric Films ······ 16
3. Various Low-k Dielectric Materials ······ 20
1) Organic Polymers Materials ······ 21
2) Porous Materials ······ 24
3) Critical Issues with Porous Dielectrics ······ 27

Ⅲ. Theory ······ 29
1. Dielectric Materials ······ 29

제주대학교 중앙도서관
JEJU NATIONAL UNIVERSITY LIBRARY

1) Capacitance and Relative Permittivity ········· 29
2) Polarization Phenomena ········· 31
3) Film Density and Relative Permittivity ········· 34
4) Relative Permittivity and Frequency ········· 35
5) Dielectric Constant ········· 37
2. Analysis of Mechanical Properties ········· 42
3. Time of Flight-Elastic Recoil Detection (TOF-ERD) Analysis ········· 49
4. Bruggeman's Effective Medium ········· 53
5. Carrier Transport in Insulating Films ········· 56

Ⅳ. Experiments and Analysis ········· 59
1. Formation of the SiOC(-H) Films ········· 59
2. Analysis of the Bonding Structure on SiOC(-H) Films ········· 61
3. XPS Analysis ········· 62
4. Measurements of TOF-ERD ········· 62
5. Measurements of Pore Distribution ········· 63
6. Nano-indentation Experiments ········· 64
7. I-V and C-V Measurements ········· 64
8. The Surface Morphology and Roughness ········· 65
9. TEM Images ········· 65
10. Measurements of Film Thickness ········· 66

제주대학교 중앙도서관
JEJU NATIONAL UNIVERSITY LIBRARY

Ⅴ. Results and Discussion ······ 67
1. Chemical Properties ······ 67
1) Bonding Structure of SiOC(-H) Films ······ 67
2) Binding Energy of SiOC(-H) Films ······ 97
2. Nano-pore Structure ······ 108
1) The Pore Size and the Size Distribution ······ 108
2) GISAXS Analysis ······ 114
3) XRR Analysis ······ 120
4) Porosity of the SiOC(-H) Films ······ 125
5) Film Density and Composition ······ 128
6) TEM Images ······ 147
3. Mechanical and Electrical Properties ······ 149
1) Mechanical Hardness and Elastic Modulus ······ 149
2) Current-voltage (I-V) Characteristics ······ 153
4. Dielectric Properties ······ 160

Ⅵ. Conclusion ······ 176

References ······ 181
List of related publications ······ 188
Abstract (Korean) ······ 201
Acknowledgement (Korean) ······ 204

제주대학교 중앙도서관
JEJU NATIONAL UNIVERSITY LIBRARY

List of Tables

Table 1. Property requirements for low-*k* dielectrics. 19

Table 2. Micro-processor unit interconnect technology requirements. 20

Table 3. Comparison of Low-k Materials. 22

Table 4. Basic conduction processes in insulators. 58

Table 5. Experimental condition 61

Table 6. Pore size and size distribution 118

Table 7. The critical angle and the average electron density for SiOC(-H) films of as-deposited, annealed samples at 200, 300 and 400 ℃ with a flow rate ratio of 85 %. 124

Table 8. The critical angle and the average electron density for the SiOC(-H) films annealed at 400 ℃ deposited with flow rate ratios of 45 to 85 %. 124

Table 9. The porosity and dielectric constant of SiOC(-H) composite films, as-deposited and annealed at 200, 300 and 400 ℃ with various BTMSM/(O_2+BTMSM) flow rate ratios. 126

Table 10. The density (g/cm^3) of as-deposited and annealed SiOC(-H) films at 200, 300 and 400 ℃ with BTMSM/(O_2+BTMSM) flow rate ratios. 146

Table 11. Mechanical properties of Low-k films 153

Table 12. The dipole moment of the Si-O-C chain structure and the bonding angle between Si-O and Si-C bonds. 161

Table 13. The dielectric constant arise from electronic, ionic, dipolar and total component of SiOC(-H) films as a function of the BTMSM/(O_2+BTMSM) flow rate ratios from 45 to 85 %. 175

List of Figures

Fig. 1. Cross-sectional SEM picture of 10-level Cu dual-Damascene structure fabricated using SiLK™ at the lower level (minimum feature size from M1 to M4) of multilevel interconnects. ·········· 7

Fig. 2. Simple crossed metal lines with dielectrics. ································· 9

Fig. 3. Components of parasitic capacitance versus feature size. ············ 11

Fig. 4. Dependence of signal delay on device size. Decrease in interconnect delay and improved performance are achieved using copper and low-k dielectrics. ··· 12

Fig. 5. Decrease in interconnect delay and improved performance are achieved using copper and low-k dielectrics. ································· 14

Fig. 6. Microprocessor clock speed for different metals and dielectrics as a function of feature size. ·· 15

Fig. 7. Typical chip cross-section illustrating hierarchical scaling of Cu damascene. ·· 18

Fig. 8. Schematic cross section of two capacitor plates with surface charge density and a dielectric polarized by an electric field E. Each circle denotes a polarization moment. ································· 30

Fig. 9. Frequency dependence of the several factors contributing to polarizability. ·· 40

Fig. 10. An indentation load-displacement curve in which several important parameters used in the Oliver and Pharr analysis are illustrated. ·· 43

제주대학교 중앙도서관
JEJU NATIONAL UNIVERSITY LIBRARY

Fig. 11. Illustration of the indentation geometry at maximum load for an ideal conical indenter. ········· 47
Fig. 12. Interaction of ion-beam and material. ········· 50
Fig. 13. Schematic diagram of ERD-TOF analysis system. ········· 51
Fig. 14. Schematic diagram of two particles before and after collision. ··· 51
Fig. 15. Bruggeman's effective medium approximation showing dielectric constant versus porosity for oxide and a low-k material. ········· 55
Fig. 16. Schematic diagram of ICP-CVD system. ········· 60
Fig. 17. FTIR spectra of SiOC(-H) films prepared with various BTMSM/(O_2+BTMSM) flow rate ratios. ········· 69
Fig. 18. FTIR spectra of SiOC(-H) films prepared with various BTMSM/(O_2+BTMSM) flow rate ratios for annealed films at 200 ℃ for 30 min. ········· 71
Fig. 19. FTIR spectra of SiOC(-H) films prepared with various BTMSM/(O_2+BTMSM) flow rate ratios for annealed films at 300 ℃ for 30 min. ········· 72
Fig. 20. FTIR spectra of SiOC(-H) films prepared with various BTMSM/(O_2+BTMSM) flow rate ratios for annealed films at 400 ℃ for 30 min. ········· 73
Fig. 21. Deconvolution of Si-O-C bonding mode in the wavenumber range 950~1250 cm^{-1} of the same sample Fig. 17. ········· 75

제주대학교 중앙도서관
JEJU NATIONAL UNIVERSITY LIBRARY

Fig. 22. Deconvolution of Si-O-C bonding mode in the wavenumber range 950~1250 cm^{-1} of the same sample Fig. 18. 76
Fig. 23. Deconvolution of Si-O-C bonding mode in the wavenumber range 950~1250 cm^{-1} of the same sample Fig. 19. 77
Fig. 24. Deconvolution of Si-O-C bonding mode in the wavenumber range 950~1250 cm^{-1} of the same sample Fig. 20. 79
Fig. 25. The peak position of Si-O-C ring link of spectrum between 950 cm^{-1} and 1250 cm^{-1} for the resulted fitted peaks as-deposited and annealed SiOC(-H) composite films at 200, 300 and 400℃ with various BTMSM/(O_2+BTMSM) flow rate ratios. 81
Fig. 26. The relative integrated absorption area (peak area/total area of spectrum between 950 and 1250 cm^{-1}) of the Si-O-C ring link for the resulted fitted peaks, as-deposited and annealed SiOC(-H) composite films at 200, 300 and 400 ℃ with various BTMSM/(O_2+BTMSM) flow rate ratios. 82
Fig. 27. The relation of the carbon concentration of as-deposited and annealed SiOC(-H) composite films at 200, 300 and 400 ℃ with various BTMSM/(O_2+BTMSM) flow rate ratios. 85
Fig. 28. The bonding angle of SiOC(-H) composite films, as-deposited and annealed at 200, 300 and 400 ℃ with various BTMSM/(O_2+BTMSM) flow rate ratios. 86

제주대학교 중앙도서관
JEJU NATIONAL UNIVERSITY LIBRARY

Fig. 29. Deconvolution of spectra in the wavenumber range 700~950 cm^{-1} of the same sample Fig. 17. ········· 88
Fig. 30. Deconvolution of spectra in the wavenumber range 700~950 cm^{-1} of the same sample Fig. 18. ········· 89
Fig. 31. Deconvolution of spectra in the wavenumber range from 700~950 cm^{-1} of the same sample Fig. 19. ········· 90
Fig. 32. Deconvolution of spectra in the wavenumber range from 700~950 cm^{-1} of the same sample Fig. 20. ········· 91
Fig. 33. Deconvolution of spectra in the wavenumber range from 2850~3050 cm^{-1} of the same sample Fig. 17. ········· 93
Fig. 34. Deconvolution of spectra in the wavenumber range 2850~3050 cm^{-1} of the same sample Fig. 18. ········· 94
Fig. 35. Deconvolution of spectra in the wavenumber range 2850~3050 cm^{-1} of the same sample Fig. 19. ········· 95
Fig. 36. Deconvolution of spectra in the wavenumber range 2850~3050 cm^{-1} of the same sample Fig. 20. ········· 96
Fig. 37. The O 1s XPS spectra of an (a) as-deposited sample and (b) annealed sample with a flow rate ratio of 85 % at 400 ℃ for 30 min in a vacuum. ········· 98
Fig. 38. The Si 2p XPS spectra of an (a) as-deposited sample and (b) annealed sample with a flow rate ratio of 85 % at 400 ℃ for 30 min in a vacuum. ········· 100

제주대학교 중앙도서관
JEJU NATIONAL UNIVERSITY LIBRARY

Fig. 39. The C 1s XPS spectra of an (a) as-deposited sample and (b) annealed sample with a flow rate ratio of 85 % at 400 ℃ for 30 min in a vacuum. ········ 102
Fig. 40. The Si 2p XPS spectra of an annealed sample with flow rate ratios of 65, 75 and 85 % at 400 ℃ for 30 min in a vacuum. ········ 106
Fig. 41. The C 1s XPS spectra of an annealed sample with flow rate ratios of 65, 75 and 85 % at 400 ℃ for 30 min in a vacuum. ········ 107
Fig. 42. Measured and fitted scattering intensities versus the scattering vector, Q, of as-deposited and annealed SiOC(-H) composite films with a BTMSM/(O_2+BTMSM) flow rate ratio of 85 %. ·· 109
Fig. 43. Distribution of pores of as-deposited and annealed SiOC(-H) composite films with a BTMSM/(O_2+BTMSM) flow rate ratio of 85 % versus pore radius as measured by using the SANS method. ········ 110
Fig. 44. Measured and fitted scattering intensities versus the scattering vector, Q, of SiOC(-H) composite films annealed at 400 ℃ with various BTMSM/(O_2+BTMSM) flow rate ratios. ········ 112
Fig. 45. Distribution of pores of SiOC(-H) composite films, annealed at 400 ℃ with various BTMSM/(O_2+BTMSM) flow rate ratios, versus pore radius as measured by using the SANS method. ··· 113

제주대학교 중앙도서관
JEJU NATIONAL UNIVERSITY LIBRARY

Fig. 46. The extracted in-plane GISAXS scattering profiles of the porous SiOC(-H) thin films with annealed at 400 ℃. ··········· 116
Fig. 47. The number distribution of pores as a function of pore radius for SiOC(-H) film with annealed at 400 ℃ deposited with a flow rate ratio of 55 %. ··········· 117
Fig. 48. The GISAXS data for the as-deposited SiOC(-H) film with a flow rate ratio of 85 %. ··········· 119
Fig. 49. The experimental reflectivity for SiOC(-H) thin films of as-deposited and annealed samples at 200, 300 and 400 ℃ with a flow rate ratio of 85 %. ··········· 122
Fig. 50. The X-ray reflectivity for SiOC(-H) films annealed at 400 ℃ deposited with various BTMSM/(O_2+BTMSM) flow rate ratios. 123
Fig. 51. The porosity of SiOC(-H) composite films, as-deposited and annealed at 200, 300 and 400 ℃ with various BTMSM/(O_2+BTMSM) flow rate ratios. ··········· 127
Fig. 52. Flight Time versus energy scatter plot of annealed SiOC(-H) film at 400 ℃ with various BTMSM/(O_2+BTMSM) flow rate ratios of (a) 45 %, (b) 55 %, (c) 65 %, (d) 75 % and (e) 85 %. ········ 130
Fig. 53. RBS spectra of SiOC(-H) annealed films at 400 ℃ with BTMSM/(O_2+BTMSM) flow rate ratios. (a) carbon, (b) oxygen, (c) hydrogen and (d) silicon ··········· 131

제주대학교 중앙도서관
JEJU NATIONAL UNIVERSITY LIBRARY

Fig. 54. Flight Time versus energy scatter plot of SiOC(-H) film with BTMSM/(O_2+BTMSM) flow rate ratio of 85 % at (a) as-deposited and annealed at (b) 200 ℃, (c) 300 ℃ and (d) 400 ℃. 136
Fig. 55. RBS spectra of SiOC(-H) annealed film at 400 ℃ with BTMSM/(O_2+BTMSM) flow rate ratio of 85 % of as-deposited and annealed films at 200, 300 and 400 ℃. (a) carbon, (b) oxygen, (c) hydrogen and (d) silicon. 137
Fig. 56. The atomic concentration of as-deposited and annealed films at 200, 300 and 400 ℃ measured by ERD-TOF with BTMSM/(O_2+BTMSM) flow rate ratio of 85 %. 133
Fig. 57. The atomic concentration of annealed films at 400℃ measured by ERD-TOF with BTMSM/(O_2+BTMSM) flow rate ratios of 45, 55, 65, 7 and 85 %. 143
Fig. 58. The density of as-deposited and annealed SiOC(-H) films at 200, 300 and 400 ℃ with various BTMSM/(O_2+BTMSM) flow rate ratios. 145
Fig. 59. The Cross-sectional TEM images of (a) as-deposited and (b) annealed SiOC(-H) Films at 400 ℃. 148
Fig. 60. Variation of the hardness (H) values of as-deposited and the annealed SiOC(-H) films as a function of BTMSM/(BTMSM+O_2) flow rate ratios. 151

제주대학교 중앙도서관
JEJU NATIONAL UNIVERSITY LIBRARY

Fig. 61. The elastic modulus (E) of as-deposited and annealed SiOC(-H) films as a function of BTMSM/(BTMSM+O_2) flow rate ratios. 152

Fig. 62. The leakage current density as a function of the electrical field strength for SiOC(-H) films of as-deposited and annealed at 100, 200, 300 and 400 ℃ with BTMSM/(O_2+ BTMSM) flow rate ratio of 85 %. 154

Fig. 63. "$\ln J$" versus electric field $\sqrt{E}$: characteristics as a function of measurement temperature with a BTMSM/(O_2+BTMSM) flow rate ratio of 45 %. 156

Fig. 64. "$\ln J$" versus electric field $\sqrt{E}$: characteristics as a function of measurement temperature for annealed films at 400 ℃ with BTMSM/(O_2+BTMSM) flow rate ratio of 45 %. 157

Fig. 65. "$\ln J$" versus electric field $\sqrt{E}$: characteristics as a function of measurement temperature with a BTMSM/(O_2+BTMSM) flow rate ratio of 85 %. 158

Fig. 66. "$\ln J$" versus electric field $\sqrt{E}$: characteristics as a function of measurement temperature for annealed films at 400 ℃ with a BTMSM/(O_2+BTMSM) flow rate ratio of 85 %. 159

Fig. 67. The dipole moment as a function of BTMSM/(O_2+BTMSM) flow rate ratio for as-deposited and annealed films at 200, 300 and 400 ℃. 162

제주대학교 중앙도서관
JEJU NATIONAL UNIVERSITY LIBRARY

Fig. 68. The function of number density to the BTMSM/(O_2+BTMSM) flow rate ratios. ········· 165
Fig. 69. The calculated the dipolar polarizability as a function of the BTMSM/(O_2+BTMSM) flow rate ratios. ········· 166
Fig. 70. The dielectric constants of as-deposited and annealed SiOC(-H) films with various BTMSM/(O_2+BTMSM) flow rate ratios. ····· 168
Fig. 71. The relationship between the refractive index with of as-deposited and annealed SiOC(-H) film the BTMSM/(O_2+BTMSM) flow rate ratios from 45 to 85 %. ········· 169
Fig. 72. Electronic dielectric constants of as-deposited and annealed SiOC(-H) films as a function of BTMSM/(O_2+BTMSM) flow rate ratios from 45 to 85 %. ········· 171
Fig. 73. Ionic dielectric constants of the SiOC(-H) films as a function of BTMSM/(O_2+BTMSM) flow rate ratios from 45 to 85 %. ·· 172
Fig. 74. Dipolar dielectric constants of the SiOC(-H) films as a function of BTMSM/(O_2+BTMSM) flow rate ratios from 45 to 85 %. ········· 173

제주대학교 중앙도서관
JEJU NATIONAL UNIVERSITY LIBRARY

Abstract

This work is focused on exploring the chemical structure of SiOC(-H) film including its dielectric constant and porosity during deposition and post-annealing procedures. Influences on electrical and mechanical properties resulting from changes in chemical structure are also examined. Different chemicals can be deposited on Low-*k* SiOC(-H) composite films by using an inductively coupled plasma chemical vapor deposition (ICPCVD) system with a bis-trimethylsilymethane (BTMSM, H_9C_3-Si-CH_2-Si-C_3H_9) precursor and oxygen gas.

Structural characteristics of SiOC(-H) films with different bonding arrangements were investigated by Fourier transform infrared (FTIR) spectroscopy. The spectra were generally broad and overlapping due to the complex stoichiometry and the amorphous nature of the films. The bonding structure of SiOC(-H) films examined were Si-CH_3 (885 cm^{-1}), Si-O-C(Si) (1046 and 1106 cm^{-1}), CH_x (1457 and 2955 cm^{-1}), and OH-related (3720 cm^{-1}) bonds. The spectra of the Si-O-Si asymmetric stretching mode were found to be clearly separated Si-O-Si and Si-O-C bonds. Some CH_n species were removed from the bulk of the film due to the annealing process, and some of the Si-O-Si bonds changed into Si-O-C bonds including ring, open and cage links in which C atoms have been incorporated. The bonding structure of SiOC(-H) films changed due to the post-annealing process and increases in the flow rate ratio, which could be transformed from an open-linked to a

제주대학교 중앙도서관
JEJU NATIONAL UNIVERSITY LIBRARY

ring-linked substructure. The bonding angle between the Si-O and the Si-C bonds increased with the flow rate ratio as well as with the annealing temperature.

The O 1s XPS spectra consisted of O-Si bond (532.6 eV) and O-C bond (530.6 eV) and after being annealed, the C-O bond intensity was a little bit higher than that of the as-deposited film. The Si 2p spectrum consisted of two peaks, which could be assigned as $Si-O_4$ bond (103.0 eV) and $C-Si-O_3$ bond (101.0 eV), for the annealed sample it consisted of three peaks as a $Si-O_4$ bond (103.1 eV), $C-Si-O_3$ bond (101.3 eV) and C_2-Si-O_2 bond (99.4 eV). The C 1s spectra consisted of C-H, C-Si and -C-O bonds. By increasing the flow rate ratio, C-Si bonds were chemically shifted towards the lower binding energy side. Such binding energy changes could be explained by the oxidation states of silicon atoms. When carbon in C-Si was replaced by O-Si-O, the binding energy of the $C-Si-O_3$ bond shifted to a higher energy state.

제주대학교 중앙도서관
JEJU NATIONAL UNIVERSITY LIBRARY

The distribution of pore diameters ranged from 1.8 to 3.5 nm, with an average measured value of 2.5±0.2 nm. The peak value in the pore diameter size distribution increased about 12 % after annealing, but the average size of the pore was almost unchanged. The porosity increased due to the increase in the relative content of the Si-O-C ring link mode, in which the carbon atoms are incorporated in the Si-O-Si bonds. The density of as-deposited SiOC(-H) films decreased from 2.42 to 1.21 g/cm^3 as the flow rate ratios increased from 45 to 85 %. The density of SiOC(-H) films annealed at 400 ℃ were calculated as 0.98 g/cm^3 for a flow rate ratio of 85 %. The decreased film density was due to the formation of voids in the film.

The hardness values of as-deposited films ranged from 2.6 to 1.6 GPa and films annealed at 400 ℃ exhibited hardness values from 2.0 to 0.7 GPa. Elastic modulus values of as-deposited films ranged from 26 to 14 GPa, with that of films annealed at 400 ℃ ranging from 20 to 7 GPa. The leakage current density at 1 MV/cm increased from 2.0×10^{-7} for as-deposited samples to 2.2×10^{-8} A/cm^2 for samples annealed at 400 ℃. The dielectric constant of as-deposited SiOC(-H) film with flow rate ratios of 45 and 85 % were found to be 2.60 and 2.30, respectively. In the case of samples annealed at 200, 300 and 400 ℃, the dielectric constant decreased gradually from 45 to 85 %. The lowest relative dielectric constant of the annealed film with a flow rate of 85 % was about 2.18. The experimental results showed that the refractive index decreased to 1.37 from 1.50 when the flow rate ratio was increased. The refractive index of annealed films also decreased from 1.40 to 1.31 when the flow rate ratio was increased.

제주대학교 중앙도서관
JEJU NATIONAL UNIVERSITY LIBRARY

From these results, we could infer that the dielectric constant of the SiOC(-H) film depended on the relative carbon contents and the porosity. The porosity increase was due to the increasing relative content of Si-O-C ring link forms, in which the CH_3 groups were incorporated in the Si-O-Si bonds. This causes nano-pores to be formed due to the aloof force between the CH_3 group and other parts of Si-O-Si bond. The porosity of SiOC(-H) films was closely related to the film density. The decrease of the dielectric constant after annealing indicated that a rearrangement of bonding structure in the film resulted in the formation or enhancement of pre-existing atomic scale nano-pores in the film.

Ⅰ. Introduction

Continuing improvement in device density and performance has significantly impacted the feature size and complexity of the wiring structure for on-chip interconnects. As the minimum device dimensions reduce beyond 70 nm, the increase in propagation delay, crosstalk noise, and power dissipation in the interconnect structure become limiting factors for ultra-large-scale integration (ULSI) of integrated circuits. Since the delay, noise, and power consumption all critically depend on the dielectric constant (k) of the separating insulator, much attention has been focused recently on replacing the standard silicon dioxide with new intermetal dielectric materials which have considerably lower dielectric constants than thermal silicon dioxide films (k=3.9~4.2) [1].

제주대학교 중앙도서관
JEJU NATIONAL UNIVERSITY LIBRARY

Many researchers have proposed a variety of organic and inorganic materials as alternatives to SiO_2 [2~6]. Thin films formed using inorganic materials have good thermal and mechanical stability, as well as better film adhesion. However, they generally have higher dielectric constants and more serious moisture absorption problems than organic materials and as a result, they require additional liner and capping layers. The hybrid-type films formed from organic and inorganic materials are promising as low-k materials with stable properties [7]. Sometimes called "organosilicate glass (OSG)" or "carbon-doped glass", SiOC film can be any one of a variety of glassy materials composed of differing organic molecules [8-11]. These materials have the chemical composition $SiO_{1-x}C_xH_y$, in which

the silicon-oxygen network seen in glass is occasionally interrupted, in a more or less homogeneous fashion, by the presence of organic, typically methyl (CH_3) groups. Hydrido (H) substitution at silicon can also be present [8, 11]. The film's lower dielectric constant is due to these changes to the SiO_2 network and the reduced density of the OSG film relative to SiO_2. In typical low-k SiOC films with nano-pore structures, 10% to 25% of the silicon atoms are substituted with organic groups. SiOC(-H) containing alkyl groups has attracted more attention for higher thermal and mechanical stability compared to many organic materials. The spatial hindrance of alkyl groups may produce abundant nano-size voids in the film and decrease the dielectric constant [5, 6]. It is generally accepted that the nano-pores in films formed by the steric hindrance effect of alkyl groups as well as the carbon's lower polarizability in Si-CH_3 groups are the main reasons for the decrease in the dielectric constant. However, the detailed bonding structure of the SiOC(-H) film with nano-pore structure resulting from deposition conditions of PECVD and post-annealing effects are not still clear. The post-thermal treatment can also change the bonding structure, which consists of the ring and open links in SiOC(-H) film with nano-pore structure. On the other hand, the bonding structure is directly related to the dielectric properties of the resulting films [4]. If one could vary the SiOC(-H) film with the nano-pore structure in a controlled way, it might be possible to control the dielectric constant. Therefore, it is critical to have methods for making SiOC(-H) films with nano-pore structure in order to understand the correlations between processing conditions and the resulting physical properties.

제주대학교 중앙도서관
JEJU NATIONAL UNIVERSITY LIBRARY

In this study, we will focus on exploring the chemical structure of SiOC(-H) films, their dielectric constants, and their porosity during hybrid type SiOC(-H) film deposition and post-annealing procedures. Influences on electrical and mechanical properties resulting from changes in chemical structure are also examined. The introduction summarizes the results contained herein in order to provide the reader with a complete overview of this work. We will establish a sufficiently thorough understanding of the background of the interconnection on Cu/Low-k chips, various low-k materials and critical issues with porous dielectrics. These issues are of fundamental importance for developing and processing SiOC(-H) films with nano-pore structure.

This thesis is organized as follows. In chapter II, an overview of low-k materials is presented (which is the background for interconnections on Cu/Low-k chips), requirements for interlayer dielectric films, and various critical issues with porous dielectrics. In chapter III, the theory of characteristic analysis of Low-k films will be reviewed. First, the quantitative relationship between the relative permittivity and properties of molecules, such as dipole moments, polarization and frequency will be described. We will distinguish among three polarizabilities that depend on the applied frequency. Second, analysis of the mechanical properties by nanoindentation procedures will be introduced. The method used in the present research is elastic modulus, which is dependent on penetration depth and also hardness. Third, the calculation of density and atomic concentration will be described by Time of flight- Elastic recoil detection analysis. Finally, the effect of porosity on

제주대학교 중앙도서관
JEJU NATIONAL UNIVERSITY LIBRARY

the dielectric constant will be explained using Bruggman's effective medium. In chapter Ⅳ, the method used in carrying out experiments and analysis will be briefly introduced, including a description of systems and conditions for the deposition of SiOC(-H) film, FTIR, XPS, ERD-TOF, nonoindentation, TEM imaging, and so on. In chapter V, characteristics of SiOC(-H) films and its chemical properties will be reported. The detailed bonding structure of SiOC(-H) films with nano-pore structure made by PECVD deposition will be investigated by using FTIR and XPS. We will check pore size and pore distribution by SANS and TEM imaging. We will then refer to electrical properties, mechanical properties, and the influence of carbon contents by thermal treatment. In chapter Ⅵ, we will show and discuss some of the results from chapter Ⅴ. In chapter Ⅶ, conclusions will be presented defining the experimental results of this work. This section will focus on exploring the chemical structure of SiOC(-H) films along with their dielectric constants and porosity during hybrid type SiOC(-H) film deposition and post-annealing procedures.

제주대학교 중앙도서관
JEJU NATIONAL UNIVERSITY LIBRARY

Ⅱ. Overview of the low dielectric materials

The interconnect structure for Cu metallization is fabricated using the damascene process where Cu is deposited into wiring channels patterned into the ILD layer and then planarized using chemical-mechanical polishing (CMP). The damascene structure introduces a new set of materials and processes distinctly different from the standard AlCu interconnect technology, which makes the the implementation of low-k dielectrics a challenging task. At this time, low-k integration is proceeding with a number of candidate materials. In spite of the intense effort, no clearly superior dielectric with k 〈 3.0 has emerged. The lack of a clear choice of low-*k* dielectric can be largely attributed to the many challenges associated with the successful integration of these materials into future on-chip interconnects. In addition to low dielectric constant, candidate intr- and interlevel dielectrics must satisfy a large number of diverse requirements in order to be successfully integrated. The requirements include high thermal and mechanical stability, good adhesion to the other interconnect materials, resistance to processing chemicals, low moisture absorption, and low cost. In recent years there have been widespread efforts to develop low-k materials that can simultaneously satisfy all of these requirements. A particularly difficult challenge for materials development has been to obtain the combination of low dielectric constant and good thermal and mechanical stability.

제주대학교 중앙도서관
JEJU NATIONAL UNIVERSITY LIBRARY

1. Background of Interconnection

1) Interconnection of Cu/Low-k Chip

The number of interconnect line, which is required to transform the arrays of electronic devices into meaningful circuit is too large to accommodate all lines in a single layer. For present 256 MB DRAM chip, up to four levels of interconnect lines (metallization levels) are necessary [12]. For the 1 GB DRAM chips, this will not change much, but the next generation of logic chips up to eight metallization levels will probably be necessary. The bridging metal lines have to be constructed with surface deposition/etching techniques, which require level, uniform surface. Therefore, the space between the lines of one level must be filled with an electrically insulating material, which can serve as the basis for the bridges in the next higher level. In Fig. 1 10-level interconnects for a 90 nm-generation device is shown [13], which were fabricated using a layers between the interconnects are made of production worthy single-Damascene process. The dielectric SiLK^{TM} (M1-M4), SiOC (M5-M8), and SiO_2 (M9-M10). For the next generation down to 70 nm, porous materials having a k below 2.5 must be used in order to achieve wiring capacitances below 180 fF/mm [14].

In these interconnections, the continuous improvement of the performance of a device is limited mostly by two factors, the gate delay and the interconnect delay (mostly RC delay). Gate delay was the dominant reason for the performance of a device a decade ago. As the dimensions continuous to scale down, the interconnect delay becomes larger. The gate delay is less as the gate length is shorter. However

제주대학교 중앙도서관
JEJU NATIONAL UNIVERSITY LIBRARY

Fig. 1. Cross-sectional SEM picture of 10-level Cu dual-Damascene structure fabricated using SiLK^{TM} at the lower level (minimum feature size from M1 to M4) of multilevel interconnects.

the interconnect delay is worse as the dimension scales down. Not the exact number but the trend is more important because the dimension of different levels of a multilevel interconnect are different. The resistance of metal line increases as the line width decreases and the capacitance increases as metal lines are closer. Eventually the RC delay will dominate as the dimension is getting smaller and smaller. The solution for the resistance is copper metalization. The solution for capacitance is the low k dielectrics. The integration of low k dielectric between metal lines can also reduce the cross-talk noise level, which is critical for future interconnects [15].

2) RC delay

제주대학교 중앙도서관
JEJU NATIONAL UNIVERSITY LIBRARY

As the distance between the interconnect lines decreases, the lines start to influence each other, when voltage and current are applied to the unit cell as shown Fig. 2. Inductive and capacitive effects increase. Because a line to line capacitance C_{LL} increases as the scale length decreases, and vertical layer to layer capacitance C_{LG} decreases as the scale length decreases, but total capacitance increase. Therefore, a reduction in line to line capacitance is one of the most critical issues for manufacturing high density devices. Along with the decrease in the metal pitch, both interconnect wiring resistance and capacitance increase, which leads to higher interconnect resistance capacitance (RC) delay time from Eq. (1-1). The RC delay can be written as [15]

$$R = \frac{2\rho L}{PT}$$

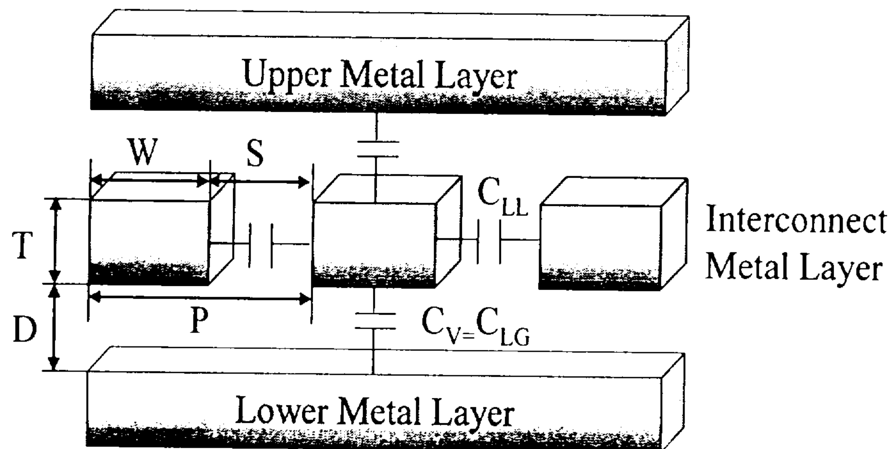

P = W + S ; W = S ; T = D ,
W : metal width
S : space between metals
T : metal thickness
D : dielectric thickness Assuming

P : metal pitch
C_{LL} : lateral line-to-line capacitance
C_V : vertical layer-to-layer capacitance
C_{LG} : line-to-ground capacitance
$C_V = C_{LG}$

Fig. 2. Simple crossed metal lines with dielectrics.

제주대학교 중앙도서관
JEJU NATIONAL UNIVERSITY LIBRARY

$$C = 2C(C_{LL} + C_V) = 2k\epsilon_o\left(\frac{2LT}{P} + \frac{LP}{2T}\right) \quad (1\text{-}1)$$

$$RC = 2\rho k\epsilon_o\left(\frac{4L^2}{P} + \frac{L^2}{T^2}\right)$$

where ρ is the resistivity of the metal line, *k* is the dielectric constant of dielectrics, ϵ_o is the permittivity of vacuum, L is the total length of metal line, P is metal pitch, and T is metal thickness, respectively. From Eq. (1-1), the RC delay will be increased to be proportional to $(1-P)^2$ as the metal pitch decreases. And also, a change of the electrical current in one line induces a current in the neighboring line through a change of the electrical field. Hence, inductive cross-talk decreases the reliability of data transport. In addition, two neighboring lines at different voltage form a capacitor, when they are close enough to reach other. Thus, below a certain distance of the interconnecting lines, the signal delay is no longer dominated by the intrinsic gate delay of the transistor, but by capacitive resistance of the interconnect array. The components of parasitic capacitance and the gate delay time are illustrated in Figs. 3 and 4 [12]. Replacing aluminum (Al: resistivity ~2.66 ㎛-cm) by copper (Cu: resistivity ~1.67 ㎛-cm) is an approach to reduce the resistances of metal lines by 38%. Reducing capacitances among metal lines (intermetallic dielectric: IMD or interlayer dielectric: ILD) needs the use of low dielectric constant (low-*k* : relative dielectric constant *k* < 3.0) and/or ultra low-*k* (*k* < 2.4) materials as IMD (or ILD) materials. As a result, for the metal line and dielectrics we should substitute Cu and low-*k* (or ultra low-*k*) for Al and SiO_2 (*k*=4.0) to overcome the obstacle of the device performance [13].

제주대학교 중앙도서관

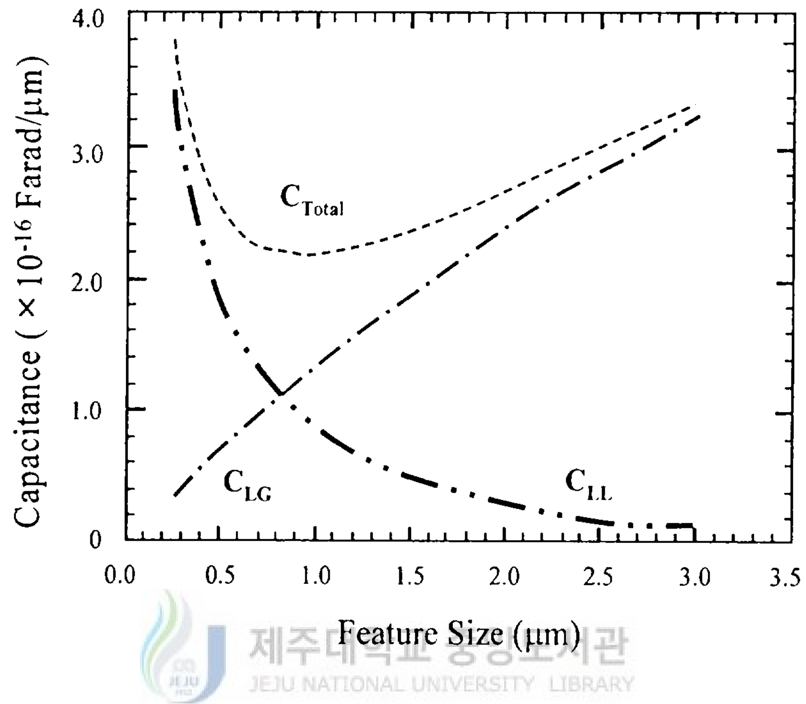

제주대학교 중앙도서관
JEJU NATIONAL UNIVERSITY LIBRARY

Fig. 3. Components of parasitic capacitance versus feature size.

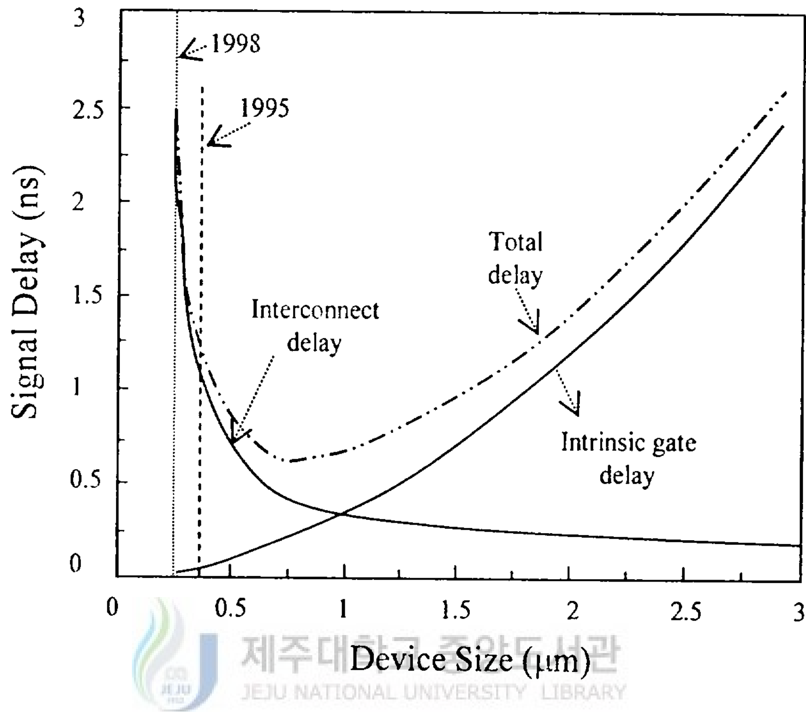

제주대학교 중앙도서관
JEJU NATIONAL UNIVERSITY LIBRARY

Fig. 4. Dependence of signal delay on device size.

3) Cross-talk

Signal cross-talk (C_L/C_T) of DRAM device is given by the ratio of line-to-line (sidewall) capacitance to total capacitance; power dissipation in interconnects is proportional to total capacitance, as is RC delay. Thus, it is important to simultaneously co-optimize the sidewall and the total capacitance to ensure that the best overall system performance is achieved. As transistor operating voltage continues to scale downward, interconnect cross-talk becomes increasingly important and noise levels must be reduced to avoid spurious transistor turn-on. Silicon cross-talk is dominated by interconnect sidewall capacitance (as is overall capacitance for minimum feature size as shown in Fig. 3), process-related solutions such as the use of thinner metallization and/or low-*k* dielectrics must be explored [12]. The interconnect scaling scenario shown in Fig. 5 illustrates how sidewall capacitance can be mitigated in cross-talk as conductor spacing decreases. However, for this approach resistance and current density in the wire increase with the square of the scaling factor, so that RC delay and Joule heating increase, the latter raising reliability concerns. It is obvious that for this scaling approach to be effective in improving the RC delay and cross-talk, a lower resistivity and higher reliability metal is needed; insertion of a lower permittivity (low-*k*) dielectric offers additional performance improvement. The introduction of copper metalization served as an enabler for aggressive interconnect scaling due to its lower resistivity (1.8 $\mu\Omega$cm) as compared with traditional AlCu metalization (~3.3 $\mu\Omega$cm) as well as improved reliability. Thus, for a fixed resistance per unit length, thinner metal could be used for copper versus aluminum wiring and sidewall capacitance could be reduced.

제주대학교 중앙도서관
JEJU NATIONAL UNIVERSITY LIBRARY

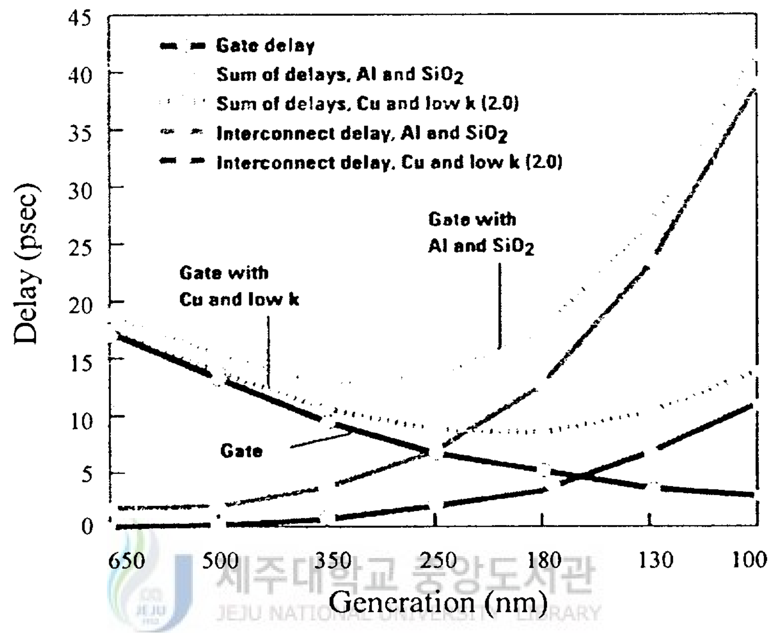

Fig. 5. Decrease in interconnect delay and improved performance are achieved using copper and low-k dielectrics [16].

제주대학교 중앙도서관
JEJU NATIONAL UNIVERSITY LIBRARY

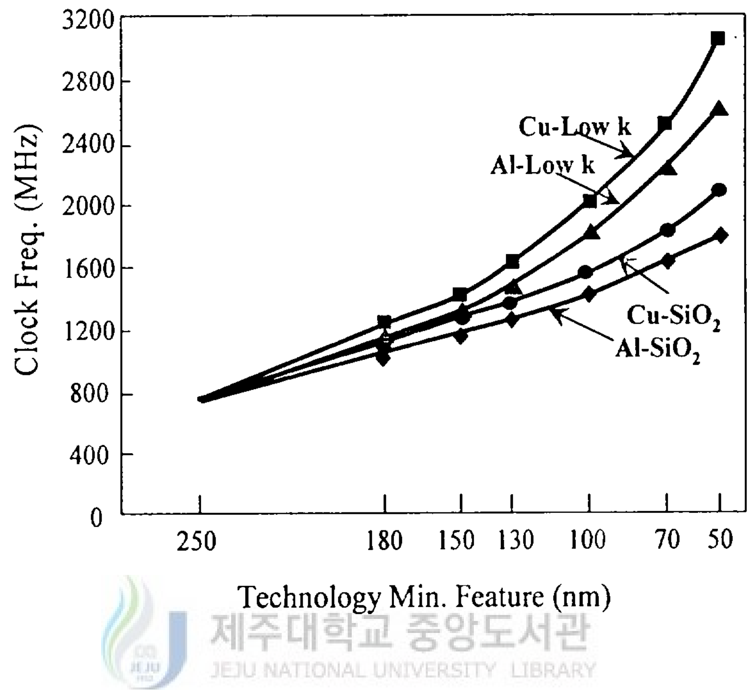

제주대학교 중앙도서관
JEJU NATIONAL UNIVERSITY LIBRARY

Fig. 6. Microprocessor clock speed for different metals and dielectrics as a function of feature size.

Later introduction of low-*k* dielectric relieved sidewall capacitance and provided more latitude in the optimization of RC, power, and cross-talk versus metal thickness and spacing [17].

4) Power dissipation

Power dissipation should be reduced in order to achieve excellent performance for mobile devices. Power dissipation of CMOS circuit is defined by $p = CV^2 f$, where p is power, C is circuit capacitance, f is operating frequency, and V is operating voltage. While there are circuit layout techniques to minimize the interconnect power dissipation with respect to frequency [18].

2. Requirements for interlayer dielectric films

The basic properties to be evaluated for interlayer dielectric films are : ⅰ) electrical properties, ⅱ) chemical and physical properties, and ⅲ) thermal properties. Leakage current, breakdown strength and dielectric loss as well as dielectric constant, are important for the electrical properties. Refractive index, chemical bonding structure/composition, residual stress, density, shrinkage at heat treatment, water absorbance, etching rate, impurities and step coverage/planarity (in case of damascene structure, step coverage is less important) are important for the chemical/physical properties evaluation.

As for the thermal properties, thermal stress variation at heat-treatment cycles, thermogravimetric analysis, thermomechanical properties, and residual gas analysis are the major criteria. The List of properties that must be possessed by such dielectric layer is given in Table 1 [12, 19-21]. In the evaluations, the relationships among these properties and mechanism analysis should be considered [18].

Typical microprocessor design utilize a hierarchical or "reverse scaling" metallization scheme (see Fig. 7) where widely spaced "fat wires" are used on upper global interconnect and power levels to minimize RC delay and voltage drop. Maintaining power distribution at constant voltage through equipotential wires to all bias points requires increasingly lower resistance global wires as operating voltage continues to scale and switching frequencies increase. This need is being partially addressed by the introduction of ball-grid-array packaging technology that distributes individual power feeds across the chip, eliminating much of the need for lateral power distribution across chip. New packaging technologies will undoubtedly play an equally important role in alleviating power dissipation and system performance bottlenecks [13, 18].

In order to meet future performance needs, the International Technology Roadmap for Semiconductors (ITRS) 2004 Update Edition [22] suggested the concrete values such as the dielectric constant, the resistivity of Cu, and so on with the technology node (Table 2). Of particular note is a need for increased current handling capability, lower permittivity dielectrics, and a reduction in metal barrier thickness. These changes, while extremely challenging, are to a certain extent

제주대학교 중앙도서관
JEJU NATIONAL UNIVERSITY LIBRARY

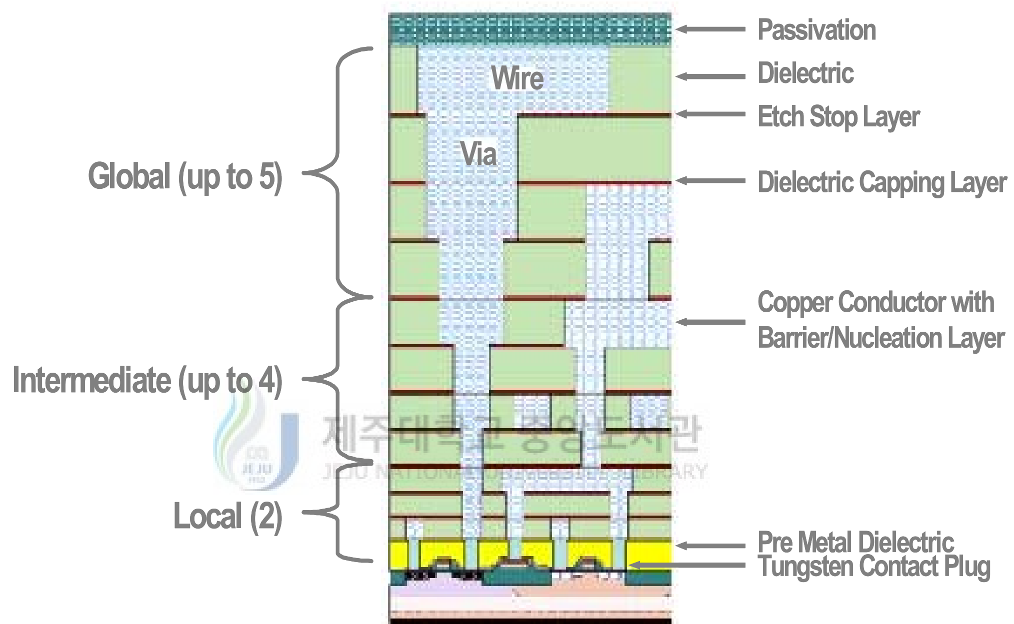

제주대학교 중앙도서관
JEJU NATIONAL UNIVERSITY LIBRARY

Fig. 7. Typical chip cross-section illustrating hierarchical scaling of Cu damascene.

Table 1. Property requirements for low-k dielectrics.

Property		Value	Unit
Electrical	Low-k	< 3 (preferably<2.5)	
	Low dielectric loss		
	Low dissipation at 1 MHz	< 0.005	
	Low leakage current	$< 10^{-9}$	A/cm^2
	Dielectric breakdown	> 1	MV/cm
	Low charge trapping		
	High electric-field strength		
	High reliability		
Chemical	Chemical resistance		
	Etch rate	> 3	nm/s
	Etch selectivity	Oxygen plasma resistance	
	Low moisture absorption	< 1	%
	Low solubility in H_2O		
	Low gas permeability		
	High purity		
	No metal corrosion		
	Long storage life	6	Month
	Environmentally safe		
Mechanical	Thickness uniformity within wafer	< 10	%
	Planarization	> 80	%
	Step coverage	> 80	%
	Good adhesion (to metal, self-adhesion)	Pass tape test after thermal cycles to 450 ℃	
	Gap-fill	No voids at 0.35 ㎛, aspect ratio=2	
	Number of particle > 0.3 ㎛	< 0.08	cm^{-2}
	Low shrinkage		
	Crack resistance		
	Low stress	< ±100	MPa
	Tensile strength	> 200	MPa
	High hardness	> 0.1	GPa
	High tensile modulus	> 1	GPa
	CMP compatibility		
Thermal	High thermal stability	> 425	℃
	Low coefficient of thermal expansion	< 50	ppm
	Low thermal shrinkage	< 2.5	%
	Low thermal weight loss at 450℃, 8h	< 10	%wt
	Glass transition temp. Tg	> 400	℃
	High thermal conductivity	> 0.1	W/mk

제주대학교 중앙도서관
JEJU NATIONAL UNIVERSITY LIBRARY

Table 2. Micro-processor unit (MPU) interconnect technology requirements.

Year of production	2003	2004	2005	2006	2007	2010	2013	2016
Technology node(nm) (DRAM 1/2 pitch)	100	90	80	70	65	45	32	22
Number of metal levels	9	10	11	11	11	12	12	14
Barrier thickness(nm)	12	10	9	8	7	5	3.5	2.5
Interlevel metal insulator bulk dielectric constant	< 3.0	< 2.7	< 2.7	< 2.7	< 2.4	< 2.1	< 1.9	< 1.7
Interlevel metal insulator effective dielectric constant	3.3-3.6	3.1-3.6	3.1-3.6	3.1-3.6	2.7-3.0	2.3-2.6	2.0-2.4	< 2.0

□ Manufacturable exit, and are being optimize

■ Manufacturable solution are NOT known

■ Manufacturable solution are known

evolutionary since traditional wiring technology will be employed. However, recent simulations [23] predict that in spite of these material changes the performance roadmap will not be met. Revolutionary approaches are needed to meet the performance challenge, and several new candidate interconnect technologies all needed [17].

제주대학교 중앙도서관
JEJU NATIONAL UNIVERSITY LIBRARY

3. Various low-k materials

Silicon dioxide (SiO_2) has been the most widely used dielectric material in the semiconductor industry. It has good thermal and mechanical properties, but too high a dielectric constant (3.9~4.5) for the future generation of IC's.

Initial attempts to decrease the dielectric constant of SiO_2 involved the incorporation of fluorine or carbon to the oxide films, and also the use of spin-on glasses or silsesquioxanes, which are similar in nature to SiO_2, but with lower dielectric constants due to the non-bridging silicon-carbon bonds in the backbone. The Si-C bonds lower the density of the films by introducing free volume, and also exhibit lower polarizability with respect to the Si-O bonds in silicon dioxide. Over the years, a wide variety of materials have been tested for low dielectric constant applications and Table 3 summarizes some of these, along with their respective k values and deposition method [14, 24, 25]. The most promising among these materials are the organic polymers and the porous materials because of their lower dielectric constant. However, as stated previously, the ideal thin film dielectric material not only needs to have a low dielectric constant, but also a series of electrical, mechanical, and thermal properties required for its application into microelectronic devices.

제주대학교 중앙도서관
JEJU NATIONAL UNIVERSITY LIBRARY

1) Organic polymers materials

The failure to meet one or several of these requirements has limited the use of some materials, such as Teflon AF (DuPont). This amorphous copolymer of tetrafluoriethylene and 2,2-bis(trifluoromethyl)-4,5- difluorodi -oxide has a very low dielectric constant (k=2.1), but lacks thermo-mechanical stability as it has low glass transition (T_g<300 ℃) and decomposition temperatures (~360 ℃) [26, 27]. It also shows poor adhesion to metals.

Table 3. Comparison of Low-k Materials.

Deposition methode	Type of materials		Dielectric constant	Company
CVD	Inorganic	Air gap	< 2.0	
		BN	2.6~3.0	
		SiOB	3.1~3.5	
		SiOF	3.1~3.5	
		Fluorinated SiO_2	2.8~3.9	
	Organic	SiCOH	2.05	IBM
		Coral	< 2.4	Novellus
		Orion	2.2	Trikon
		Palylene-F	2.1~2.5	
		a-C:F	2.1~2.5	
		Palylene-N	2.6~3.0	
		Black Diamond	2.6~3.0	Applied materials
		Black Diamond Ⅲ	< 2.4	Applied materials
		Flow Fill	2.6~3.0	Trikon
		Coral	2.6~3.0	Novellus systems
Spin on	Inorganic SOG	Nanoglass E	2.2	Honeywell
		Nanoglass	2.6~3.0	AlliedSignal
		HPS	2.6~3.0	CCIC
		NCS	2.6~3.0	CCIC
		T-22	2.6~3.0	AlliedSignal
		FOX	2.6~3.0	Daw corning
		Type-12	2.6~3.0	TOK
	Organic SOG	ST-F2000	2.1~2.5	Hitachi Chemical
		HSG-R7	2.6~3.0	Hitachi Chemical
		Type-9	2.6~3.0	TOK
		T-18	2.6~3.0	AlliedSignal
		HOSP	2.6~3.0	AlliedSignal
	Organic	Speed Film	< 2.0	Gore
		p-SiLK	2.1	Daw chemical
		XLK	2.2	Daw corning
		Cytop	2.1~2.5	Asahi Glass
		Nautilus	2.1~2.5	Daw chemical
		ELK-FLARE	2.1~2.5	AlliedSignal
		SiLK	2.65	Daw chemical
		FLARE	2.6~3.0	AlliedSignal
		Cyclotene	2.6~3.0	Daw chemical
		Velox	2.6~3.0	Schumacher
		Alcap	2.6~3.0	Asahi Chamical
		PQ-600	2.6~3.0	Hitachi Chemical
		PQ-100	2.6~3.0	Hitachi Chemical

제주대학교 중앙도서관
JEJU NATIONAL UNIVERSITY LIBRARY

Other organic polymers like the polymides [25, 28] tend to have low dielectric constants in the range of 2.9~3.5, good thermomechanical properties, and planarizing capabilites. However, some types of polymides have high moisture absorption (which raises the dielectric constant), and are extremely anisotropic with high in-plane dielectric constants. Fluorinated polyimides have lower dielectric constant, higher T_g and improved moisture resistance over the nonfluorinated ones, but they show poor adhesion and outgassing of fluorine wpecies is possible at elevated temperatures. Benzocylcobutenes (Dow Chemical) [25, 28] are themosetting polymers that have good spin-on planarization characteristic and low moisture absorption (<0.2 wt% at 85 % relative humidity). Their low dielectric constant (*k*~2.6) is the result of a chemical structure that combines relatively non-polarizable aliphatic rings with aromatic rings. However, the main disadvantage with these materials is a limited thermal stability when exposed to temperatures of 150~300 ℃ in the presence of air, and a high coefficient of thermal expansion (CTE=52 ppm/℃) [29]. They decompose at temperatures above 350 ℃.

Polyarylene ethers [30, 31] are another type of organic polymers being considered for low-k applications. FLARE™ (Honeywell) is the commercial name for one of such polymers, and one of its formulations has shown a dielectric constant with as low a value as 2.38. This dielectric constant is isotropic and stable during thermal cycling to 450 ℃. The material exhibits comparable thermal stability to polymides, but with lower moisture absorption. It also shows good mechanical stability and solvent resistance, but major

제주대학교 중앙도서관
JEJU NATIONAL UNIVERSITY LIBRARY

concerns include adhesion and outgassing of fluorine species during subsequent processing, which can compromise the dielectric constant.

Among the most recent materials being rested for integration into IC manufaturing are SiLK (Dow Chemical) and Black Diamond (Applied Materials). SiLK is an aromatized and cross-linked polyphenylene spin-on material with a dielectric constant of 2.65, and thermal stability in excess of 450 ℃ [32]. It also has good adhesion to typical metals and barrier layers used in microelectronic processing, and a high T_g (>490 ℃). Continuing effort by IBM have demonstrated successful integration of SiLK into copper-based chips [33], making this the first report of an organic dielectric material used in IC fabrication. On the other hand, Black Diamond is a plasma enhanced a plasma enhanced chemical vapor deposited material with the nature of carbon-dopes silicon dioxide. It has a dielectric constant of 2.7, good thermal stability, and can withstand the stresses applied during CMP processing without delaminating from the substrate [30, 34]. However, etching the material without leaving residues on the sidewalls has presented some difficulties for its application.

Increasing attention has focused on the use of porous materials as interlevel dielectrics because no fully-densified material cam compare to the ultra low-k values obtained when air (porosity) is added to the films.

2) Porous materials

The feasibility of the porous dielectrics approach was originally

제주대학교 중앙도서관
JEJU NATIONAL UNIVERSITY LIBRARY

demonstrated with porous silica. These materials consisted of a silicon dioxide network with a high fraction of small pores with diameters in the nanometer range [35]. The typical preparation procedure for porous silica involves spin-coating a precursor (e. g. tetraethoxysilane) in a solvent onto the substrate, followed by gelation of the silica network under controlled conditions of temperature, pH and catalyst (acid/base) concentration [36, 37]. After the gelation process, subsequent aging drying and annealing steps are necessary to move the remaining solvent and the water produced is required because the large amounts of liquid that need to be removed can lead to shrinkage and can cause high internal stress levels and cracking in the films. Porous silica has been subdivided into two classes depending on the preparation procedure and the resultant porosity. Aerogels are the materials with the highest porosity (up to 98 %), attained only by supercritical drying under high pressure. The xerogels, on the other hand, show a significantly lower degree of porosity (50~90 %), but are prepared using conventional solvents under moderate conditions [38]. The dielectric constant of these films has been measured in the range of 1.1~2.5 depending on the degree of porosity. Nanoglass (Honewell) is the commercial name of a spin-on nanoporous silica product, and it has a dielectric constant of 2.0 with a porosity of 70 % [39].

Aerogels and xrogels (porous silica) offer advantages over other dielectric materials that induced high thermal stability, and lower dielectric constant due to variable porosity. However, the use of porous silica in microelectronic applications has been limited due to difficulties in obtaining homogeneous and

제주대학교 중앙도서관
JEJU NATIONAL UNIVERSITY LIBRARY

reproducible pore microstructures, and also because of high moisture absorption and low mechanical strength consideration [35, 40]. Jin et al. [35] and Cho et al. [41] have reported on chemical modification techniques used to reduce the surface hydroxyl (OH) groups, and therefore, the moisture uptake of the porous silica films.

A more recently developed porous material is Dow Cornig XLK dielectric material [42, 43]. These films are deposited via a spin on process, and the chemical formulation contains hydrogen silsesquioxane (HSQ) resin, a high boiling point solvent, and a low boiling point solvent. The preparation procedure includes a gelation reaction in the presence of the high boiling point solvent, and low boiling point solvent. The gelation process involves a controlled exposure to a wet ammonia treatment. Therefore, analogous to the previous porous silica films, the XLK films also require a complex preparation procedure. The cured films have a dielectric constant of 2.19, and a prosity of 59.5 % that is completely interconnected through the film (as determined from small angle neutron scattering). One of the major difficulties with these films is moving the solvents without collapsing the HSQ resin structure in the process.

In a similar study, A. Gill et al. [44] developed a SiOCH films using a tetramethlylcyclotetrasiloxane (TMCTS) organic materials by PECVD methode The cured films have a dielectric constant of 2.05, and a porosity of 29 % that is completely interconnected through the film. The entire range of SiOCH films, with k=2.8~2.05, is characterized by low leakage currents of

제주대학교 중앙도서관
JEJU NATIONAL UNIVERSITY LIBRARY

about 10^{-9} A/cm^2 at 1 MV/cm and relatively low coefficients of thermal expansion of about 12×10^{-6}/K. The hardness and elastic modulus of the material decrease with dielectric constant.

3) Critical issues with porous dielectrics

Even though the reduction in the dielectric constant of the insulating material is a major step forward in the development of he next generation of interconnects, there are numerous technical issues to be addressed regarding the use of porous materials as dielectric layer for microelectronic applications. Many issues deal with pore size and distribution, and control over the pore parameters, but other factors like the feasibility or the complexity of process are also major concerns, especially when the reproducibility in high volume manufacturing is at stake. Most of the previously described porous dielectrics suffer from one or several of these issues.

제주대학교 중앙도서관
JEJU NATIONAL UNIVERSITY LIBRARY

To assure proper device operation, a porous dielectric film would need to have a homogeneous pore distribution with size that are 10~20 precent or less of the smallest feature size [32, 33]. In terms of the processing conditions, this would require tight control over the pore size and have a narrow size distribution. The pore interconnectivity is a critical material parameter that affects the electrical and mechanical parameter of the film. Large and open pores make the thin film more susceptible to metal diffusion that could adversely, as well as the adhesion to the interface. When the loading of pore generator is too high, large and interconnected pores may

obtained, resulting in high leakage current and poor mechanical strength. Clearly, the quantitative characterization and understanding of pore size and interconnectivity is important for optimizing the design of porous materials for low-k dielectric applications. With these limitations, the nature of the pores becomes a major concern in the development of porous materials.

Ⅲ. Theory

1. Characteristics of Dielectric materials

1) Capacitance and relative permittivity

The relative permittivity ε_r of a medium is defined as the ratio of the capacitances of a capacitor with and without the dielectric in place. The capacitance is described by its charge density s and plate area A in Fig. 8 [45]. The charge density s and the magnitude of the applied field E are related as

$$E = \sigma/\epsilon \tag{2-1}$$

The charge on the plates arises from the polarizing medium which induces a net charge density p.

제주대학교 중앙도서관
JEJU NATIONAL UNIVERSITY LIBRARY

The electric field between the plates can be written as

$$E = (\sigma - p)/\epsilon_0 \tag{2-2}$$

Since the electric field in both of these equations is the same, one obtains the following expression

$$p = \left(\frac{\epsilon - \epsilon_0}{\epsilon}\right)\sigma = (\epsilon_r - 1)\epsilon_0 E \tag{2-3}$$

The electric susceptibility χ_e is defined as

$$\chi_e = \epsilon_r - 1 \tag{2-4}$$

and writing the polarization and electric field as vectors, one obtains

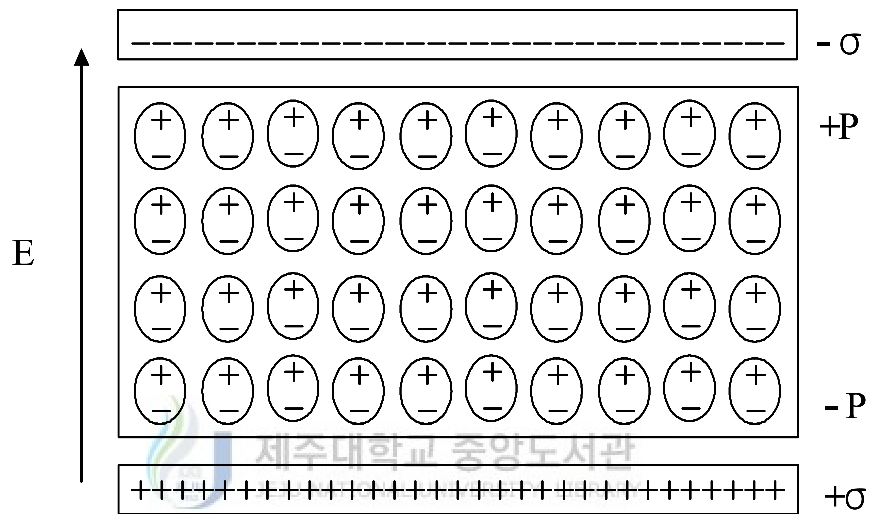

Fig. 8. Schematic cross section of two capacitor plates with surface charge density "σ" and a dielectric polarized by an electric field "E". Each circle denotes a polarization moment.

$$p = \chi_e \epsilon_0 E \qquad (2\text{-}5)$$

The next stage is relating the polarization of the medium, P, to the polarizability of its molecules. The polarization is the dipole moment density and equals the mean dipole moment of a molecule, p, in the medium, multiplied by the number density of molecules N. The induced dipole moment is proportional to the local electric field E^*. The local electric field is the total field arising from the applied field and the electric dipoles in which field stimulates in the medium. The polarization of the medium becomes

$$p = Np = \alpha N E^* \qquad (2\text{-}6)$$

with α the polarization constant. For a continuous dielectric, the Lorentz local field can be derived from electrostatics and is given by

제주대학교 중앙도서관
JEJU NATIONAL UNIVERSITY LIBRARY

$$E^* = E + P/3\epsilon_0 \qquad (2\text{-}7)$$

2) Polarization phenomena

The polarizability of a molecule is a measure of its ability to respond to an electric field and acquire an electric dipole moment p. There are several microscopic mechanisms of polarization involved with in dielectric material [46-49]. Electric dipole moments can be induced by of two types, namely induced by the electric field and permanent. The induced electric dipole moment can be a result of two polarization phenomena, i.e., electronic polarization and distortion polarization. Electronic polarization, α_e, describes the displacement of the cloud of bound electrons with reference to the nucleus under an applied electric field. The atom

distorts and the center of the atom's negative charge no longer coincides with the position of the nucleus, resulting in an electric dipole moment. The electric dipole moment of each atom is described by the expression

$$p = \alpha_e E^* \tag{2-8}$$

Distortion polarization α_d (also often referred to as ionic polarization) relates to the distortion of the position of the nuclei by the applied field, thereby stretching or compressing the bond length, depending on the relative orientation between the ionic bond and the electric field. The molecule is bent and stretched by the applied field and its dipole moment changes accordingly. Nonpolar molecules may acquire an induced dipole moment in an electric field on account of the distortion the field causes in their electronic distributions and nuclear positions.

제주대학교 중앙도서관
JEJU NATIONAL UNIVERSITY LIBRARY

A polar molecule is a molecule with a permanent electric dipole moment. The permanent dipole moment is a result of the partial charges on the atoms in the molecule that arise from the different electronegativity or other features of bonding. Polar molecules may have their existing dipole moments modified by the applied field. Orientation polarization relates to the phenomenon of a permanent dipole moment as a result of polar molecules.

The total polarization of a medium, composed of polarizable polar molecules, is therefore

$$P = N\left(\alpha_e + \alpha_d + \frac{\mu^2}{3kT}\right)E^* \tag{2-9}$$

where N is the number of molecules per m^3, μ is the orientation polarizability, k is the Boltzmann constant, and T is the temperature in K.

The terms α_e and α_d represent the electronic and distortion polarization in the molecule, while the term $\mu^2/3kT$ stems from the thermal averaging of permanent electric dipole moments in the presence of an applied field.

The quantitative relation between the relative permittivity and properties of the molecules is described by the Debye equation

$$\frac{\epsilon_r - 1}{\epsilon_r + 2} = \frac{N}{3\epsilon_0}\left(\alpha_e + \alpha_d + \frac{\mu^2}{3kT}\right) \qquad (2\text{-}10)$$

The relative permittivity ϵ_r of materials is high if its molecules are polar and highly polarizable. This equation shows that the permittivity is smaller if materials do not contain polar molecules. Reduction of density N and polarizabilities α_e and α_d are also possible ways to decrease the dielectric constant. Reducing the number of ionic bonds in the material minimizes distortion polarization. The electronic polarization is minimized by lowering the electron density in the material, i.e., introducing smaller elements.

제주대학교 중앙도서관
JEJU NATIONAL UNIVERSITY LIBRARY

The same expression, but without the permanent dipole moment contribution, is called the Clausius-Mossotti equation

$$\frac{\epsilon_r - 1}{\epsilon_r + 2} = \frac{N}{3\epsilon_0}\left(\alpha_e + \alpha_d\right) \qquad (2\text{-}11)$$

Although the value of the electric dipole moment is extremely important for predicting properties of dielectric materials, their calculation is difficult. In the case of simple molecules the Stark effect [12] is used to measure the electric dipole moment of molecules for which rotational spectra can be observed. In the case of more complicated systems, the polarizability and permanent dipole moment of

molecules can be determined by measuring ϵ_r at a series of temperatures. These measurements facilitate the determination of molar polarizations and their slope and intersect versus *1/T* give values of dipole moment and polarizability.

3) Film density and relative permittivity

The possibility to lower the molecular polarizability is limited. Equations (2-9)~(2-11) show that number of molecules per unit of volume (film density) plays an important role in reduction of the film permittivity. The effect of the density on the film permittivity is stronger that the effect of molecular polarizability since reducing density allows to reduce the dielectric constant to the extreme value close to unity.

Technologically, an important way to reduce the film density is introduction of pores. Generally, porous films can be considered as two-component materials where the solid skeleton has a dielectric constant close to the dense prototype and the second component (pores) has dielectric constant equal to 1. The relative permittivity of porous film ϵ_r directly depends on porosity.

제주대학교 중앙도서관
JEJU NATIONAL UNIVERSITY LIBRARY

$$(1-P)\frac{(\epsilon_2-1)}{(\epsilon_2+2)} \qquad (2\text{-}12)$$

In this equation ϵ_1 is permittivity of material inside the pores, ϵ_2 is permittivity of the film skeleton, and *P* is the film porosity. The term $P(\epsilon_1-1)/(\epsilon_1+2)$ is equal to 0 if the pores are empty, as experimentally demonstrated [50].

4) Relative permittivity and frequency

When the applied electric field is an ac field, the frequency of the signal comes into play. The polarization phenomena described above are very different for applied electric fields with different frequencies.

For an applied field

$$E = E_0 e^{-iwt} \tag{2-13}$$

the polarization vector is of the form

$$P = \epsilon_0 (\epsilon_r - 1) E_0 e^{-iwt} \tag{2-14}$$

and gives rise to a current density

$$J = -iw\epsilon_0 (\epsilon_r - 1) E_0 e^{-iwt} \tag{2-15}$$

which is imaginary as long as ϵ_r is real. This will not always be the case as will be discussed later. Let us first consider the consequences for the polarization phenomena. Electronic polarization follows the electric field almost instantaneously as only the displacement of bound electrons is involved. The distortion polarization can not respond as rapidly to fast changing fields since it involves the displacement of entire ions. Both electronic and distortion polarization are subject to a counteractive restoring force, which gives rise to a resonant frequency. In contrast, orientation polarization requires the motion of complete molecules. For orientation polarization there is no counteractive restoring force. Therefore, it does not give rise to a resonance at a critical frequency, as distortion and electronic polarization do. The orientation polarization is, however, opposed by thermal disorder. At low frequencies the three polarization phenomena contribute to the real part of the

제주대학교 중앙도서관 JEJU NATIONAL UNIVERSITY LIBRARY

dielectric constant. The maximum frequency for orientation polarization is of the order of 10^9 Hz. Above this frequency distortion and electronic polarization contribute to the dielectric constant up to the resonance frequency for distortion polarization, which is typically in the order of ~10^{13} Hz, and beyond that only electronic polarization is defining the dielectric constant. The resonant frequency of the electronic polarization is typically beyond the frequency of visible light at ~10^{15} Hz.

It follows from Maxwell's equations that the refractive index relates to the relative permittivity, beyond optical frequencies, as

$$n_r = \epsilon^{1/2} \tag{2-16}$$

Because of the relation between the relative permittivity and the molecular polarizability, one can relate n_r to the molecular properties as follows:

제주대학교 중앙도서관
JEJU NATIONAL UNIVERSITY LIBRARY

$$n_r = \left(\frac{1 + (2\alpha N/3\epsilon_0)}{1 - (\alpha N/3\epsilon_0)} \right)^{1/2} \approx 1 + \frac{\alpha N}{2\epsilon_0} \tag{2-17}$$

This expression leads to the Lorenz-Lorentz formula

$$\frac{n_r^2 - 1}{n_r^2 + 2} = \frac{N\alpha(w)}{3\epsilon_0} \tag{2-18}$$

The characteristic response of the different polarization phenomena to the electric field results in a frequency dependence which has not only an impact on the real part of the dielectric constant, but the imaginary part is related to the counteractive restoring forces in case of electronic and distortion polarization, and to the thermal disorder in case of orientation polarization. The imaginary component of the dielectric constant corresponds to a current density within the dielectric that is no

longer exactly $\pi/2$ out of phase with the electric field.

From the frequency dependence one should note that orientation polarization in low-k dielectrics should be prevented as much as possible, not only for its contribution to the dielectric constant but more importantly for the imaginary part of the dielectric constant. Indeed orientation polarization leads to heat dissipation in a frequency range that is envisioned within the application frequencies of microelectronics systems.

5) Dielectric constant

Any two conducting plates separated by an insulator (dielectric) or a vacuum form a capacitor (C) when applying a voltage (V). And the charge (Q) is stored at the surface of the two plates. The dielectric constant *(k)* which is degree of polarization of insulating material is a definition of the capacitance divided by vacuum's capacitance. However, the dielectric constant depends on the frequency of the electric field.

The dielectric constant of the film is composed of three polarizabilities, that is,

$$k_{total} = \alpha_{electronic} + \alpha_{ionic} + \alpha_{dipolar} \tag{2-19}$$

where $\alpha_{electronic}$, α_{ionic}, and $\alpha_{dipolar}$ are electronic (~10^{14} Hz), ionic (~10^{12} Hz), and dipolar (~10^{9} Hz) polarizabilities, respectively, as shown in Fig. 9. From experiments, we can distinguish three polarizabilities depending on the applied frequency. $\alpha_{electronic}$ and α_{ionic} can also be measured by ellipsometry (He-Ne laser : 632.8 nm) and Fourier transform infrared spectroscopy (FTIR), respectively.

제주대학교 중앙도서관 JEJU NATIONAL UNIVERSITY LIBRARY

$\alpha_{electronic}$ and α_{ionic} can be obtained from the square of refractive index (n^2) and from *Kramers-Kronig relation* analysis, respectively. Thus, we could determine $\alpha_{dipolar}$ as subtracting the two polarizations ($\alpha_{electronic}+\alpha_{ionic}$) from the total dielectric constant (k_{total}) at a frequency of 10^6 Hz. Consequently, we can find which component is the most important contribution to the dielectric constant and why the dielectric constant increases or decreases with deposition conditions and treatments [18, 51].

As shown in Fig. 9, the polarization is a frequency-dependent, intrinsic material property [47]. In this section, dielectric constant and imaginary part of refractive index are expressed as ϵ and *k*, respectively, in order to clarify the difference between them. The dielectric constant, ϵ, can be divided into three components that result from electronic, ionic, and dipolar polarization. The dielectric constants measured at the region of microwave region due to electronic ($\triangle\epsilon_e$), ionic ($\triangle\epsilon_i$), and dipolar contributions ($\triangle\epsilon_d$) are as expressed in Eq (1.2).

$$\epsilon_r \text{ (at 1 } MHz\text{)} = 1 + \triangle\epsilon_e + \triangle\epsilon_i + \triangle\epsilon_d \quad (2\text{-}20)$$

The dielectric constant of the material can also be calculated from the refractive index, as expressed in Eq (2-21):

$$\epsilon_r(\lambda) = n^2(\lambda) + k^2(\lambda) \quad (2\text{-}21)$$

where ϵ_r is a relative dielectric constant, n is a real part of refractive index, k is the imaginary part of a refractive index, and λ is the wavelength of a light source.

The pure electronic contribution to the dielectric constant ($\triangle\epsilon_e$) was calculated from

제주대학교 중앙도서관
JEJU NATIONAL UNIVERSITY LIBRARY

the refractive index obtained in the visible-ultraviolet (vis-UV) region. Since the extinction coefficient, k, of SiO_2-based materials is normally negligible in this region, the relative dielectric constant in equation (2-21) can be simply expressed as n^2 [53, 54]. The ionic contribution to the dielectric constant ($\triangle\epsilon_i$) was calculated by subtracting the dielectric constant at 632.8 nm, $1 + \epsilon_e$, from the dielectric constant the IR region, $1 + \triangle\epsilon_i + \triangle\epsilon_e$. To obtain the dielectric constant in the IR region, the refractive index was calculated from the Kramers-Kronig dispersion relation. The original Kramers-Kroing relation is expressed as Eq (2-22).

$$n_i = 1 + \frac{\pi}{2} P \int_0^{\infty} \frac{\nu k(\nu)}{\nu^2 - \nu_1^2} d\nu \qquad (2\text{-}22)$$

where n_i is the real part of the refractive index at the ith wave number at i, and k is the imaginary part of the refractive index (extinction coefficient).

제주대학교 중앙도서관
JEJU NATIONAL UNIVERSITY LIBRARY

The integration in Eq (2-22) cannot be performed from zero to infinity since the IR spectrum is obtained only in a finite region (650~4000 cm^{-1}). By introducing the refractive index at 632.8 nm (n_e at ν of 15,800 cm^{-1} to infinity is approximated as the dielectric constant at 632.8 nm calculated from the refractive index by ellipsometery, as explained in Eq (2-21).

$$n_i = n_e + \frac{\pi}{2} \left[\int_{650}^{\nu} \frac{\nu k(\nu)}{\nu^2 - \nu_1^2} d\nu - \int_{\nu_i}^{4000} \frac{\nu k(\nu)}{\nu^2 - 15800^2} d\nu \right] \qquad (2\text{-}23)$$

where n_e is the refractive index at 632.8 nm (15,800). The IR region dielectric constants were calculated by Eq (2-21) and (2-22).

The dipolar polarization was qualitatively estimated by the Clausius-Mossotti

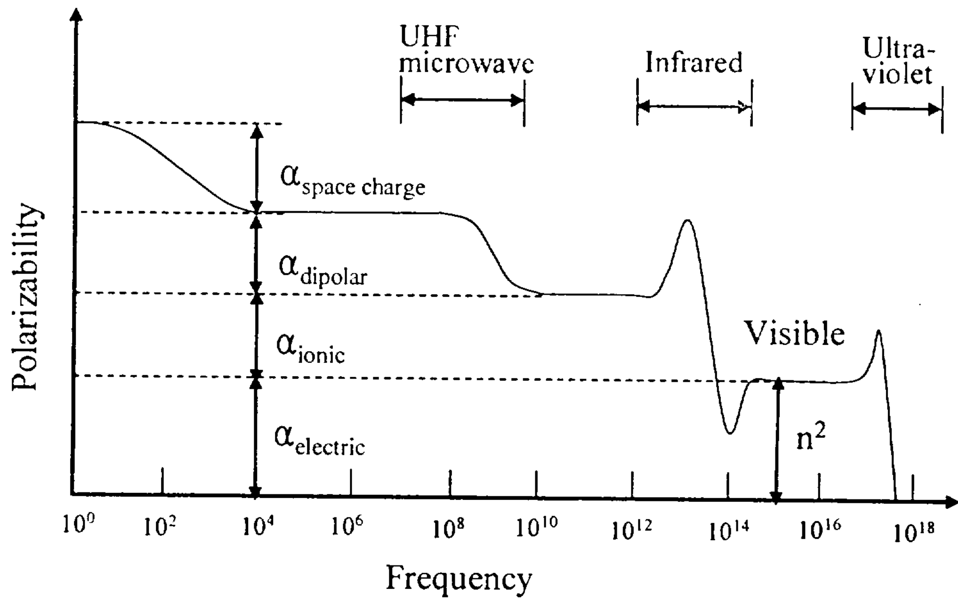

Fig. 9. Frequency dependence of the several factors contributing to polarizability.

제주대학교 중앙도서관
JEJU NATIONAL UNIVERSITY LIBRARY

relation in Eq (2-24) [24].

The dipolar polarization was qualitatively estimated by the Clausius-Mossotti relation in Eq (2-24) [24].

$$[\frac{(\epsilon_r - 1)}{(\epsilon_r + 2)}] = \frac{\rho}{M} \times \frac{N_A}{3\epsilon_0}(\alpha_{ie} + \alpha_d)$$
$$\alpha_d = \frac{P^2}{3kT}\ (dipolar\ \ polarizabilty) \quad (2\text{-}24)$$

where M is molecular weight, ρ is density, ϵ_r is the dielectric constant at 1 MHz, ϵ_0 is the vacuum dielectric constant, α_d is the dipolar polarizability, p is the dipole moment, k is the Boltzmann constant, and T is absolute temperature.

Unlike electronic and ionic polarizabilities, dipolar polarizability is inversely proportional to temperature, as is shown by Eq (2-24). Therefore, the temperature dependence of the polarizability per unit volume can imply that a dipole moment exists in the film.

제주대학교 중앙도서관

2. Analysis of mechanical properties

The analysis of indentation load-penetration curves produced by depth-sensing indentation systems is often based on work by Oliver and Pharr [54]. Their analysis was in turn based upon relationships developed by Sneddon [55] for the penetration of a flat elastic half space by different probes with particular axisymmetric shapes (e.g., a flat-ended cylindrical punch, a paraboloid of revolution, and a cone). In

general, the relationships between penetration depth, h, and load, P, for such indenter geometries can be represented in the form

$$P = \alpha (h - h_f)^m \qquad (2\text{-}25)$$

where α contains geometric constants, the sample elastic modulus, the sample Poisson's ratio, the indenter elastic modulus, and the indenter Poisson's ratio, h_f is the final unloading depth, and m is a power law exponent that is related to the geometry of the indenter; for a flat-ended cylindrical punch, m=1, for a paraboloid of revolution, m=1.5, and for a cone, m=2.

In applying Eq (2-25) to the calculation of modulus, Oliver and Pharr [54] made two significant realizations. First, the slope of the unloading curve changes constantly due to a constantly changing contact area. In prior research, the high load portion of the unloading curve was approximated as linear, which incorrectly assumes that the contact area remains constant for the initial unloading of the material. This practice created a dependence of calculated modulus values on the number of points used in the linear fit [54].

제주대학교 중앙도서관
JEJU NATIONAL UNIVERSITY LIBRARY

Second, if the unloading curve can be fit [54] by a power law expression (i.e., Eq. 2-25), then a derivative, dP/dh, applied at the maximum loading point (h_{max}, P_{max}) should yield information about the state of contact at that point. This derivative was termed the contact stiffness, S, and is given by

$$S = 2\alpha E_r = \frac{2\beta}{\sqrt{\pi}} E_r \sqrt{A} \qquad (2\text{-}26)$$

where α is the contact radius and A is the projected area of tip-sample contact. The reduced modulus, E_r, accounts for deformation of both the indenter and the sample

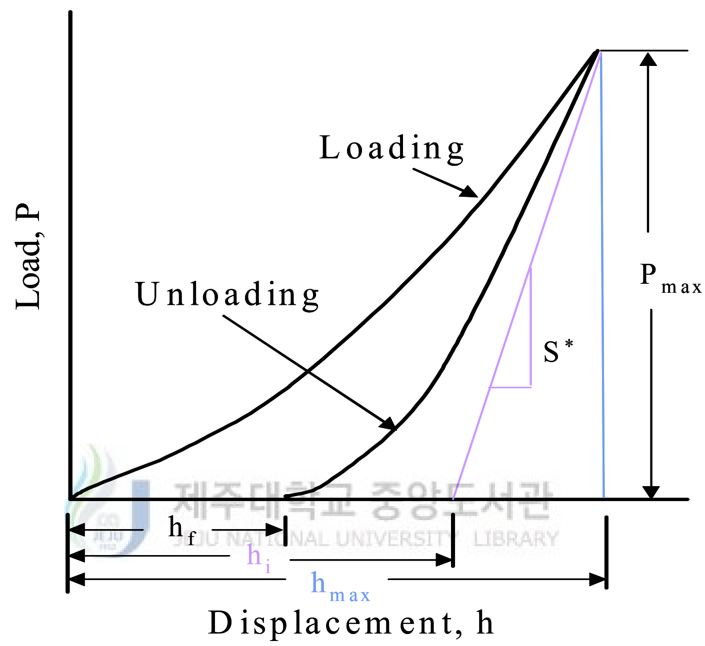

제주대학교 중앙도서관
JEJU NATIONAL UNIVERSITY LIBRARY

h_{max} = maximum displacement

h_f = final depth

h_i = intercept displacement

Fig. 10. An indentation load-displacement curve in which several important parameters used in the Oliver and Pharr analysis are illustrated.

and is given by

$$\frac{1}{E_r} = \frac{(1-\nu^2)}{E} + \frac{(1-\nu_i^2)}{E_i} \tag{2-27}$$

where E and ν are the sample elastic modulus and Poisson's ratio, respectively, and E_i and ν_i are the elastic modulus and Poisson's ratio, respectively, of the indenter material. β is used to account for the triangular and square cross sections of many indenters used in nanoindentation studies. For β= 1, the cross section of the indenter is assumed to be circular, as the contact radius, a, is replaced by $(A/\pi)^{1/2}$, and Eq. 2-26 (with β = 1) is valid for any indenter that has a shape described by a solid body of revolution of a smooth function. However, the values of β , as determined by King [56]) using numerical analysis, are only small corrections (e.g., β =1.03 for a triangular punch) and are not often used in practice. Another correction factor has recently been suggested due to unrealistic boundary conditions used by Sneddon [57]) (and also Hertz [58])). This correction factor, γ, which depends upon the sample Poisson's ratio, ν, and tip geometry ranges from approximately 1.05 to 1.10 for ν between 0.10 and 0.40 and a conical indenter with an opening angle of 70.32°.

In Fig. 10, an indentation load-displacement curve is illustrated along with several important parameters used in the Oliver and Pharr analysis. The stiffness, S^*, is the slope of the tangent line to the unloading curve at the maximum loading point (h_{max}, P_{max}) and is given by

$$S^* = \left(\frac{dP}{dh}\right)_{(h_{\max}, P_{\max})} = \alpha m\,(h_{\max} - h_f)^{m-1} \tag{2-28}$$

where the parenthetic subscript denotes that the derivative is evaluated at the

제주대학교 중앙도서관
JEJU NATIONAL UNIVERSITY LIBRARY

maximum loading point. When the displacement, h, is the total measured displacement of the system, S^* is the total system stiffness. After successful calibration and removal of the load-frame compliance, the displacement of the load frame is removed so that h represents only the displacement of the tip into the sample. In this case, $S^* = S$ and the tangent line represents an unloading path for which the contact area does not change. Thus, the contact area, A, calculated using S (see Eq. 2-26) should be the actual contact area at maximum load. Also, extrapolating this line down to $P = 0$ yields an intercept value for depth, h_i, which should be related to the contact depth, h_c, associated with the maximum loading point. However, h_c is related to the deformation behavior of the material and the shape of the indenter, as illustrated in Fig. 11. In fact, $h_c = h_{\max} - h_s$, where h_s is defined as the elastic displacement of the surface at the contact perimeter and can be calculated for specific geometries using displacement equations from Sneddon's analyses [50]). For each of three specific tip shapes (flat-ended punch, paraboloid of revolution, and cone), $h_s = \epsilon P_{\max}/S$ where ϵ is a function of the particular tip geometry. Thus, h_c is given by

$$h_c = h_{\max} - \frac{\epsilon P_{\max}}{S} \tag{2-29}$$

The nanoindentation procedures include calibration of the load-frame compliance, C_{lf}, and the tip shape area function, $A(h_c)$. Prior to the load-frame compliance calibration, the measured displacement, h_{total}, is a combination of displacement of the load frame, h_{lf}, and displacement of the sample, h_{samp}. Treating

제주대학교 중앙도서관 JEJU NATIONAL UNIVERSITY LIBRARY

the system as two springs (the load frame and the sample) in series under a given load, *P*,

$$h_{total} = h_{lf} + h_{samp} \tag{2-30}$$

Dividing both sides by *P*,

$$C_{toal} = C_{lf} + C_s = C_{lf} + \frac{\sqrt{\pi}}{2E_r}\frac{1}{\sqrt{A}} \tag{2-31}$$

where the total compliance $C_{total} = 1/S^*$ and the sample compliance $C_s = 1/S$. A number of possible methods exist for determining C_{lf} using a reference sample that is homogeneous and isotropic and for which both E and ν are known. Typically, a series of indentation measurements are made on the reference sample. Oliver and Pharr [54] suggested using an iterative technique to calibrate both the load-frame compliance and the tip shape with one set of data from a single reference sample, as both C_{lf} and A are unknowns in Eq. (2-31). While this method has the advantage of not requiring an independent measurement of the area of each indent, its use has been limited, perhaps because it is mathematically intensive.

The use of the AFM with indentation measurements provides a method of high-resolution imaging of the plastic impression, which should have approximately the same projected area as the contact area at maximum load, particularly for a highly plastic reference material such as aluminum. Using this type of an approach, the measured compliance, C_{total}, can be plotted as a function of $1/\sqrt{A}$. A linear curve fit to the data can then be used to determine the load-frame compliance, C_{lf}, which will be the value of the y-intercept. A third method and the one used in the

제주대학교 중앙도서관
JEJU NATIONAL UNIVERSITY LIBRARY

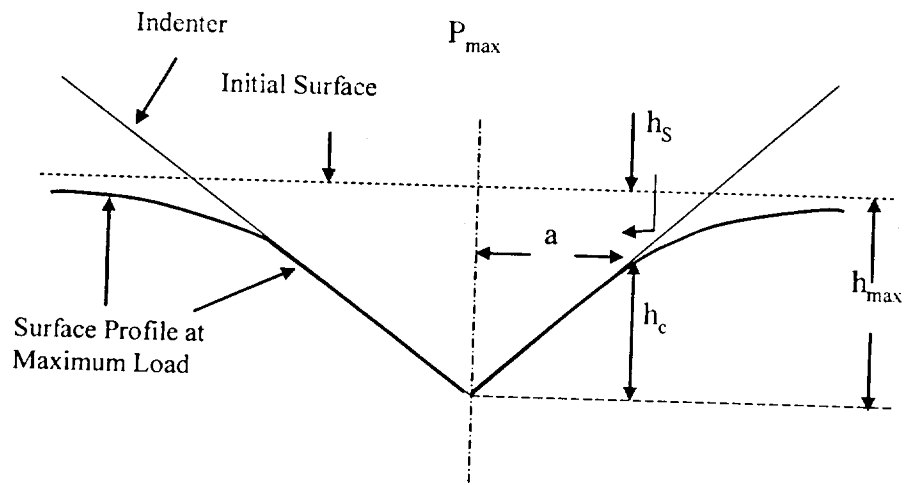

Fig. 11. Illustration of the indentation geometry at maximum load for an ideal conical indenter.

제주대학교 중앙도서관
JEJU NATIONAL UNIVERSITY LIBRARY

present research is to assume that not only is E independent of penetration depth but also hardness, $H = P_{max}/A$. Thus, if H is constant, C_{total} can be plotted as a function of $1/\sqrt{P_{max}}$, and again the y-intercept of the fitted linear curve yields C_{lf}. In this method, aluminum is often replaced by fused silica, because oxide formation on aluminum can create variations in E and H with penetration depth [59].

3. Analysis of Time of flight-Elastic recoil detection

The film composition was determined by TOF-ERD analysis. The density was also calculated using this tool. Elastic recoil detection analysis (ERDA) is one of the most promising methods for determining of light elements in solid-state samples, especially when information along with depth is required [60]. This analysis is very similar to Rutherford back scattering (RBS). By measuring the time of flight with the energy of recoil particle, a two-dimensional plot having the energy and time dimension can be obtained which contains separated curves representing single masses. Measuring the TOF with the energy of a recoil particle has two large advantages. Firstly, the mass of a recoil particle can be calculated without considering the depth from which the recoil particle came. In the case of conventional ERDA, the mass of a recoil particle from the sample surface is calculated using its kinetic energy. Secondly, clearly separated curves appear in energy-time plot,

제주대학교 중앙도서관
JEJU NATIONAL UNIVERSITY LIBRARY

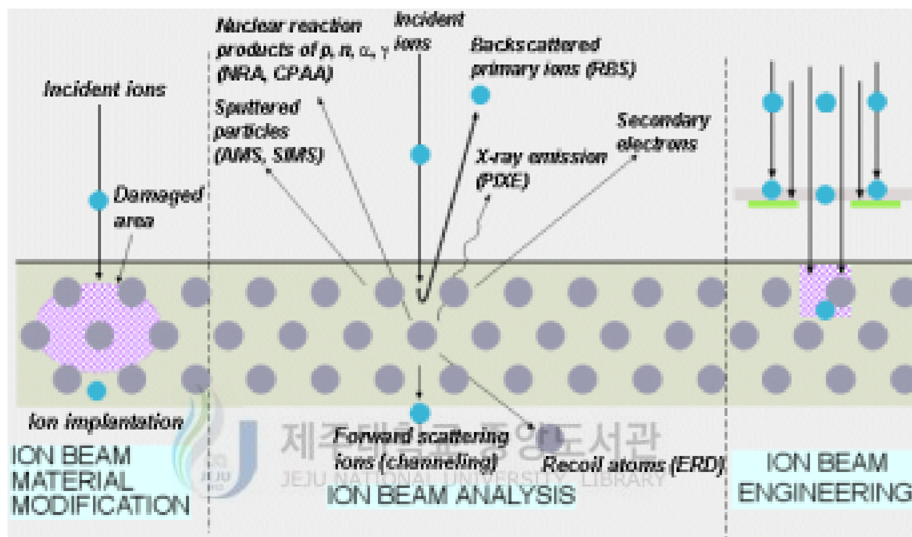

Fig. 12. Interaction of ion-beam and material.

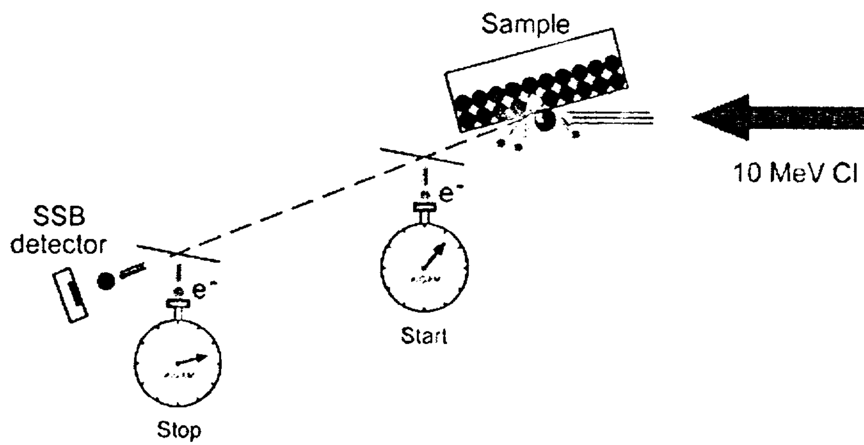

Fig. 13. Schematic diagram of ERD-TOF analysis system.

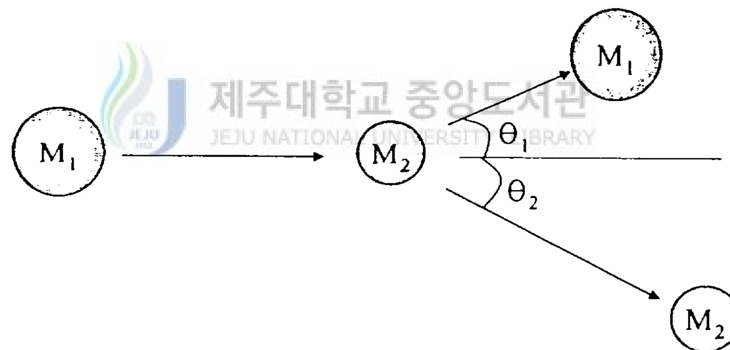

제주대학교 중앙도서관
JEJU NATIONAL UNIVERSITY LIBRARY

Fig. 14. Schematic diagram of two particles before and after collision.

even though the peaks in the energy spectrum overlap. This is very useful information for deciding whether an element exist in a sample or not. The last one is that a very low background has achieved, since any interference from other peaks can be eliminated by peak separation using a TOF-energy two-dimensional scatter plot.

When a particle of mass M_1 is moving and collides with a stationary particle of mass M_2, the energy is transferred from the moving particle to the stationary one. The stationary particle has kinetic energy and recoils after the collision. A schematic representation is given in Fig. 14.

Since the collision is elastic, sums of the kinetic energies and momentums of two particles before and after the collision are conserved. If the ratio of the energy of the scattered particle (E_1) and the recoil energy (E_2) to the incident energy (E_0) is defined as the kinematic factor of the scattering and recoil particle (K_S and K_R, respectively) [61].

제주대학교 중앙도서관
JEJU NATIONAL UNIVERSITY LIBRARY

$$K_s \equiv \frac{E_1}{E_0} = \left(\frac{(M_2^2 - M_1^2 Sin^2\theta_1)^{1/2} + M_1 cos\theta_1}{M_1 + M_2} \right)^2 \quad (2\text{-}32)$$

$$k_R \equiv \frac{E_2}{E_0} = \frac{4M_1M_2}{(M_1+M_2)^2} cos^2\theta_2 \quad (2\text{-}33)$$

where M_1 and M_2 are the mass of the probe ion and the recoil atom, respectively; θ_1 and θ_2 are the scattering and recoil angles from the probe-ion direction, respectively. Since the kinematic factors (K_S and K_R) are functions of the target mass (M_2), only when the experimental condition is fixed and the target mass surface cab be known if the recoil energy (E_2) is

measured.

The mass of a detected particle in the case of TOF-energy spectrometer is represented by

$$M = 2E\left(\frac{t}{l}\right)^2 \tag{2-34}$$

where M and E are the mass and energy of a recoiled particle, respectively; t and l are the time of flight of the flight path. Therefore, the mass resolution of the measurement system was calculated using

$$\left(\frac{\triangle M}{M}\right)^2 = \left(\frac{\triangle E}{E}\right)^2 + \left(\frac{2\triangle t}{t}\right)^2 + \left(\frac{2\triangle l}{l}\right)^2 \tag{2-35}$$

제주대학교 중앙도서관
JEJU NATIONAL UNIVERSITY LIBRARY

4. Bruggeman's effective medium

In case of the compound of over two materials by physical mixture, the calculation method of dielectric reaction of the compound is very useful for the measurement of pore fraction. Introduction of nanometer-sized pores into the material is a natural extension of this strategy to increase the free space and decrease the material density. The effect of porosity on dielectric constant can be predicted using a simple model, such as the Bruggeman effective medium approximation [1, 18, 62]:

$$f_1 \frac{k_1 - k_e}{k_1 + 2k_e} + f_2 \frac{k_2 - k_e}{k_2 + 2k_e} = 0 \tag{2-36}$$

where $f_{1,2}$ (f_1+f_2=1) represents the fraction of the two components, $k_{1,2}$ the dielectric constant of the components, and k_e is the effective dielectric constant of the material. The model assumes two components of the film: the solid wall material and voids (k=1). Figure 1 shows the dielectric constant as a function of porosity predicted by the model for SiO_2 (k=4.0) and for a lower k=2.6 wall material. If k_1=1 and k_2=4.0 then

$$f_1 \frac{1-k_e}{1+2k_e} + (1-f_1)\frac{4-k_e}{4+2k_e} = 0 \tag{2-37}$$

$$2k_e^2 + (9f_1 - 7)k_e - 4 = 0 \tag{2-38}$$

If k_1=1 and k_2=2.6 then

$$f_1 \frac{1-k_e}{1+2k_e} + (1-f_1)\frac{2.6-k_e}{2.6+2k_e} = 0 \tag{2-39}$$

제주대학교 중앙도서관
JEJU NATIONAL UNIVERSITY LIBRARY

$$2k_e^2 + (4.8f_1 - 4.2)k_e - 2.6 = 0 \tag{2-40}$$

The plots show that the value decreases slightly faster than linearly. Although the model is simple, the predicted results appear to be in reasonable agreement with recent experimental measurements on methyl silsesquioxane [58] and oxide porous films. Differences between the theoretical prediction and experimental results are likely related to surface chemistry, such as the presence of terminating OH groups and adsorbed water, and to the pore geometries.

One point demonstrated in Fig. 15 is that to obtain a given k value, significantly less porosity would have to be incorporated into the lower k material than into the SiO_2. For example, to get to k=2.0, about 55 % porosity would be needed in an oxide material, whereas only ~35 % would be needed in the lower k material. Since

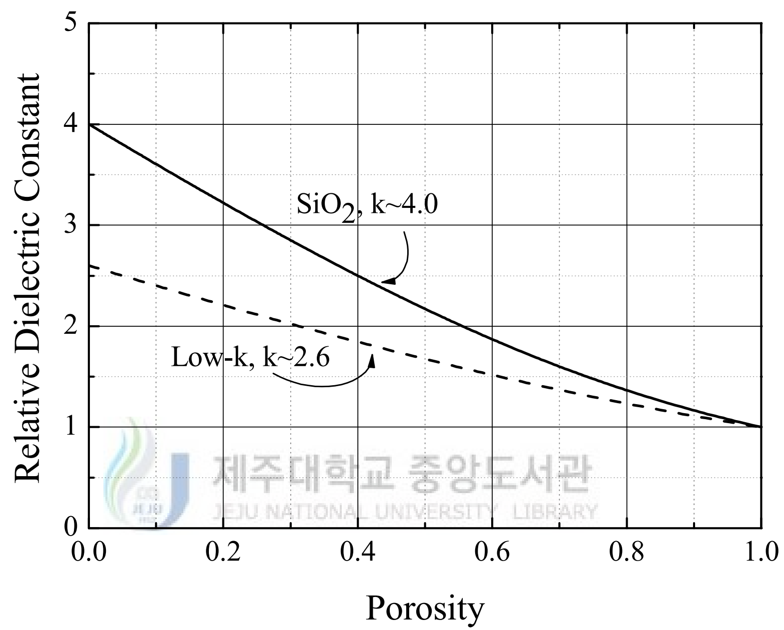

제주대학교 중앙도서관
JEJU NATIONAL UNIVERSITY LIBRARY

Fig. 15. Bruggeman's effective medium approximation showing dielectric constant versus porosity for oxide and a low-k material.

Sa high percentage porosity in the film can be expected to give rise to a number of reliability concerns, there is a definite advantage in using a lower k starting material to minimize the amount of porosity needed.

5. Carrier transport in insulating films

In an ideal MIS diode the conductance of the insulting film is assumed to be zero. Real insulators, however, show carrier conduction when the electric field or temperature is sufficiently high. To estimate the electric field in an insulator under basing conditions, we obtain from Equation

제주대학교 중앙도서관
JEJU NATIONAL UNIVERSITY LIBRARY

$$m_{dh} = (m_{lh}^{*3/2} + m_{hh}^{*3/2})^{2/3} \tag{2-41}$$

where m_{dh} is the density-of-state effective mass of valence band, the subscripts refer to "light" and "heavy" hole masses [64].

$$n = N_D^+ + p \tag{2-42}$$

$$N_D^+ = N_D\left(1 - \frac{1}{1 + \frac{1}{g}\exp\left(\frac{E_D - E_F}{kT}\right)}\right) \tag{2-43}$$

where n is the electron density in the conduction band, p the hole density in the valence band, N_D^+, the number of ionized donors.

$$\varepsilon_i = \varepsilon_s\left(\frac{\epsilon_s}{\epsilon_i}\right) \tag{2-44}$$

where E_i and E_S are the electric field in the insulator and semiconductor,

respectively, and ε_i and ε_s are the corresponding permitivities [64]. For the Si-SiO_2 system, the field for silicon at avalanche breakdown is about 3×10^5 V/cm; the corresponding field in the oxide id then three times larger ($\varepsilon_{Si}/\varepsilon_{SiO_2}$=17.1/3.9), that is about 10^6 V/cm. At this field the electron and hole conductance in the SiO_2 are negligible even at elevated temperatures. However, mobile ions such as sodium can transport though the oxide and give rise to device instability and a hysteresis effect. For ultrathin SiO_2 or under a very high electric field, tunneling will occur. In either Si_3N_4 or Al_2O_3 the conductance is generally much higher than in SiO_2.

Table 4 summairzes the basic conduction process in insulators. A plot of $\ln(J/T^2)$ verses $1/T$ yields a straight line with a slope determined by the permitivity ϵ_i of the insulator. The Frenkel-Poole emission is due to field-enhanced thermal excitation of trapped electrons into the conduction band. For trap states with coulomb potentials, the expression is virtually identical to that to that of the Shottky emission. The barrier hight, however, the depth of the trap potential well, and the quantity $\sqrt{q/\pi\varepsilon_i}$ is larger than in the case of Schottky emission by a factor of 2, since the barrier lowering is twice as large due to the immobility of the positive charge. The tunnel emission is caused by field ionization of trapped electrons into the conduction band or by electrons tunneling from the metal Fermi energy into the insulator conduction band. The tunnel emission has the strongest dependence on the applied voltage but is essentially independent of the temperature. The space-charge-limited current results from a carrier injected into the insulator, where no compensating charge is present. The current for the unipolar trap-free case is proportional to the square of

제주대학교 중앙도서관
JEJU NATIONAL UNIVERSITY LIBRARY

the applied voltage. At low voltage and high temperature, current is carried by thermally excited electrons hopping from one isolated state to the next. This mechanism yields an ohmic characteristic exponentially dependent on temperature. The ionic conduction is similar to a diffusion process. Generally, the dc ionic conductivity decreases during the time the electric field is applied, because ions cannot be readily injected into or extracted from the insulator. After an initial current flow, positive and negative space charges will build up near the metal-insulator and semiconductor-insulator interface, causing a distortion of the potential distribution. When the applied field is removed, large internal fields remain which cause some, but not all, ions to flow back toward their equilibrium position; hysteresis effects result.

제주대학교 중앙도서관
JEJU NATIONAL UNIVERSITY LIBRARY

Table 4. Basic conduction processes in insulators.

Process	Expression[a]	Voltage and temperature dependence[b]
Schottky emission	$J=A^{*}T^{2}\exp(\frac{-q(\phi_{B}-\sqrt{q\varepsilon/4\pi\varepsilon_{i}}}{kT})$	$\sim T^{2}\exp(+a\sqrt{V}/T-q\phi_{B}/kT$
Frenkel-Pool emission	$J\sim E\exp(\frac{-q(\phi_{B}-\sqrt{qE/4\pi\varepsilon_{i}}}{kT})$	$\sim V\exp(+2a\sqrt{V}/T-q\phi_{B}/kT$
Tunnerl or field emission	$J\sim E^{2}\exp(-\frac{4\sqrt{2m^{*}}(q\phi_{B})^{3/2}}{3q\hbar E})$	$\sim V^{2}\exp(-b/V)$
Space-charge-limited	$J=\frac{8\varepsilon_{i}\mu V^{2}}{9d^{3}}$	$\sim V^{2}$
Ohmic	$J\sim E\exp(-\triangle E_{ae}/kT)$	$\sim V\exp(-c/T)$
Ionic conduction	$J\sim\frac{E}{T}\exp(-\triangle E_{ai}/kT)$	$\sim\frac{V}{T}\exp(-d/T)$

[a] A^{*}=effective Richardson constant, ϕ_b=barrier height, E=electric field, ϵ_i =insulator dynamic permitivity, m*=effective mass, d=insulator thickness, $\triangle E_{ae}$ =activation energy of electrons, $\triangle E_{ai}$=activation energy of ions, and $a\equiv\sqrt{q/4\pi\varepsilon_{i}d}$. [b] $V=Ed$. Positive constants independent of V or T are b, c, and d'.

제주대학교 중앙도서관 JEJU NATIONAL UNIVERSITY LIBRARY

Ⅳ. Experiments and Analysis

1. Formation of the SiOC(-H) films

The hybrid-type SiOC(-H) films were deposited on p-type Si(100) wafers by using a mixture of bis-trimethylsilylmethane (BTMSM) and oxygen gases in a radio-frequency (13.56 MHz) inductively coupled plasma chemical vapor deposition (ICPCVD) system. The wafers were kept in a floating potential and were not intentionally heated. The wafers were cleaned by a standard cleaning procedure before loading them into the reaction chamber. The inductively coupled plasma was generated by means of a three-turn coil, which was set around a quartz tube. A base pressure of 10^{-6} Torr was reached before each deposition. The BTMSM precursor was a nontoxic, colorless liquid with a boiling point of 137 ℃ and a melting point of -41 ℃ at standard atmospheric pressure. It was vaporized and carried by inert argon gas from a thermostatic bubbler (maintained at 40 ℃) to the reaction chamber. To prevent recondensation of BTMSM, all of the gas delivery lines were heated and kept at a constant temperature of 40 ℃. We were controlled carbon concentration by BTMSM flow rate ratios. The flow rate ratios as R(%)=[BTMSM/(BTMSM+O_2)] was varied from 45 to 85 % and the total gas flow rates were kept at a constant of 40 sccm. The O_2 and BTMSM gases were introduced through a mass flow controller (MFC) into the reaction chamber, and the discharge pressure was measured with a Baratron gauge and kept at about 2.5×10^{-1} Torr. The film was deposited at room

제주대학교 중앙도서관
JEJU NATIONAL UNIVERSITY LIBRARY

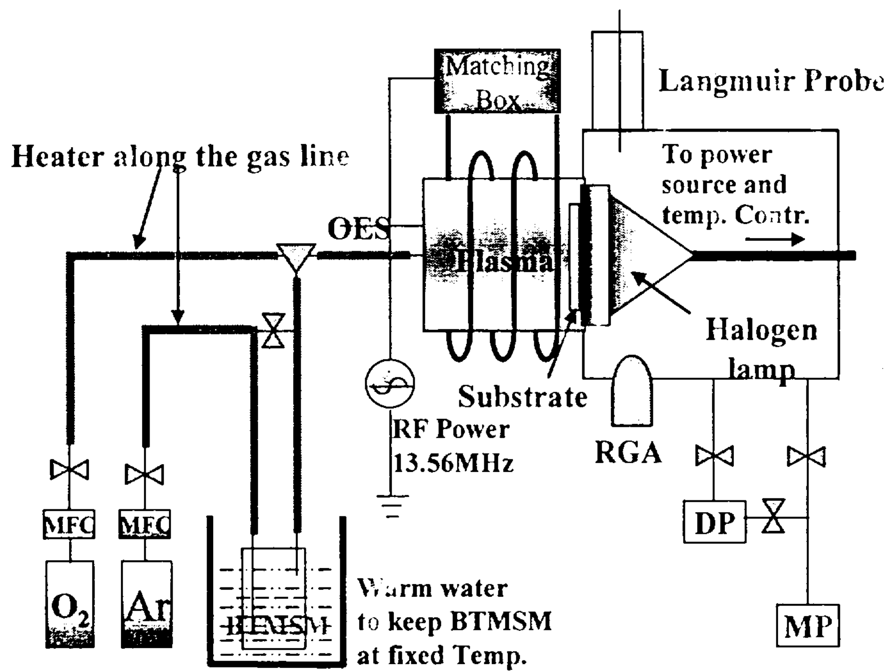

제주대학교 중앙도서관
JEJU NATIONAL UNIVERSITY LIBRARY

Fig. 16. Schematic diagram of ICP-CVD system.

Table 5. Experimental condition

Antenna structure	3 turn
RF power	300 W, 13.56 MHz
Total flow rate	40 sccm
O_2 gas flow rate	6 ~ 22 sccm
BTMSM(Ar gas) flow rate	18 ~ 34 sccm
Gas line bubbler temp.	40℃
Initial Pressure	~ 10^{-5} Torr
Working pressure	200 mTorr
Deposition time	5 min
Annealing temp. & time	200℃, 300℃, 400℃, 30 min
Wafer	p-type Si (100)

temperature and the annealing process was performed at 200, 300 and 400℃ for 30 minutes in a vacuum for study on the annealing effects of the film.

제주대학교 중앙도서관

2. Analysis of the bonding structure on SiOC(-H) films

To investigate the chemical bonding structure of SiOC(-H) films with a nano-pore structure, we carried out the post-annealing at 200, 300, and 400 ℃, applied temperature to process, for 30 min in a vacuum. The properties of the SiOC(-H) film such as bonding mode, spectrum of FWHM, peak position, related carbon concentration, peak area ratio, have been characterized by Fourier transform infrared (FTIR) spectra. FTIR spectroscopy (IFS-120HR/FRA-106S Bruker) was used to determine the related Si-O-C bonding configurations in the film.

3. XPS analysis

Chemical state of the element, bonding energy, and transition of each elements bonding energy according to carbon concentration distribution and annealing condition, initial forming procedure and reaction mechanism are investigated by X-ray photoelectron spectroscopy (XPS). Survey scan spectra and narrow scan spectra of each element are proceeded at the pass energy of 100 eV and 20 eV, respectively. The depth profile is carried out by Ar ion sputtering (20Å/min) method. Element analysis is performed in low resolution scan by survey spectrum. The purpose of this composition analysis is to verify a critical concentration of C depending on an optimum condition of a lowering of dielectric constant and to process temperature and planarization of Si-O-C(-H) films. XPS (ESCA 2000-Lab) was used to determine the related Si-O-C bonding configurations in the film.

제주대학교 중앙도서관
JEJU NATIONAL UNIVERSITY LIBRARY

4. Measurements of TOF-ERD

The film composition was determined by time of flight elastic recoil detection (TOF-ERD) analysis. TOF-ERD analysis is one of the most promising methods for determining of light-element in solid-state samples, especially when information along with depth is required. The method is that the time of flight elastic recoil and energy are detected at once and convert to mass and energy data. In this experiment, $^{35}Cl^{5+}$ ions accelerated to 9.628

MeV were employed. The SSB detector, time detector, sample and incidence beam are in the same plane in Fig. 14. The length of the flight path between the carbon foil and SSB detector is variable, and was chosen to be to be 314 mm. The mass resolution is fully detachable for light element of under fluorine, the depth resolution is 50 Å, the possible depth of analysis is about 3000 Å. A detecting sensitivity is 10^{13}~10^{14} atoms/cm^2 that is analysis about element of 0.1 % concentration. In case of the sufficiently large mass and energy of using element can analysis all element in the sample at once.

5. Measurements of pore distribution

제주대학교 중앙도서관
JEJU NATIONAL UNIVERSITY LIBRARY

The pore size distribution, and change of pore number distribution in the films by annealing were measured by SANS. The shape of nano pores in film can be assumed as sphere. The scattering length density was calculated with the assumption that the void smaller than 50 nm were dispersed equally. The size distribution function for spherical center is given by

$$N(R) = \sum_i N_{0i} exp\left[-0.5\left(\frac{ln(R) - ln(R_{0i})}{s_i}\right)^2\right] \tag{3-1}$$

where unknown parameters N_o, R_o and S_i are the standard scaling factor, center and width parameters of this distribution type, respectively. These log-normal distributions were fitted with non linear least fitting program SANSFITTCL for the range of Q as 0.014~0.250 Å^{-1} [65-67].

The SANS measurements were carried out on the SANS instrument at the

HANARO reactor of Korea Atomic Energy Research Institute. The neutron wavelength, was 4.31 nm and a wavelength spread ($\Delta\lambda/\lambda$) was 12 %. The sample to detector distance was 3 m. The resultant scattering vector, Q, was in the range of 0.014~0.250 $Å^{-1}$. To increase the sensitivity of measurement, 16 pieces of 2×2 cm^2 samples were stacked in series.

6. Nano-indentation experiments

Mechanical properties such as hardness (H), elastic modulus (E) of the film are investigated by nano-indentation method. The hardness invariability observed for the indentation depth of above 20 nm indicates that there is no influence of the substrate on the measured hardness value. The maximum indentation depth used in thin-film hardness measurements should not exceed 10 % of the film thickness. Nano-indentation measurements were performed using a Triboscope with Nanoscope Ⅱ (Hysitron, Inc) to determine the elastic modulus and hardness of the dielectric films.

제주대학교 중앙도서관
JEJU NATIONAL UNIVERSITY LIBRARY

7. I-V and C-V measurements

The electrical properties of the Si-O-C(-H) films, such as dielectric constant, leakage current and breakdown voltage, are measured by C-V and I-V measurements. For measuring the electrical properties, aluminum top

electrodes were deposited by direct current (DC) magnetron sputtering, and the metal-insulator-semiconductor (MIS) capacitors were fabricated by lithography and the wet-etch technique. The electrode area of 2.50×10^{-3} cm^2 and 1.15×10^{-3} cm^2 are made by photolithography. The applied voltages for C-V and I-V measurements are -30 V to 30 V and 100 V, respectively. The dielectric breakdown is the DC voltage at which permanent dielectric breakdown occurred and then the one is divided by film thickness. The dielectric constant at 1 MHz and current-voltage (I-V) characteristics were measured by a HP4280A C-V meter and HP4155B semiconductor parameter analyzer, respectively.

8. The surface morphology and roughness

제주대학교 중앙도서관
JEJU NATIONAL UNIVERSITY LIBRARY

The relationship between film morphology and deposition, annealed condition could be seen from the field emission scanning electron microscopy (FE-SEM) images. Roughness of the films was investigated with Atomic force microscopy (AFM). The measurements were performed in the air using PSI Auto Probe CP.

9. TEM images

Nano-sized pore structure of the films was observed with cross-sectional transmission electron microscopy (TEM). TEM observations with a JEOL

JEM 2000 EX instrument were carried out in order to examine nano-pore structure of the film.

10. Measurements of film thickness

The thickness and the refractive index, deposition rate as a function of flow rate and annealed condition of the Si-O-C(-H) films were measured by an ellipsometer (Gaertner L116 D) at a wavelength of 632.8 nm, FE-SEM and α-step (Tencor 200).

Ⅴ. Results and Discussion

1. Chemical properties

1) Bonding structure of SiOC(-H) films

Bonding characteristics of SiOC(-H) composite films is investigated by FTIR absorbance analysis. Figure 17 shows the FTIR spectra of as-deposited SiOC composite films with various [BTMSM/(O_2+BTMSM)] flow rate ratios. The spectra are generally broadened and overlapping due to the complex stoichiometry and the amorphous nature of the films. It is known that there are rocking and bending modes of Si-CH_3 (890, 1273 cm^{-1}), Si-O-Si(C) (1050 to 1250 cm^{-1}), CH_n(n=1,2,3) (740, 1450 and 2970 cm^{-1}), and OH-related (3720 cm^{-1}) bonds in the film, respectively. In the range of 1000 to 1250 cm^{-1}, the bonding mode at around 1030 cm^{-1} corresponds to the Si-O-Si asymmetric stretching mode, the bonding mode near 1063 cm^{-1} is the ring-link form of the Si-O-C asymmetric stretching mode and the bonding mode near 1109 cm^{-1} is the open link form of the Si-O-C asymmetric stretching mode [68, 69]. The bonding modes near 1171 and 1276 cm^{-1} are due to the Si-C cage-link stretching and Si-CH_3 bonding modes, respectively. The peak position of Si-O-C mode is shifted to a lower wave number (red shift) with the increase of R (%) flow rate ratios. This frequency shift in IR spectra is related to the change of bonding characteristics, such as bonding structure and bond length [70, 71]. When compared with the relative intensities of the related bonding modes, the peak intensities of the

제주대학교 중앙도서관
JEJU NATIONAL UNIVERSITY LIBRARY

$Si-CH_3$ and the CH_3 bonding modes increased with increasing R (%) flow rate ratios. The shoulder at the higher wavenumber of the 1109 cm^{-1} absorption peak indicates the existence of a cage type Si-C bond structure. In this case, the peaks in the wavenumber range of 1000 to 1250 cm^{-1} correspond to several substructure bonds such as the cage-link, the open-link and the ring-linked Si-O-C bonds. Not only are there main skeleton atomic Si-O-Si or Si-O-C groups, but also many other groups such as OH and CH_n modes [70]. The skeleton atomic groups are very similar to thermal SiO_2. This result shows the peak structure for clearly separated Si-O-Si and Si-O-C bonds, as well as indicating the existence of a caged Si-C bond which reflects the enhanced porosity in the film [72]. This means that there are at least two ways by which C atoms can be incorporated in the SiOC(-H) films during deposition. The first is by $-CH_3$ groups attached to Si atoms in Si-O-Si networks, and the other is by Si-O-C substructure.

제주대학교 중앙도서관
JEJU NATIONAL UNIVERSITY LIBRARY

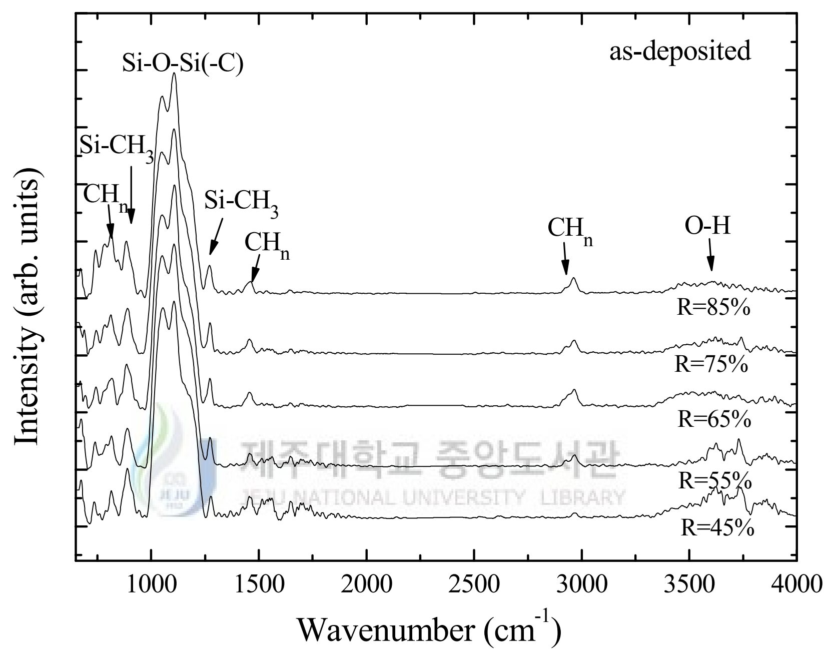

제주대학교 중앙도서관
JEJU NATIONAL UNIVERSITY LIBRARY

Fig. 17. FTIR spectra of SiOC(-H) films prepared with various BTMSM/(O_2+ BTMSM) flow rate ratios.

Figures 18~20 shows the FTIR spectra of the annealed samples at 200, 300 and 400 ℃ with various R (%) flow rate ratios. The bonding structure is similar to that of Fig. 17. The intensities of Si-CH_3, CH_n and OH-related bond groups are slightly lower than those of as-deposited films. Also the line shape of the Si-O-C and Si-O-Si bonding modes changed a little with annealing. This result indicates that some CH_n species are removed from the bulk of the film due to the annealing process, and that some of the Si-O-Si bonds change into Si-O-C bonds including ring, open and cage links in which C atoms have been incorporated. Therefore this transformation of bonding mode is responsible for the formation of the nano-size voids in the film. It was noted that when the post annealing temperature was above 300 ℃, nano-sized pores formed in the film because there of the aloof force between the CH_3 group and other parts of the Si-O-Si links [68, 69]. Grill *et al*. reported that the annealed ultra low-*k* films had significantly higher C and H concentrations than the pure SiOC(-H) film, indicating the incorporation of significant amounts of CH_3 fragments in the structure of annealed films [73]. Therefore, we can infer that post annealing induces rearrangement of the chemical bonds in SiOC(-H) film. As previously mentioned, voids formed in film can result in a low dielectric constant [74].

제주대학교 중앙도서관
JEJU NATIONAL UNIVERSITY LIBRARY

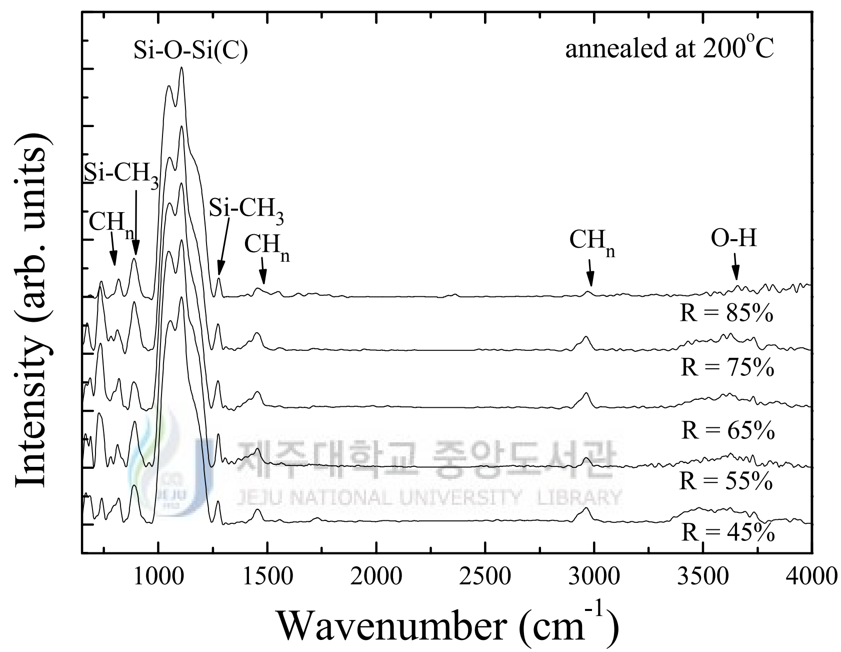

제주대학교 중앙도서관
JEJU NATIONAL UNIVERSITY LIBRARY

Fig. 18. FTIR spectra of SiOC(-H) films prepared with various BTMSM/(O_2+BTMSM) flow rate ratios for annealed films at 200 ℃ for 30 min.

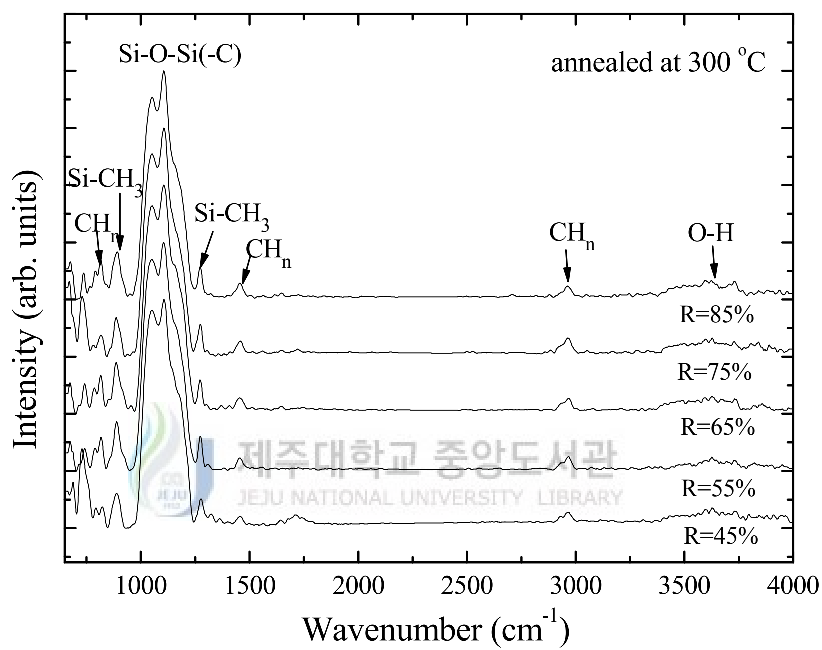

제주대학교 중앙도서관
JEJU NATIONAL UNIVERSITY LIBRARY

Fig. 19. FTIR spectra of SiOC(-H) films prepared with various BTMSM/(O_2+BTMSM) flow rate ratios for annealed films at 300 ℃ for 30 min.

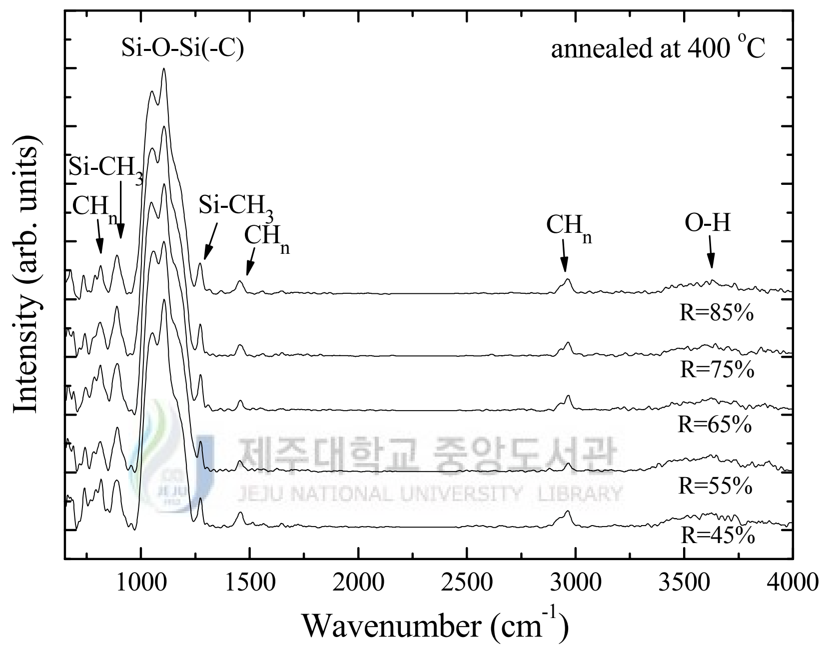

제주대학교 중앙도서관
JEJU NATIONAL UNIVERSITY LIBRARY

Fig. 20. FTIR spectra of SiOC(-H) films prepared with various BTMSM/(O_2+ BTMSM) flow rate ratios for annealed films at 400 ℃ for 30 min.

In order to investigate the Si-O-C bonding mode in the as-deposited SiOC(-H) film, the spectra in the range of 950 cm^{-1} to 1250 cm^{-1} were deconvoluted. The peaks are resolved by Gaussian fitting and the result is shown in Fig. 21 (a). From Fig. 21 (a), we know that the bonding mode near 1017 cm^{-1} is for the Si-O-Si asymmetric stretching mode, while bonding modes near 1056 cm^{-1} and 1106 cm^{-1} are for Si-O-C asymmetric ring-link and open-link stretching modes, respectively [68, 69]. The broad bonding mode at 1161 cm^{-1} is for the Si-O-C cage-link stretching mode [70].

Figures 21~24 show the FTIR spectra of the annealed samples at 200, 300 and 400 ℃ with various BTMSM/(O_2+BTMSM) flow rate ratios. We compared the relative intensities and peak areas of the related bonding mode of as-deposited samples with that of the annealed samples. The annealed samples showed little change in the absorption area for Si-O-Si bond (1016 cm^{-1}) and the Si-O-C cage link bond (1166 cm^{-1}), but the absorption area of Si-O-C bond (1106 cm^{-1}) in Si-O-Si open link decreased, while those of Si-O-C bond (1062 cm^{-1}) in Si-O-Si ring link increased simultaneously. This result means that for SiOC(-H) composite film, annealing at 200, 300 and 400 ℃ for 30 minutes in a vacuum induces the rearrangement of chemical bonds in the film. From the results, we know that for SiOC(-H) film, the post-annealing treatment induces the rearrangement of chemical bonds in the film. Therefore, void spaces can be formed, and the voids can be filled easily by other open links. We infer that this transformation of bonding mode is responsible for the formation of the nano-size void in the film. As previously mentioned, voids formed in film can result in a low dielectric constant [68].

제주대학교 중앙도서관
JEJU NATIONAL UNIVERSITY LIBRARY

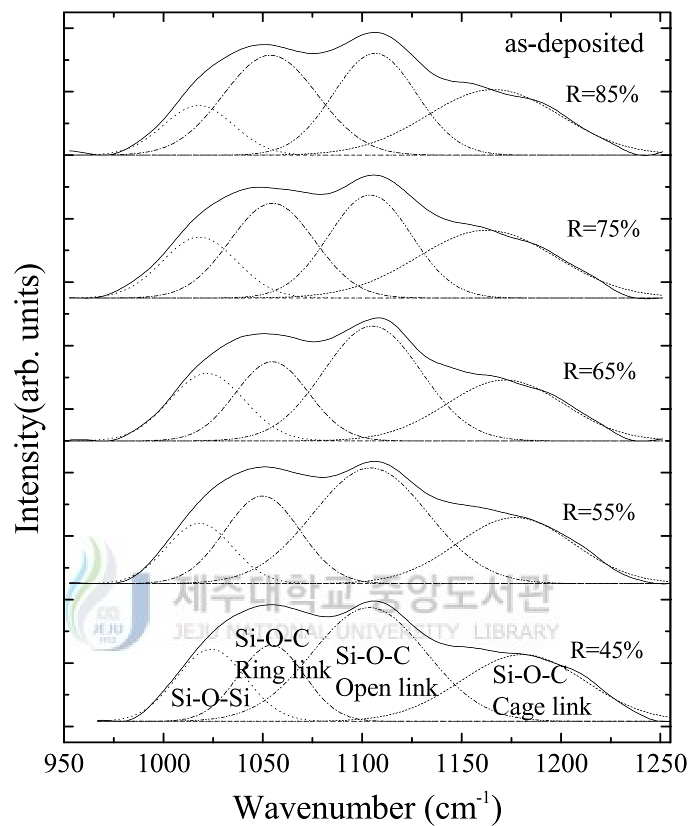

제주대학교 중앙도서관
JEJU NATIONAL UNIVERSITY LIBRARY

Fig. 21. Deconvolution of Si-O-C bonding mode in the wavenumber range 950~1250 cm^{-1} of the same sample Fig. 17.

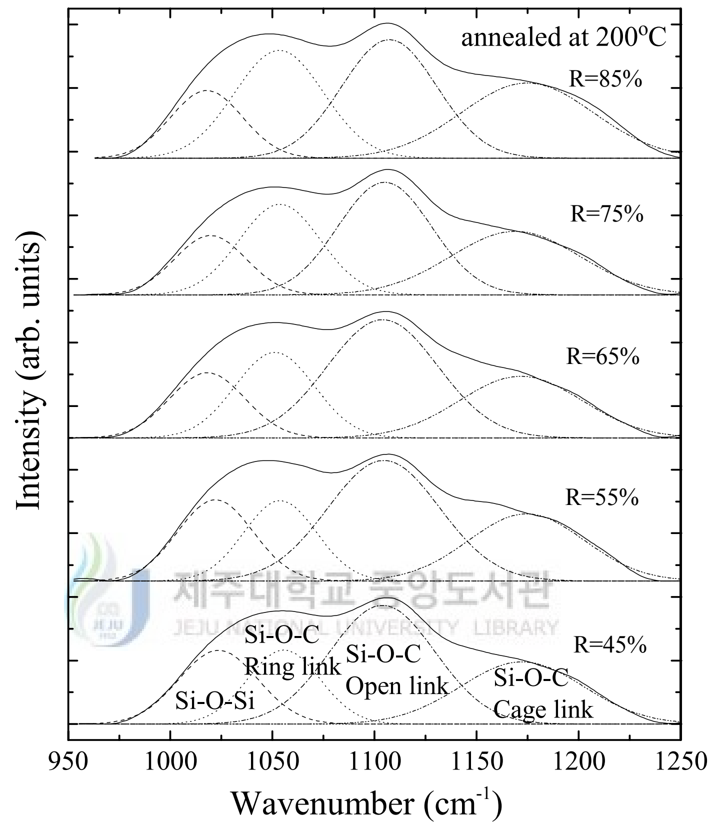

제주대학교 중앙도서관
JEJU NATIONAL UNIVERSITY LIBRARY

Fig. 22. Deconvolution of Si-O-C bonding mode in the wavenumber range 950~1250 cm^{-1} of the same sample Fig. 18.

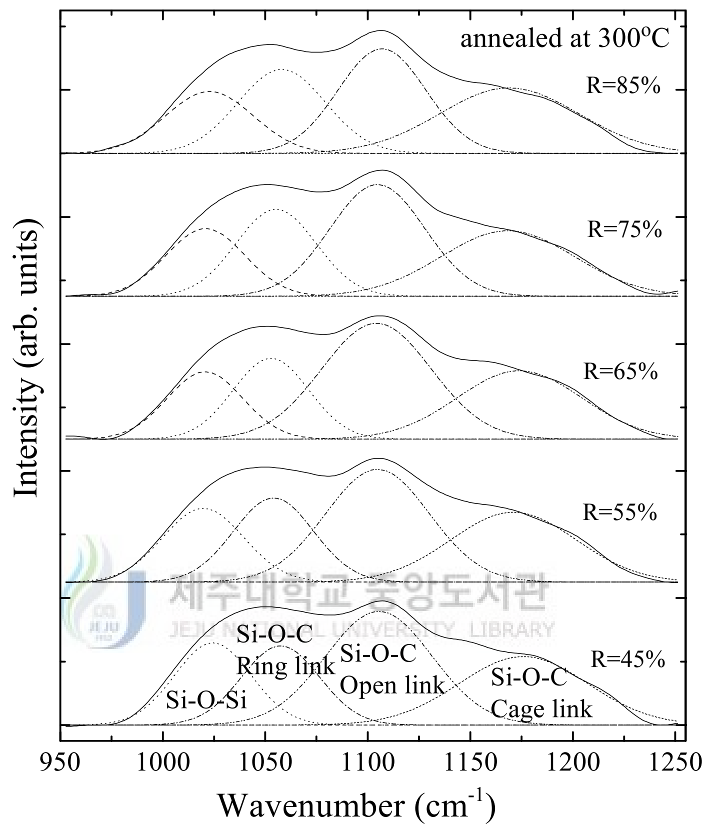

제주대학교 중앙도서관
JEJU NATIONAL UNIVERSITY LIBRARY

Fig. 23. Deconvolution of Si-O-C bonding mode in the wavenumber range 950~1250 cm^{-1} of the same sample Fig. 19.

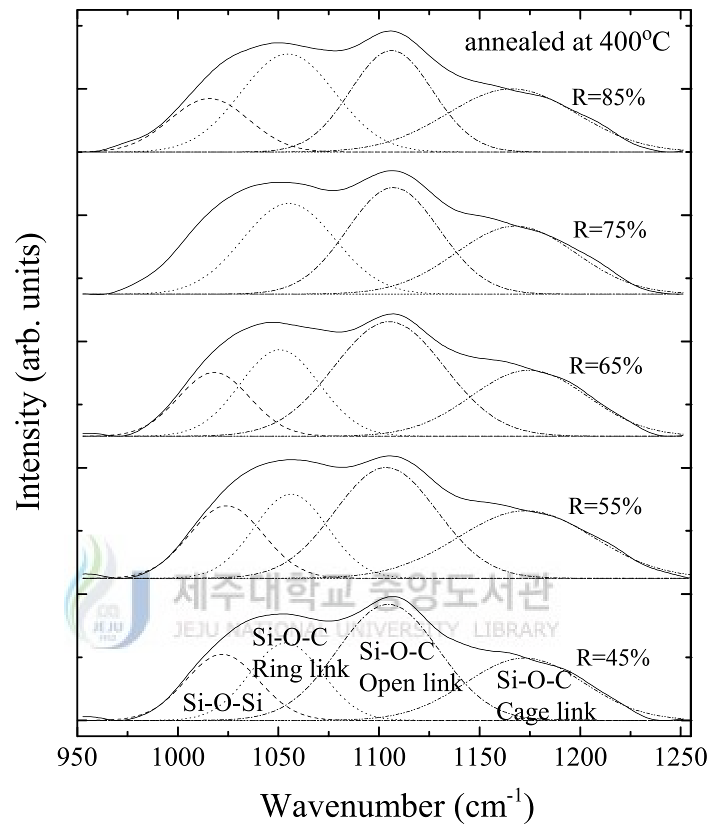

제주대학교 중앙도서관
JEJU NATIONAL UNIVERSITY LIBRARY

Fig. 24. Deconvolution of Si-O-C bonding mode in the wavenumber range 950~1250 cm^{-1} of the same sample Fig. 20.

In order to clearly understand the various structural properties of SiOCH thin films, the FTIR spectrum was deconvoluted between 950 and 1250 cm^{-1}. We carefully analyzed the bonding configuration in the deconvoluted region for as-deposited and annealed SiOC(-H) films. Here we discuss the peak position and relative peak area of Si-O-C and Si-O-Si bonding structures for the film deposited with BTMSM/(O_2+BTMSM) flow rate ratios of 45, 55, 65, 75 and 85 %. Figures 25 and 26 show the peak positions and relative peak areas as a function of flow rate ratio for as-deposited and annealed SiOC(-H) films, respectively. Fig. 25 clearly illustrates the corresponding peak position of Si-O-Si, Si-O-C ring-link, Si-O-C open-link and Si-O-C cage-link for the SiOC(-H) films with different flow rate ratios for as-deposited as well as annealed samples. It is interesting to note that the peak position of Si-O-Si asymmetric stretching mode decreased from 1024 to 1017 cm^{-1} resulting in a blue shift, while the corresponding relative peak area decreased about 6.4 % for the annealed films with flow rate ratios from 45 to 85 %. By contrast, red shift is observed for the Si-O-C asymmetric stretching mode for ring-linked forms and Si-O-C exhibited an increase of peak position from 1050 to 1056 cm^{-1} and the corresponding relative peak area increased about 13.2 %. In the case of Si-O-C asymmetric stretching mode with open link structure, there is an increase in peak position from 1103 to 1161 cm^{-1}, but the corresponding relative peak area was observed to decrease about 12.2 %.

제주대학교 중앙도서관
JEJU NATIONAL UNIVERSITY LIBRARY

At the same time, the Si-O-C cage link stretching mode structure shows a decrease in peak position from 1180 to 1161 cm^{-1} and the corresponding relative peak area decreased about 2.4 % for the as-deposited and annealed films with flow rate ratio from 45 to 85 %. Therefore, from the results of Fig. 26, it is observed that the annealed SiOC(-H) with flow rate ratio of 85 % shows an increase of Si-O-C asymmetric stretching mode in ring-link form of about 2.5 % and a decrease of Si-O-C asymmetric stretching mode in open-link form of about 2.4 %. The frequency shifts in FTIR spectra are related to the change of bonding characteristics, such as bonding structure and bond length variation in the SiOC(-H) film as a result of the annealing process. During the annealing process, the chain network of Si-O-Si link structures is broken and some of the Si-O-Si bonds change into Si-O-C bonds in the form of rings as well as open-link structures in which the C atoms have been incorporated. From these results, we know that the Si-O-C ring-link mode increases during the post-annealing procedure as the flow rate ratio increases, and that Si-O-C open-linked substructures are unstable. Therefore, the bonding structure of the SiOC(-H) film is changed due to the post-annealing and the flow rate ratio increases, which suggest a transformation from open-linked to ring-linked substructure. We infer that this transformation of bonding mode is responsible for the formation of the nano-size void in the film.

제주대학교 중앙도서관
JEJU NATIONAL UNIVERSITY LIBRARY

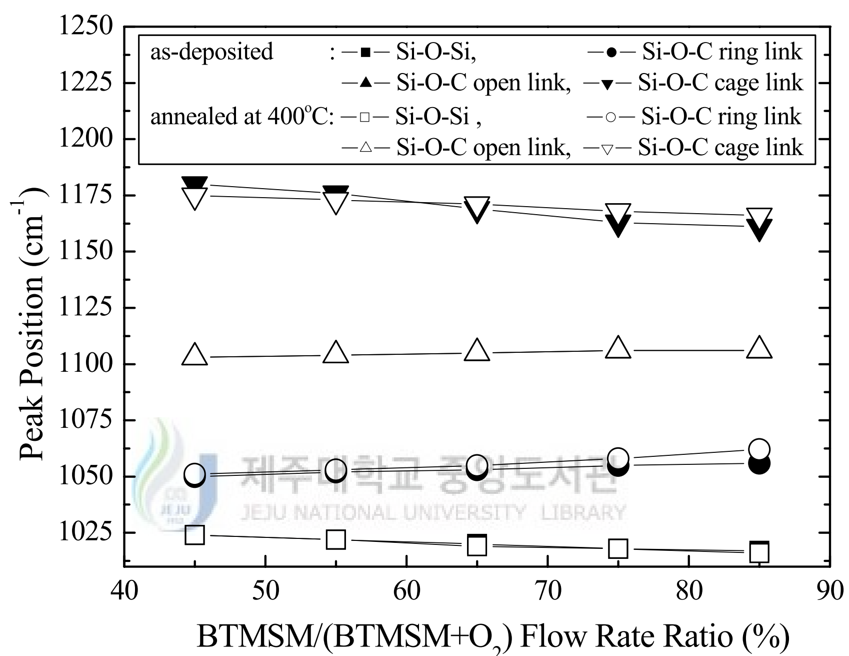

제주대학교 중앙도서관
JEJU NATIONAL UNIVERSITY LIBRARY

Fig. 25. The peak position of Si-O-C ring link of spectrum between 950 cm^{-1} and 1250 cm^{-1} for the resulted fitted peaks as-deposited and annealed SiOC(-H) composite films at 200, 300 and 400℃ with various BTMSM/(O_2+ BTMSM) flow rate ratios.

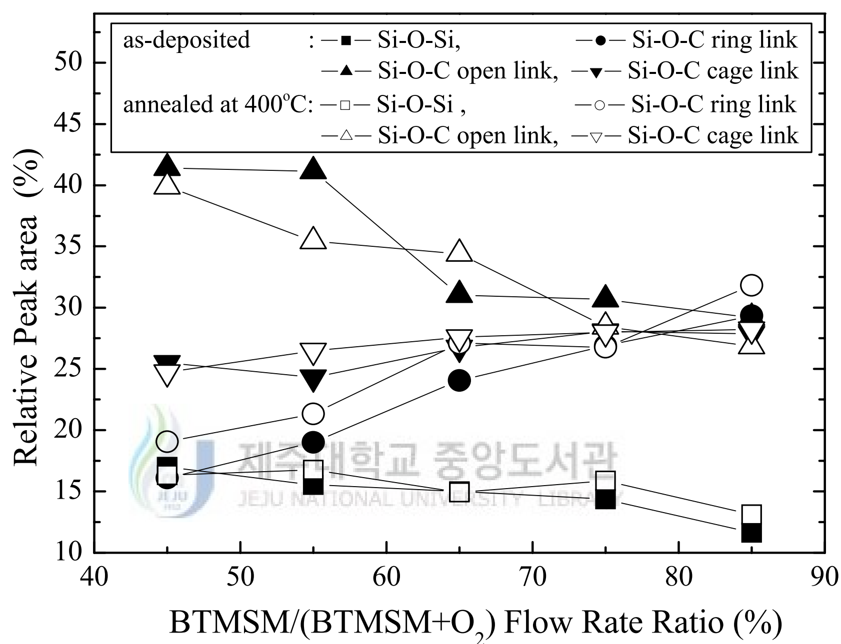

제주대학교 중앙도서관
JEJU NATIONAL UNIVERSITY LIBRARY

Fig. 26. The relative integrated absorption area (peak area/total area of spectrum between 950 cm^{-1} and 1250 cm^{-1}) for the resulted fitted peaks from Fig. 17~20, as-deposited and annealed SiOC(-H) composite films at 400℃ with various BTMSM/(O_2+BTMSM) flow rate ratios.

Figure 27 shows the relation of the carbon concentration of as-deposited and composite SiOC(-H) films annealed at 200, 300 and 400 ℃ with various BTMSM/(O_2+BTMSM) flow rate ratios. It is well known that the dielectric constant decreases with increasing -CH_3. The concentration of carbon incorporated in SiOC(-H) composite films was calculated by the following equation normalized to the peak area of the Si-O-C stretching mode. The relative carbon concentration is calculated from the formula

$$\frac{A_C}{A_C+A_O}\times 100(\%) \tag{4-1}$$

where A_O and A_C are the sum of peak areas of the Si-O-C stretching vibration mode from 950 to 1250 cm^{-1} and the Si-CH_3 stretching vibration mode at 888 cm^{-1} and 1273 cm^{-1}, respectively. The carbon concentration of as-deposited films and annealed films increases as the flow rate ratio increases: 7.4 to 14 % (as-deposited), 7.9 to 13.7 % (annealed at 200 ℃), 8.9 to 12.8 % (annealed at 300 ℃), 9.2 to 12.9 % (annealed at 400 ℃). Therefore, we infer that this transformation of bonding mode is responsible for the formation of the nano-size void in the film. The void formed in the film can result in a low dielectric constant.

We investigated the bonding angle of as-deposited and SiOC(-H) composite films annealed at 200, 300 and 400 ℃ with various BTMSM/(O_2+BTMSM) flow rate ratios. The bonding angles between Si-O and Si-C bonds are shown in Fig. 28. The bonding angle, θ can be calculated from the following simple equation [75]:

$$\overline{\nu} = \overline{\nu_0}\sin\left(\frac{\theta}{2}\right) \tag{4-2}$$

제주대학교 중앙도서관 JEJU NATIONAL UNIVERSITY LIBRARY

where θ is the bonding angle between the Si-O and the Si-C bonds. $\bar{\nu}$ is experimentally obtained from the wavenumber of the Si-O-C ring link in Fig. 25, and $\bar{\nu}_0$=1080 cm^{-1} being the wavenumber for the thermal oxide (SiO_2). The bonding angle between the Si-O and the Si-C bonds increased as the flow rate ratios increased and the annealing temperature increased. The bonding angle of as-deposited films range from 152.9 to 155.8 and that of films annealed at 400 ℃ are from 153.4 to 159.0, respectively. The incorporation of CH_3 groups breaks the continuity of Si-O-Si networks and causes nano-pores to be formed due to the aloof force between the CH_3 group and other parts of Si-O-Si links. The repulsive force between Si-O and Si-O bonds is smaller than that between Si-O and Si-C bonds in the [SiO_3C] tetrahedron due to the electronegativity of carbon atoms (2.5) being lower than that of oxygen atoms (3.5). Therefore, the bonding angle of O-Si-O is less than 120 in the [SiO_3C] tetrahedron.

제주대학교 중앙도서관
JEJU NATIONAL UNIVERSITY LIBRARY

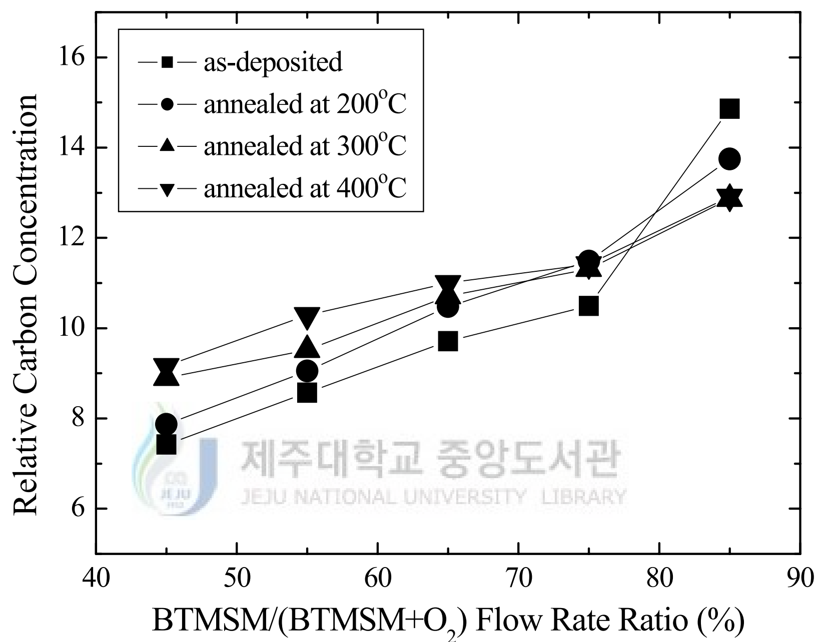

Fig. 27. The relation of the carbon concentration of as-deposited and annealed SiOC(-H) composite films at 200, 300 and 400 ℃ with various BTMSM/(O_2+BTMSM) flow rate ratios.

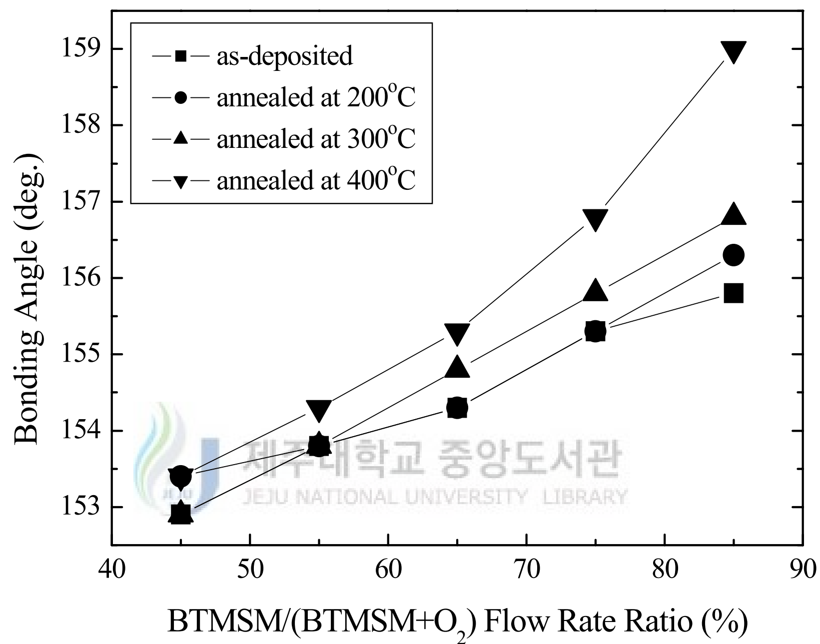

제주대학교 중앙도서관
JEJU NATIONAL UNIVERSITY LIBRARY

Fig. 28. The bonding angle of SiOC(-H) composite films, as-deposited and annealed at 200, 300 and 400 ℃ with various BTMSM/(O_2+BTMSM) flow rate ratios.

In order to understand the bonding configurations of Si-CH_3 and CH_3 related structures, we have deconvoluted the FTIR spectra in the region between 700 and 950 cm^{-1}. The detailed data of deconvoluted FTIR spectra for as-deposited and annealed SiOC(-H) films with flow rate ratios of 45, 55, 65, 75 and 85 % are shown in Fig. 29~32. Si-O-Si and $SiOCH_3$ bonds appeared in the dominant peaks. From the results of the deconvoluted data, the related peak positions are assigned as follows; Si-O-Si bond was assigned as 738 cm^{-1} Si-C bond was assigned as 767 cm^{-1} Si-C and Si-CH_3 bonds were assigned as 790 cm^{-1} Si-O and Si-CH_x bonds were assigned as 820 cm^{-1} $SiOCH_3$ bonds were assigned as 890 cm^{-1} and H-Si-O bonds were assigned as 848, 870 and 920 cm^{-1}, respectively. The decrease in Si-CH_3, CH_3 bonds with annealing match the decreased density very well because the CH_3 bonds in as-deposited film react easily with OH-related bonds during the annealing process [17].

제주대학교 중앙도서관
JEJU NATIONAL UNIVERSITY LIBRARY

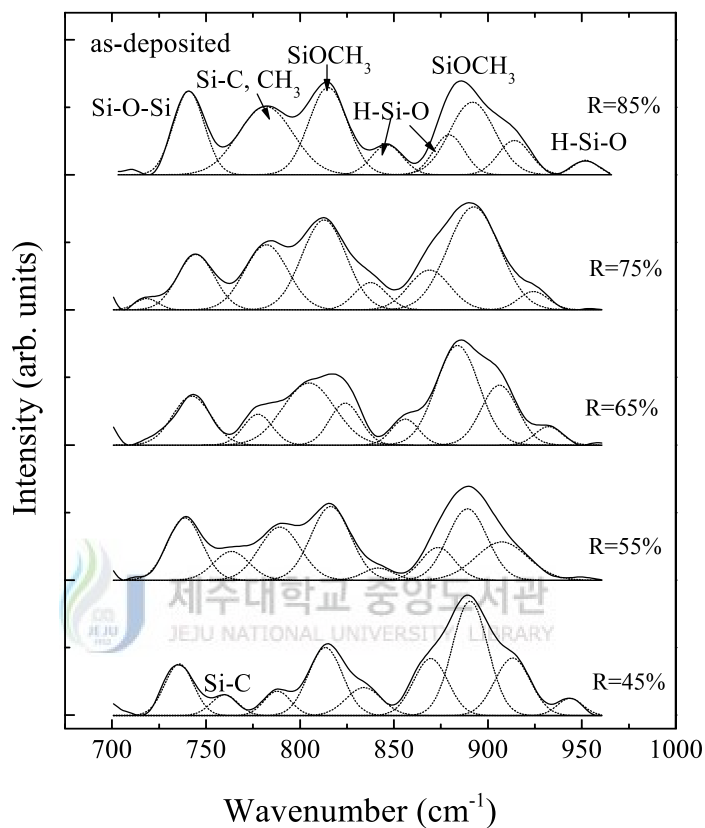

제주대학교 중앙도서관
JEJU NATIONAL UNIVERSITY LIBRARY

Fig. 29. Deconvolution of spectra in the wavenumber range 700~950 cm^{-1} of the same sample Fig. 17.

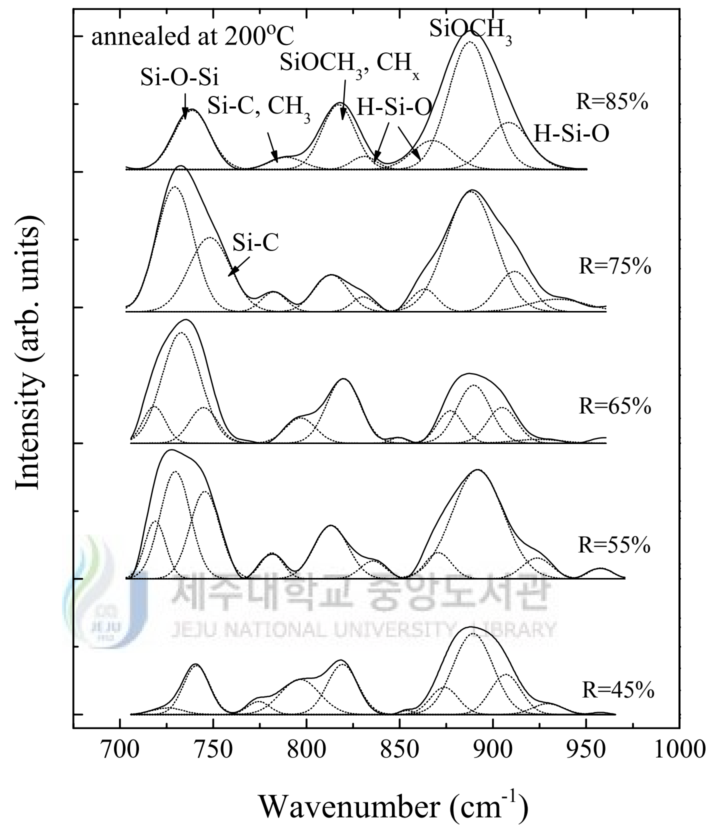

제주대학교 중앙도서관
JEJU NATIONAL UNIVERSITY LIBRARY

Fig. 30. Deconvolution of spectra in the wavenumber range 700~950 cm^{-1} of the same sample Fig. 18.

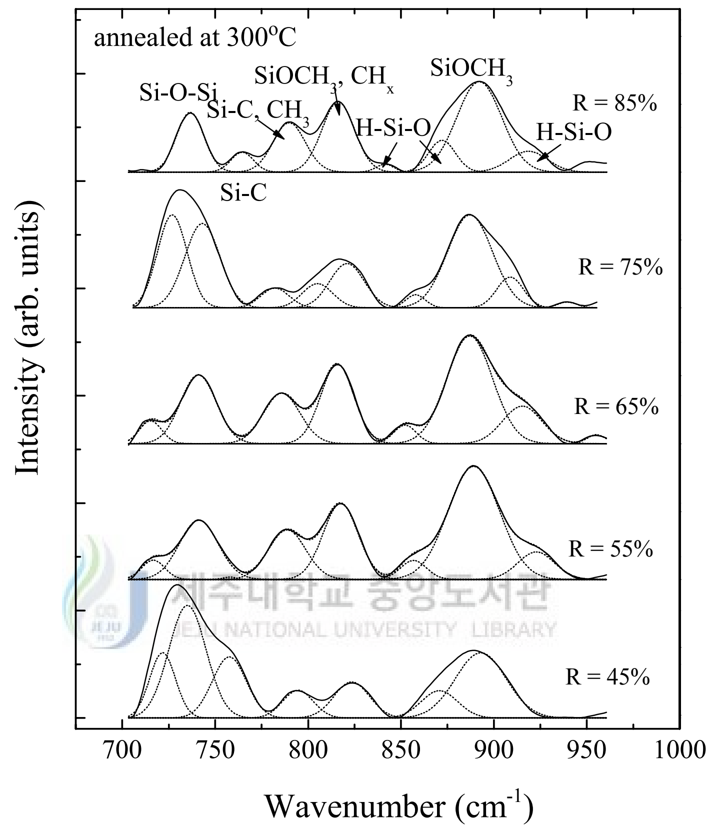

제주대학교 중앙도서관
JEJU NATIONAL UNIVERSITY LIBRARY

Fig. 31. Deconvolution of spectra in the wavenumber range 700~950 cm^{-1} of the same sample Fig. 19.

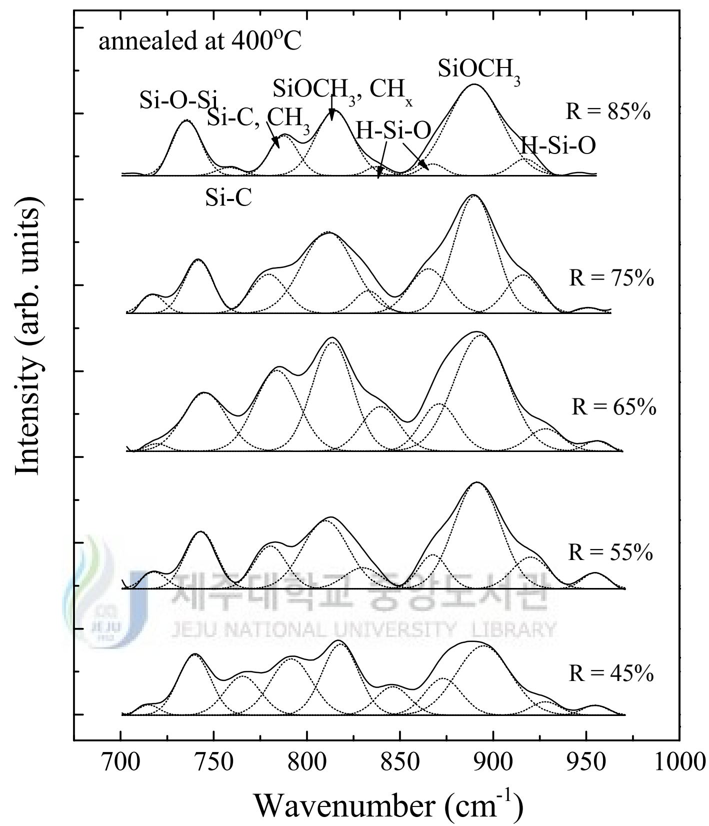

제주대학교 중앙도서관
JEJU NATIONAL UNIVERSITY LIBRARY

Fig. 32. Deconvolution of spectra in the wavenumber range 700~950 cm^{-1} of the same sample Fig. 20.

In order to understand the bonding configurations of Si-CH_3 and CH_3 related structures at higher wavenumber regions, we have deconvoluted the FTIR spectra in the region between 2850 and 3050 cm^{-1}. The detailed data of deconvoluted FTIR spectra of as-deposited and annealed SiOC(-H) films with flow rate ratios of 45, 55, 65, 75and 85 % are shown in Fig. 33~36. From the detailed deconvolution analysis of FTIR spectra the following peak positions are assigned; CH bond is assigned as 3005 cm^{-1} CH_2 bond is assigned as 2938 cm^{-1} and CH_3 bonds are assigned as 2920, 2960 and 2985 cm^{-1}, respectively. The CH_x bond was observed to increase as the flow rate ratio increased and after annealing the SiOC(-H) films, the intensity of CH_x was found to decrease. Therefore, the decrease in Si-CH_3, CH_3 bonds along with the decrease in density is matches the annealing process well because the CH_3 bonds in as-deposited film react easily with OH related bonds during the annealing process.

제주대학교 중앙도서관
JEJU NATIONAL UNIVERSITY LIBRARY

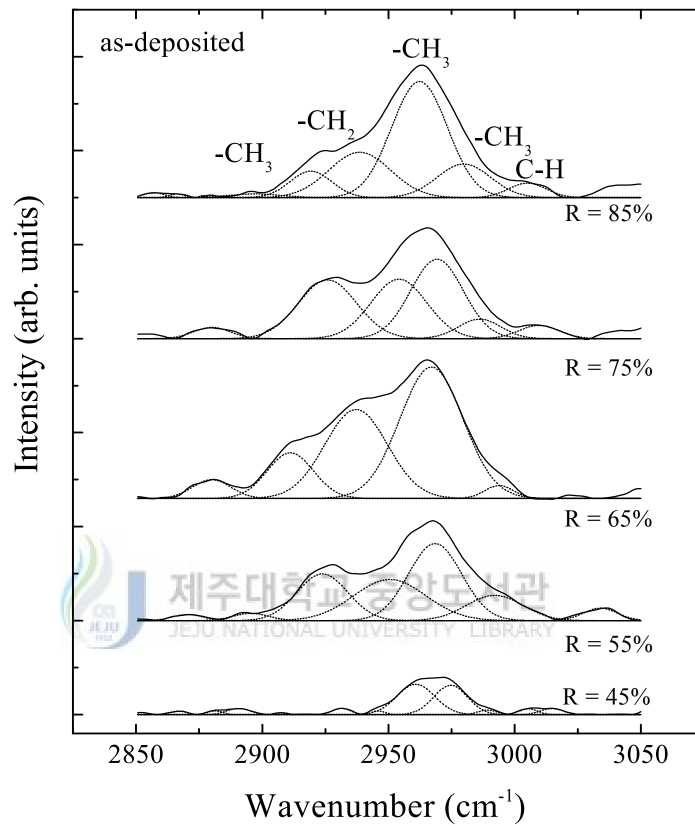

제주대학교 중앙도서관
JEJU NATIONAL UNIVERSITY LIBRARY

Fig. 33. Deconvolution of spectra in the wavenumber range 2850~3050 cm^{-1} of the same sample Fig. 17.

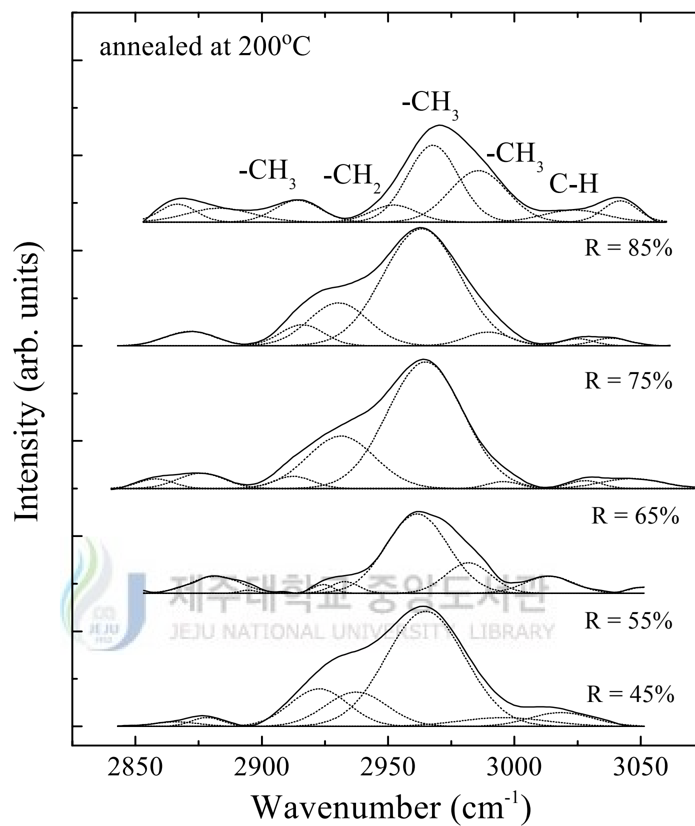

제주대학교 중앙도서관
JEJU NATIONAL UNIVERSITY LIBRARY

Fig. 34. Deconvolution of spectra in the wavenumber range 2850~3050 cm^{-1} of the same sample Fig. 18.

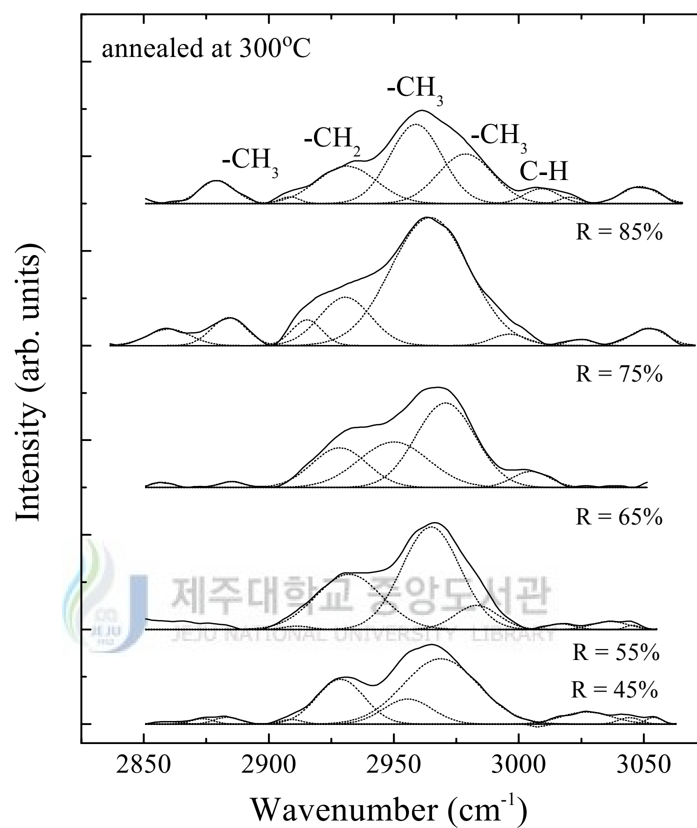

제주대학교 중앙도서관
JEJU NATIONAL UNIVERSITY LIBRARY

Fig. 35. Deconvolution of spectra in the wavenumber range 2850~3050 cm^{-1} of the same sample Fig. 19.

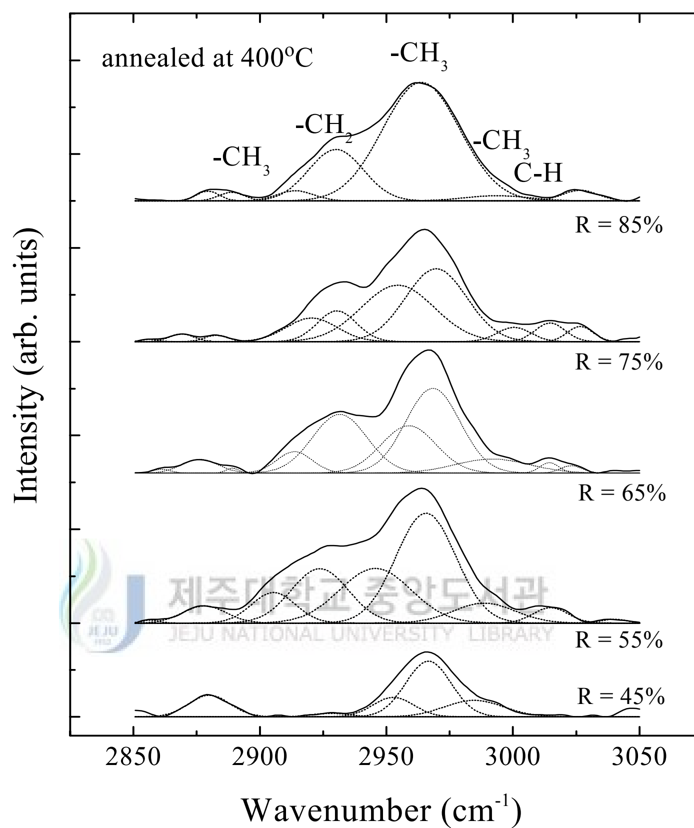

제주대학교 중앙도서관
JEJU NATIONAL UNIVERSITY LIBRARY

Fig. 36. Deconvolution of spectra in the wavenumber range 2850~3050 cm^{-1} of the same sample Fig. 20.

2) Binding energy of SiOC(-H) films

Figures 37~39 shows the O 1s, Si 2p, and C 1s XPS spectra of as-deposited and annealed samples at 400 ℃ for 30 min. in vacuum. All these peaks were resolved by Gaussian fitting. The O 1s XPS spectra consists of two peaks, which can be assigned as O-Si (532.6 eV) and O-C bonds (530.6 eV) in Fig. 37 [76]. After annealing, the C-O band intensity is a little bit higher than that of as-deposited film, meaning there are much more Si-O-C bonds formed during the annealing process. The Si 2p spectrum of as-deposited film consists of two peaks, which can be assigned as Si-O_4 (103.0 eV) and C-Si-O_3 bonds (101.0 eV), while for the annealed sample it consist of three peaks assigned as Si-O_4 (103.1 eV), C-Si-O_3 (101.3 eV) and C_2-Si-O_2 bonds (99.4 eV) in Fig. 38 [76]. The C 1s spectrum of as-deposited film consist of one broad peak with FWHM of 3.2 eV, while the spectrum of annealed film consists of two peaks with FWHM of about 1.6 eV and 1.9 eV, with one being a C-O/H bond (284.2 eV) and the other being a Si-C bond (282.2 eV). These results also show that there are many more C atoms incorporated into the Si-O link forming the Si-O-C link in Fig. 39.

제주대학교 중앙도서관
JEJU NATIONAL UNIVERSITY LIBRARY

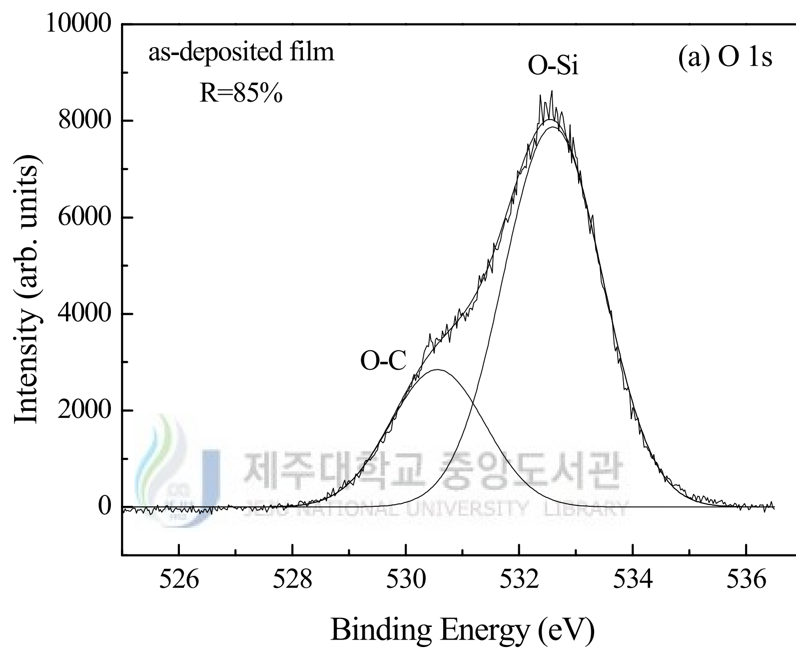

제주대학교 중앙도서관
JEJU NATIONAL UNIVERSITY LIBRARY

Fig. 37. The O 1s XPS spectra of (a) as-deposited sample and (b) annealed sample with a flow rate ratio of 85 % at 400 ℃ for 30 min in a vacuum.

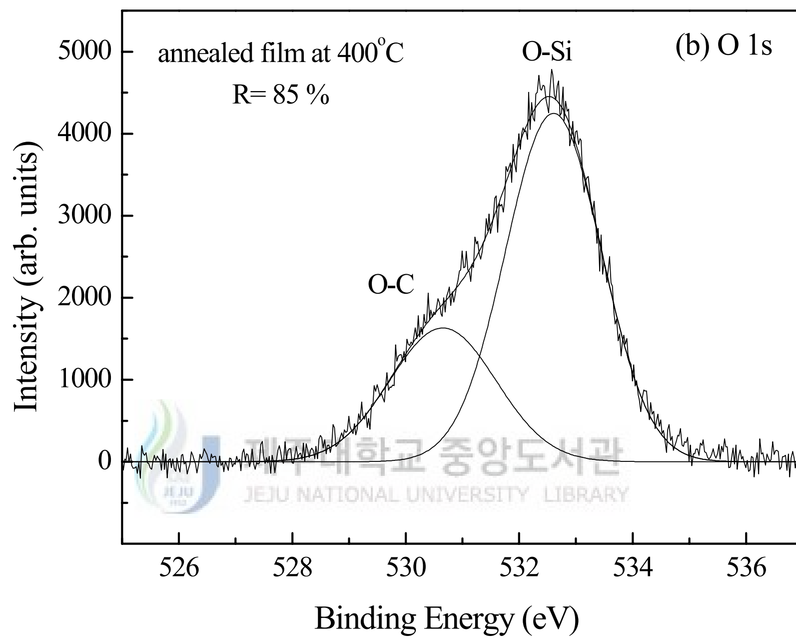

제주대학교 중앙도서관
JEJU NATIONAL UNIVERSITY LIBRARY

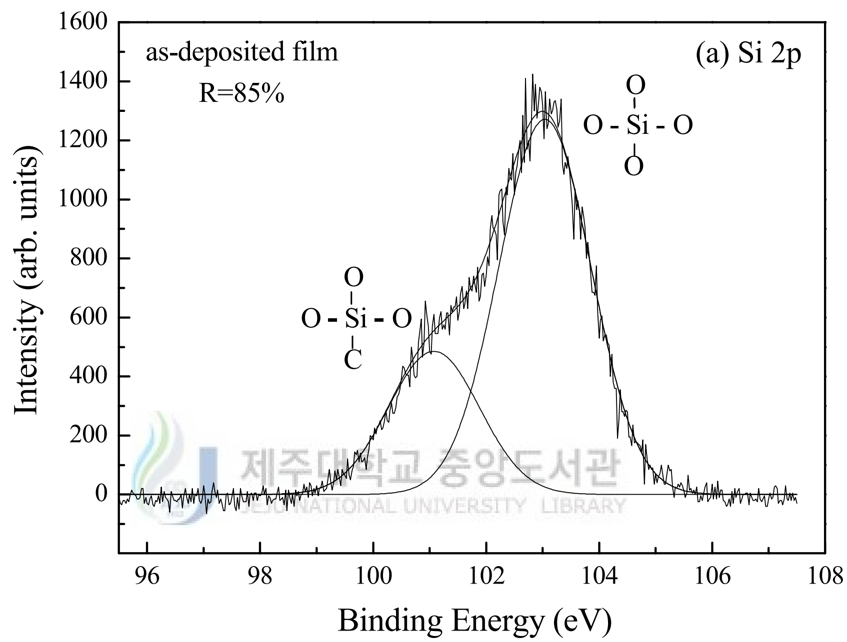

제주대학교 중앙도서관
JEJU NATIONAL UNIVERSITY LIBRARY

Fig. 38. The Si 2p XPS spectra of an (a)as-deposited sample and (b)annealed sample with a flow rate ratio of 85 % at 400 ℃ for 30 min in a vacuum.

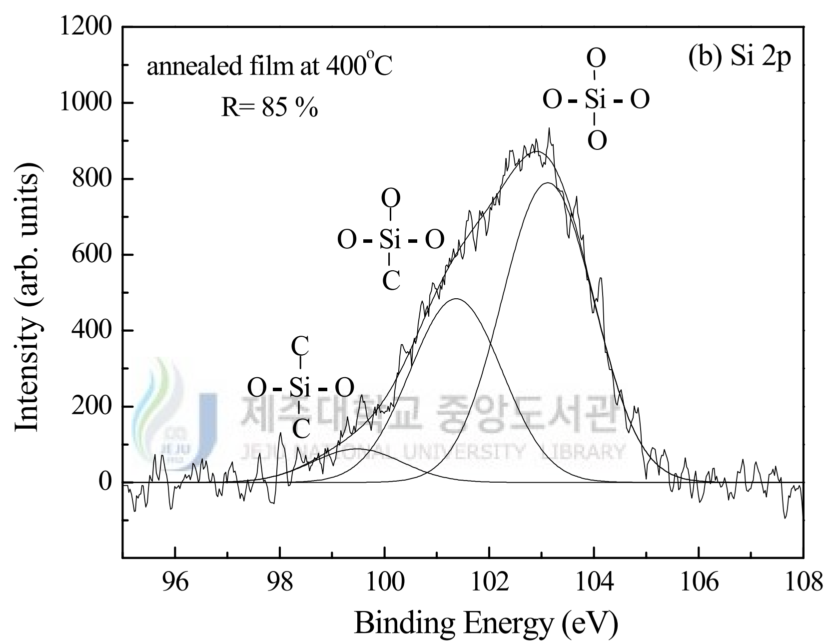

제주대학교 중앙도서관
JEJU NATIONAL UNIVERSITY LIBRARY

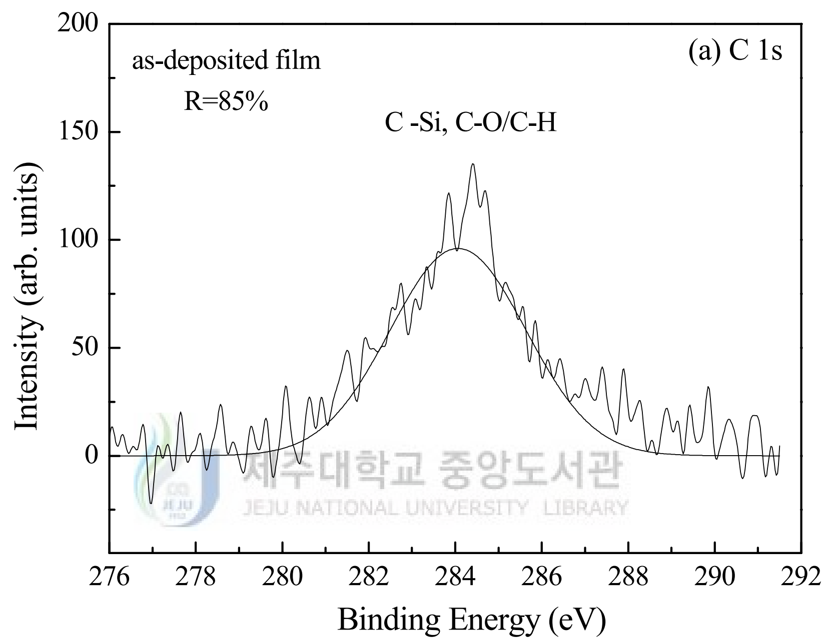

제주대학교 중앙도서관
JEJU NATIONAL UNIVERSITY LIBRARY

Fig. 39. The C 1s XPS spectra of an (a) as-deposited sample and (b)annealed sample with a flow rate ratio of 85 % at 400 ℃ for 30 min in a vacuum.

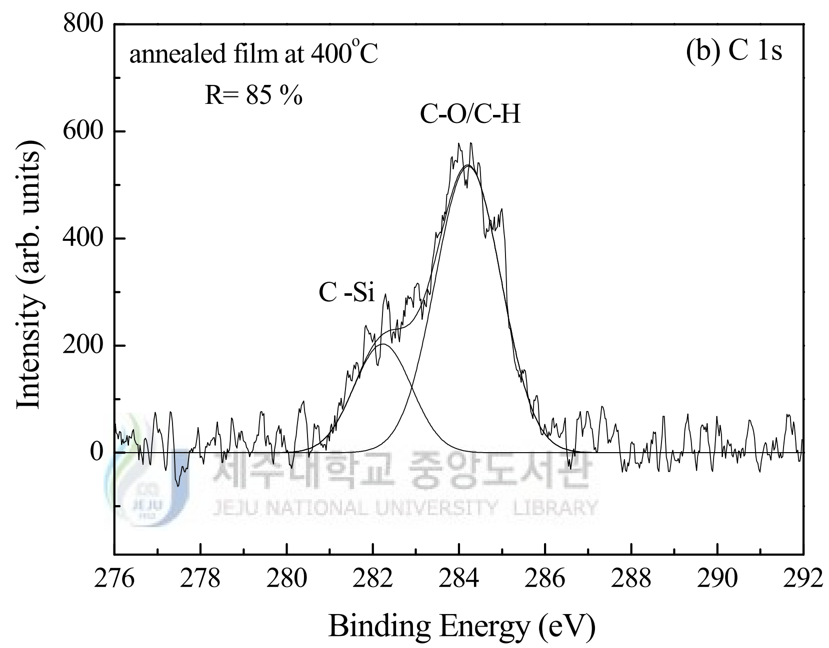

제주대학교 중앙도서관
JEJU NATIONAL UNIVERSITY LIBRARY

To confirm the O-Si-O, Si-C, C-H and C-O bonds in the film, the XPS narrow scan spectrum of the Si 2p and C 1s peaks with R=65, 75, 85 % are deconvoluted by fitting the data with a number of Gaussian peaks annealed at 400 ℃. The results are shown in Figs. 40 and 41. The Si 2p 1s electron orbital spectra (see Fig.40) consists of two peaks, which can be assigned as Si-O_4 and C-Si-O_3 bonds. By increasing the flow rate ratio, binding energy of Si-O_4 bonds are chemically shifted to the lower binding energy side such as : 103.5 eV (R=65 %), 103.4 eV (R=75 %) and 103.1 eV (R=85 %), while that of C-Si-O_3 bonds are shifted to the higher binding energy side such as : 101.1 eV (R=65 %), 101.2 eV (R=75 %) and 101.2 eV (R=85 %). Also the relative area of Si-O_4 bonds decreases from 68.4 to 64.5 % when the flow rate ratio increases from 65 to 85 %. But the relative area of C-Si-O_3 bonds increases from 31.6 to 35.5 % as the flow rate ratio increases. This result means that some bonds such as Si-O_4 have broken and that parts of O atoms are being replaced by C and H atoms, or are being removed from this film, resulting in those atoms appearing in different chemical states and in some voids formed in the film. Such binding energy changes can be explained by the oxidation states of silicon atoms. The electronegativity of carbon is lower than that of oxygen atoms. When carbon in C-Si is replaced by O-Si-O, the binding energy of C-Si-O_3 bonds shifts to higher energy levels. It is conjectured that Si 2p is related to different oxidation states of Si atoms. Si-O bonds have an energy status between C-Si-O and O-Si-O bonding states.

Figure 41 shows that the C 1s electron orbital spectra consists of three peaks, which can be assigned as C-H, C-Si and -C-O bonds. By increasing the flow rate ratio, binding energy of C-H bonds doesn't change much. But C-Si bonds are

제주대학교 중앙도서관
JEJU NATIONAL UNIVERSITY LIBRARY

chemically shifted towards the lower binding energy side such as : 286.3 eV (R=65 %), 286.1 eV (R=75 %) and 285.9 eV (R=85 %) and that of -C-O bonds are also shifted to the lower binding energy side such as : 288 eV (R=65 %), 287.9 eV (R=75 %) and 287.8 eV (R=85 %). The relative area of C-H bonds decreases from 12.4 to 7.7 % and that of C-Si bonds also decreases from 41 to 26.4 % when the flow rate ratio increases from 65 to 85 %. But the relative area of -C-O bonds increases from 46.6 to 65.9 % as the flow rate ratio increases. These results also show that there are many more C atoms integrated into the Si-O links that form the Si-O-C links, which means some of the Si-CH_3 groups have reacted with OH-related bonds.

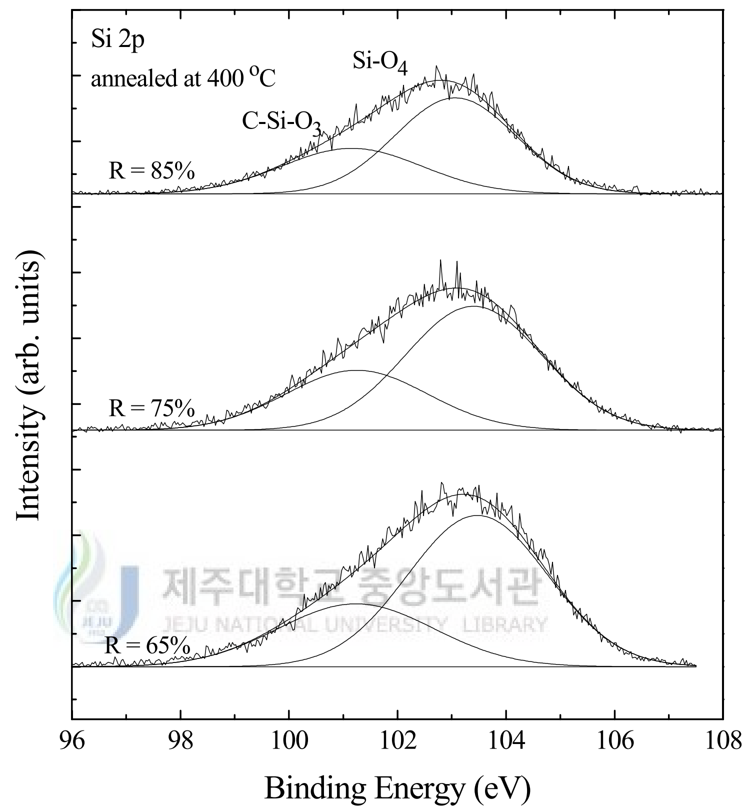

제주대학교 중앙도서관
JEJU NATIONAL UNIVERSITY LIBRARY

Fig. 40. The Si 2p XPS spectra of an annealed sample with flow rate ratios of 65, 75 and 85 % at 400 ℃ for 30 min in a vacuum.

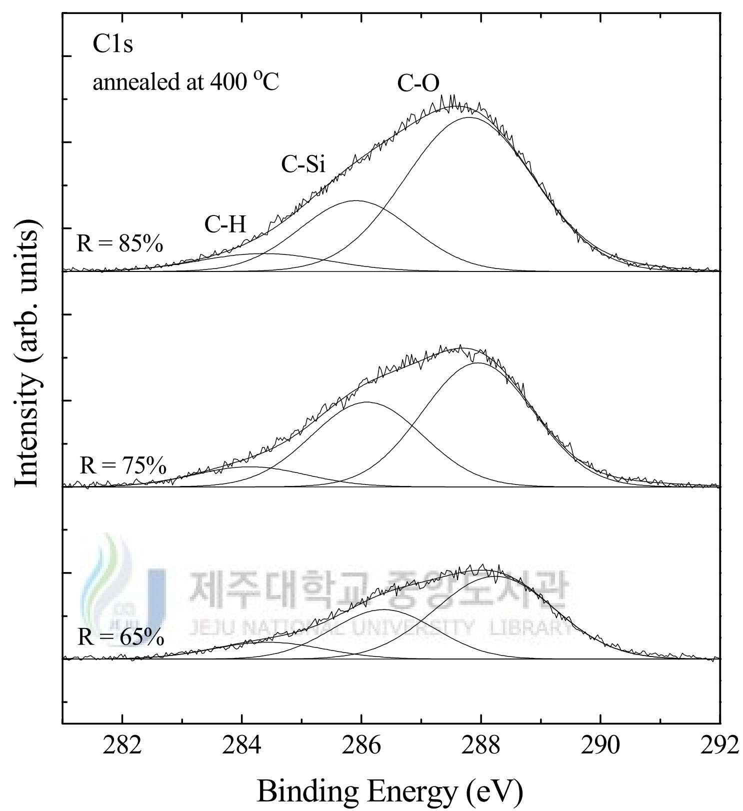

제주대학교 중앙도서관
JEJU NATIONAL UNIVERSITY LIBRARY

Fig. 41. The C 1s XPS spectra of an annealed sample with flow rate ratios of 65, 75 and 85 % at 400 ℃ for 30 min in a vacuum.

2. Nano-pore structure

1) The pore size and size distribution

The size distribution of pores was investigated by means of SANS. The shape of nano pores in film can be assumed as spherical [77]. The scattering length density was calculated with the assumption that voids smaller than 50 nm are dispersed equally. The size distribution function for spherical centers is given by

$$N(R) = \sum_i N_{0i} \exp\left[-0.5 \left(\frac{\ln(R) - \ln(R_{0i})}{S_i} \right)^2 \right] \qquad (4\text{-}3)$$

where the unknown parameters N_0, R_0 and S are the standard scaling factor, center and width parameters of this distribution type, respectively. These lognormal distributions were fitted with the non-linear least-squares fitting program SANSFITTCL for the range of Q from 0.01 to 0.25 $Å^{-1}$ [55～57].

제주대학교 중앙도서관
JEJU NATIONAL UNIVERSITY LIBRARY

The measured and fitted scattering intensities (I) versus scattering vector (Q) of as-deposited and annealed SiOC(-H) composite samples with a flow rate ratio of 5% are shown in Fig. 42. In this case the total film thickness was 500.0 nm. Figure 43 shows the number distribution of pores depends on their radius. The diameters of pores were distributed from 1.7 to 3.5 nm, and the average value was 2.5±0.2 nm. The peak value of the pore size distribution increased about 12% by annealing, but the average size of pores was almost unchanged. This means that the more equal-sized voids are produced in film by annealing and that a decrease in the dielectric constant is expected.

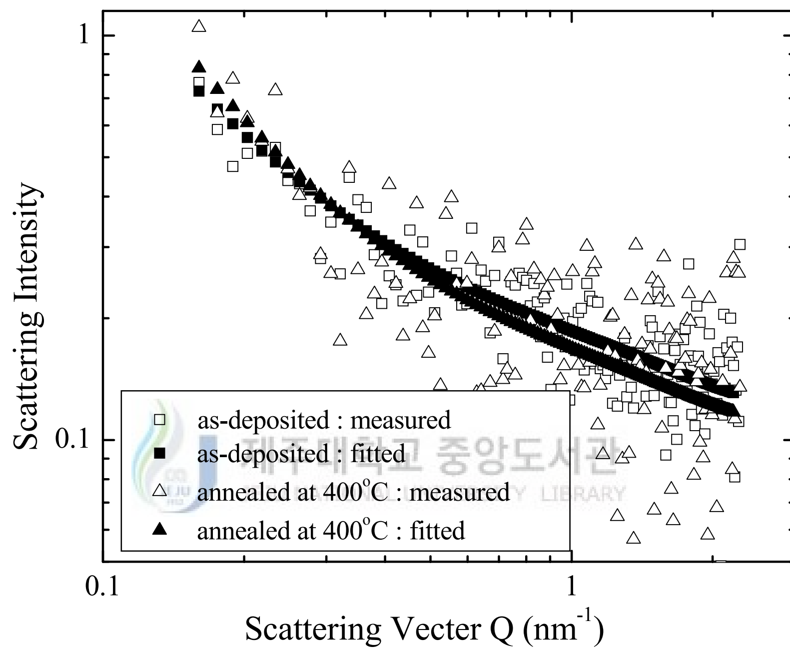

Fig. 42. Measured and fitted scattering intensities versus the scattering vector, Q of as-deposited and annealed SiOC(-H) composite films with BTMSM/ (O_2+ BTMSM) flow rate ratio of 85 %.

제주대학교 중앙도서관 LIBRARY

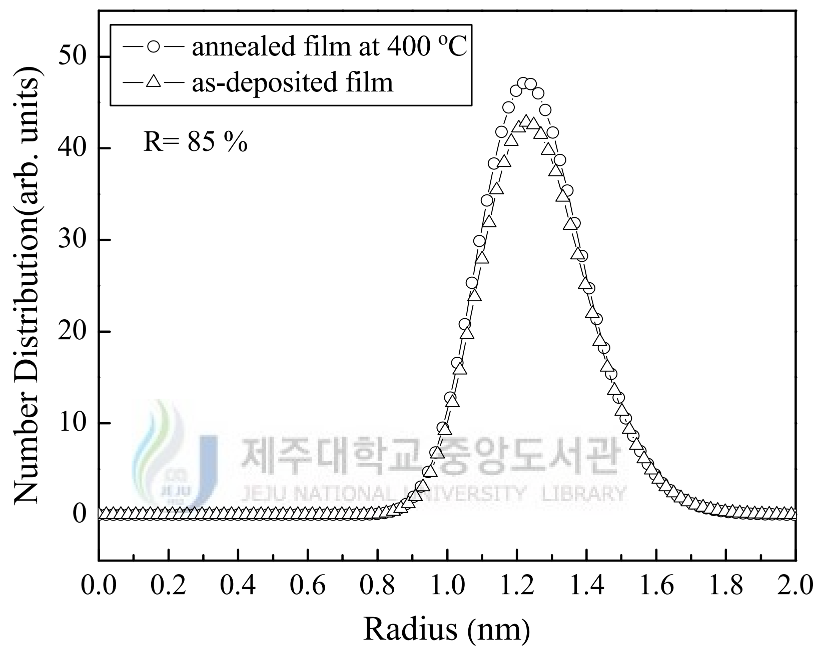

제주대학교 중앙도서관
JEJU NATIONAL UNIVERSITY LIBRARY

Fig. 43. Distribution of pores of as-deposited and annealed SiOC(-H) composite films with a BTMSM/(O_2+BTMSM) flow rate ratio of 85 % versus pore radius as measured by using the SANS method.

The generation mechanism of pores in the deposition process seems to resemble that of annealing. Unfortunately the porosity could not be deduced from SANS data because the calibration of the instrument was not fine enough.

The measured and fitted scattering intensities (I) versus scattering vector (Q) of SiOC(-H) films annealed at 400 ℃ with flow rate ratios of 65, 75 and 85 % are shown in Fig. 44. The SANS measurement determines the scattered intensities of neutrons with respect to the scattering angle, 2θ. After the effects of background noise have been discarded, the absolute scattering intensity is obtained. The data can be converted to I vs Q as shown in Fig. 44, by applying the relation $Q = 4\pi Sin\theta / \lambda$. Porosities of SiOC(-H) films increase as the BTMSM/(O_2+BTMSM) flow rate ratios increase, and the porosity changes from 49 to 62 % when the flow rate ratio is increased from 65 to 85 %. From the slope of Fig. 45, the pore size can be deduced. Figure 45 shows the distribution of pores with respect to radii for the flow rate ratios of 65, 75 and 85 %. The pore diameter ranged from 2.5 to 4.0 nm, and its average value was 2.2±0.2 nm.

제주대학교 중앙도서관
JEJU NATIONAL UNIVERSITY LIBRARY

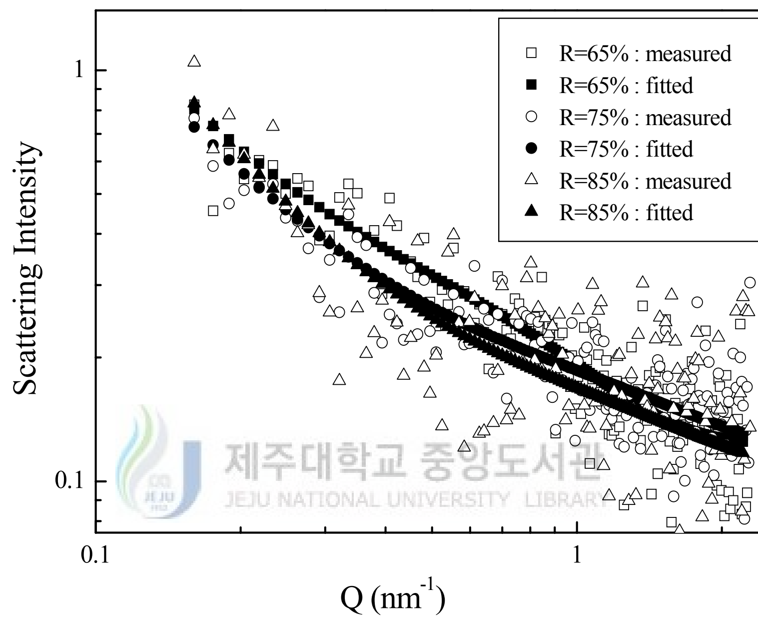

제주대학교 중앙도서관
JEJU NATIONAL UNIVERSITY LIBRARY

Fig. 44. Measured and fitted scattering intensities versus the scattering vector, Q of SiOC(-H) composite films annealed at 400 ℃ with various BTMSM/(O_2+BTMSM) flow rate ratios.

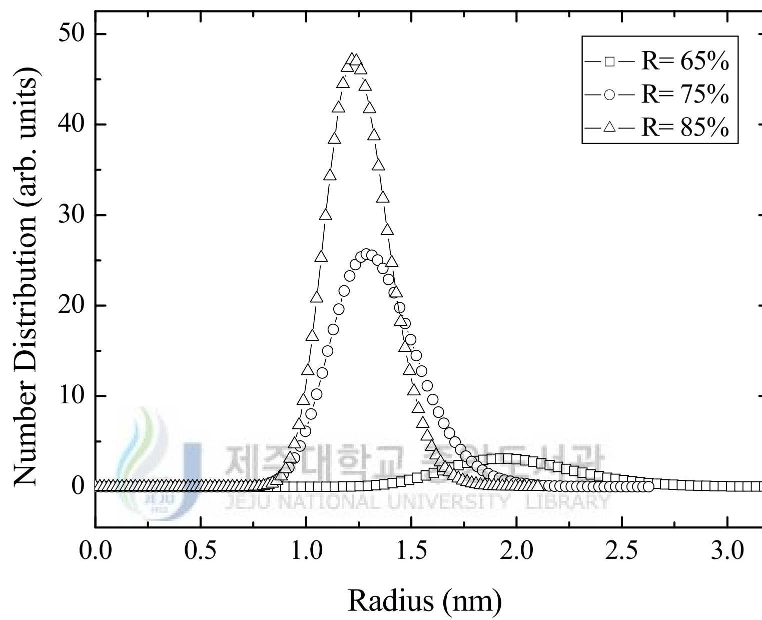

제주대학교 중앙도서관
JEJU NATIONAL UNIVERSITY LIBRARY

Fig. 45. Distribution of pores of SiOC(-H) composite films annealed at 400 ℃ with various BTMSM/(O_2+BTMSM) flow rate ratios, versus pore radius as measured by using the SANS method.

2) **GISAXS Analysis**

Grazing Incidence Small Angle X-ray Scattering (GISAXS) was carried out for SiOC(-H) films in order to examine the evolution of nano pores during the thin film formation of porous dielectrics. In this analysis, an incident X-ray beam impinges on the surfaces of a thin film at an angle and then the scattered pattern is measured on a two-dimensional charge coupled detector. The GISAXS technique has several important advantages over other methods, which includes; (1) a highly intense scattering pattern is always obtained, even for films of nanoscale thickness, because the X-ray beam path length through the film plane is sufficiently long, (2) there is no unfavorable scattering from the substrate on which the film is coated and (3) easy sample preparation [79]. In the present study we have carried out pore size and size distribution analysis of SiOC(-H) low–*k* dielectrics deposited with a flow rate ratio BTMSM/(0_2+BTMSM) of 55 % by GISAXS. As seen in Fig. 46, the extracted in-plane GISAXS scattering profiles of the porous SiOC(-H) thin films imprinted with annealed films at 400 ℃ shows a good fit with the GISAXS formula. This result suggests that the pores in the SiOC(-H) films are spherical. These GISAXS analyses determined the pore size and size distribution. In Fig. 47 we can see the distribution of the number of pores as a function of pore radius for SiOC(-H) films annealed at 400 ℃ deposited with a flow rate ratio of 55 %. From this data, it was observed that the

제주대학교 중앙도서관
JEJU NATIONAL UNIVERSITY LIBRARY

average radius of the most populated pores in the size distribution was about 3.0 nm, the average radius of gyration was about 7.0 nm with a relatively narrow size distribution (σ) of about 0.5. This is smaller than for any other materials, for example M. Morgen *et al.* reported a 6.5 nm average pore size for nano glass films [1], B. D. Lee *et al.* reported 2.5 nm pore size and 8.8 nm average pore size [79]. Spin on deposition (SOD) suppliers such as JSR (Tokyo), Asahi Chemical (Tokyo) and Shipley Co. provide materials with 5.0 nm pore structures, a wide range porosities and dielectric constants of 2.5~1.3. Dow recently announced the preparation of porous SiLK featuring a *k* value of 2.0 and pore size <20.0 nm. According to the International Union of Pure and Applied Chemistry (IUPAS) classification, pores less than 2.0 nm in size are denoted 'micropores' [82]. A. Gill *et al.* reported 1.0~7.0 nm pores in SiOCH film with porosity of 17.0~27.5 %, with dielectric constant from 2.4~2.1 [82]. The pore sizes in as-deposited SiOC(-H) films with high carbon concentrations are not uniform because some $-CH_n$ groups produced large size pores. Relatively large-sized pores with $r \leq 5.0$ nm are becoming significant for after-processing. It is interesting to note that the increase of organic additive concentrations does not change the size of micropores but increases the concentration of large size pores [82]. Therefore pore size and size distribution control are very important for device processes. The detailed GISAXS analyses for the as-deposited and SiOC(-H) films annealed at 400℃

제주대학교 중앙도서관
JEJU NATIONAL UNIVERSITY LIBRARY

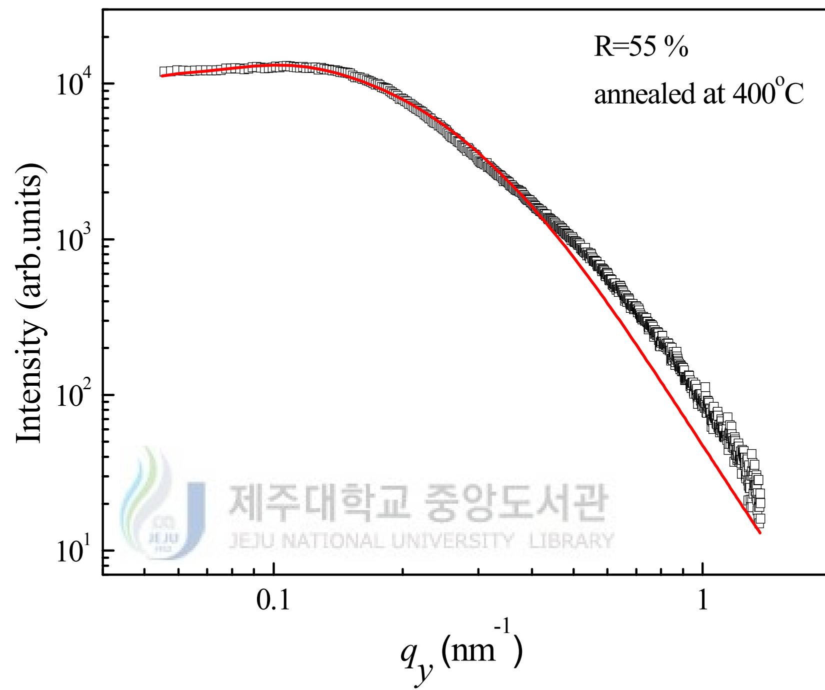

제주대학교 중앙도서관
JEJU NATIONAL UNIVERSITY LIBRARY

Fig. 46. The extracted in-plane GISAXS scattering profiles of the porous SiOC(-H) thin films with annealed at 400 ℃.

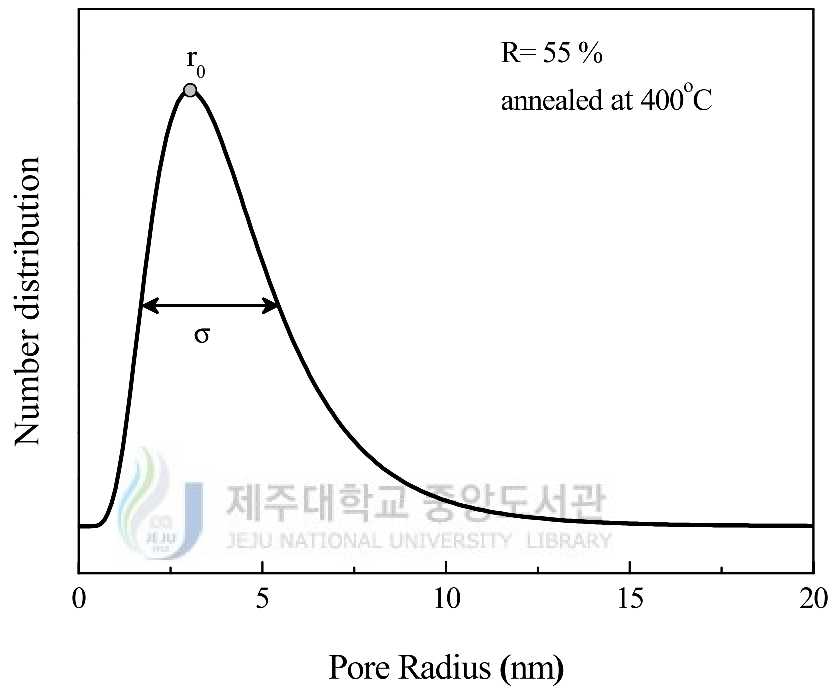

제주대학교 중앙도서관
JEJU NATIONAL UNIVERSITY LIBRARY

Fig. 47. The number distribution of pores as a function of pore radius for annealed SiOC(-H) film at 400 ℃ deposited with a flow rate ratio of 55 %.

with flow rate ratios of 45 and 55 % are listed in Table 6.

At the same time, the GISAXS data for the as-deposited SiOC(-H) films with a flow rate ratio of 85 % as shown in Fig. 48 could not be fitted with the GISAXS formula. This is because the pore sizes in as-deposited SiOC(-H) films with high carbon concentrations are not uniform. This region circled, as shown in Fig. 48. Generally for films which consist of uniform pore size distributions, the left side of the curve should be straight, but in the actual experiment the region was increasing. These results clearly demonstrate that the pore size and size distributions of annealed SiOC(-H) films are better ordered than as-deposited sample films.

Table 6. Pore size and size distribution

R (%)	Annealed temp (℃)	Pore size and size distribution		
		r_o^a (nm)	σ^b	$\overline{r}^c$ (nm)
45	RT	2.09	0.53	3.21
	400	2.33	0.52	3.50
55	RT	2.43	0.53	3.73
	400	2.30	0.53	3.53

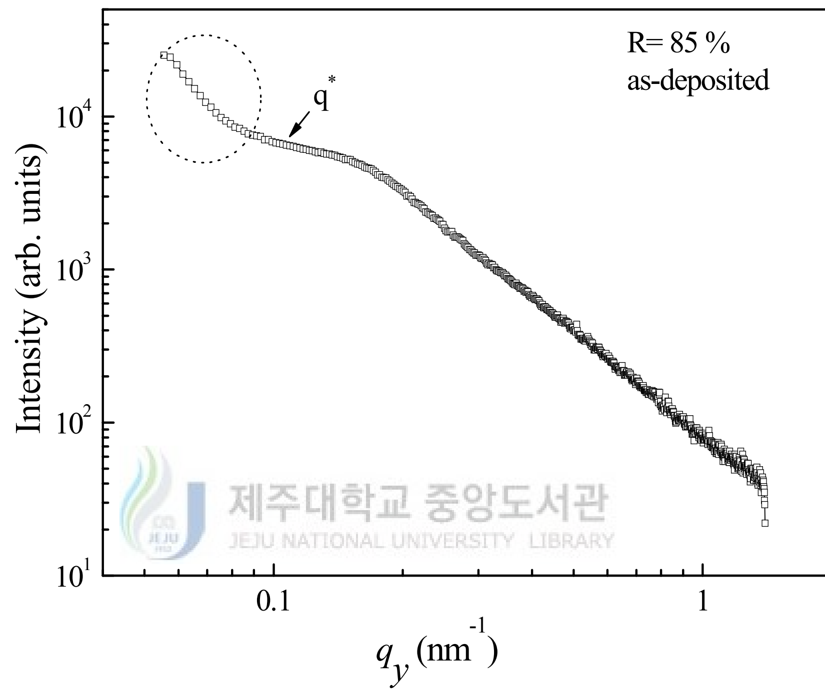

제주대학교 중앙도서관
JEJU NATIONAL UNIVERSITY LIBRARY

Fig. 48. The GISAXS data for the as-deposited SiOC(-H) film with a flow rate ratio of 85 %.

3) XRR Analysis

X-ray reflectivity (XRR) is the direct analogue of X-ray crystallography for interfacial systems. This technique is the feasible routine tool for evaluating the structure of the thin films along depth i.e., layer thickness and interface roughness. We have carried out XRR analysis of SiOC(-H) thin films deposited using BTMSM/(O_2+BTMSM) with flow rate ratios from 45 to 85 %. Figure 49 shows the experimental reflectivity for the SiOC(-H) thin films of as-deposited and samples annealed at 200, 300 and 400 ℃ with a flow rate ratio of 85 %. The experiment parameters are listed in Table 7. From Fig. 49, it is interesting to note that the annealing temperature increase causes the average electron density of SiOC(-H) films to decrease. This result demonstrates that the annealing process enhances the porosity of SiOC(-H) films which in turn reduce the film thickness. Also it is seen from the Fig. 49 that the intensity of reflectivity decreases as the annealing temperature increases, as indicated by the arrow in the curve. Observing the critical angle, it was found that the density of SiOC(-H) films is very low for annealed films when compared to that of as-deposited films. This is mainly due to the porous structure of the SiOC(-H) film, a consequence of the annealing effect. The electron density obtained for the silicon substrate was about 699 nm^{-3} and for the film it was about 660 nm^{-3}. Figure 50 shows the X-ray reflectivity for SiOC(-H) films annealed at 400 ℃ deposited with flow

제주대학교 중앙도서관
JEJU NATIONAL UNIVERSITY LIBRARY

rate ratios from 45 to 85 %. In this figure, the reflectivity is also obtained for silicon wafers and is denoted as Si-WF in the plot. As the flow rate ratio increases the intensity of X-ray reflectivity decreases, which is in accordance with SiOC(-H) film density reduction. The details of the experimental parameters are listed in Table 8. In addition, one can see that as the critical angle decreased, the average electron density of the films also decreased.

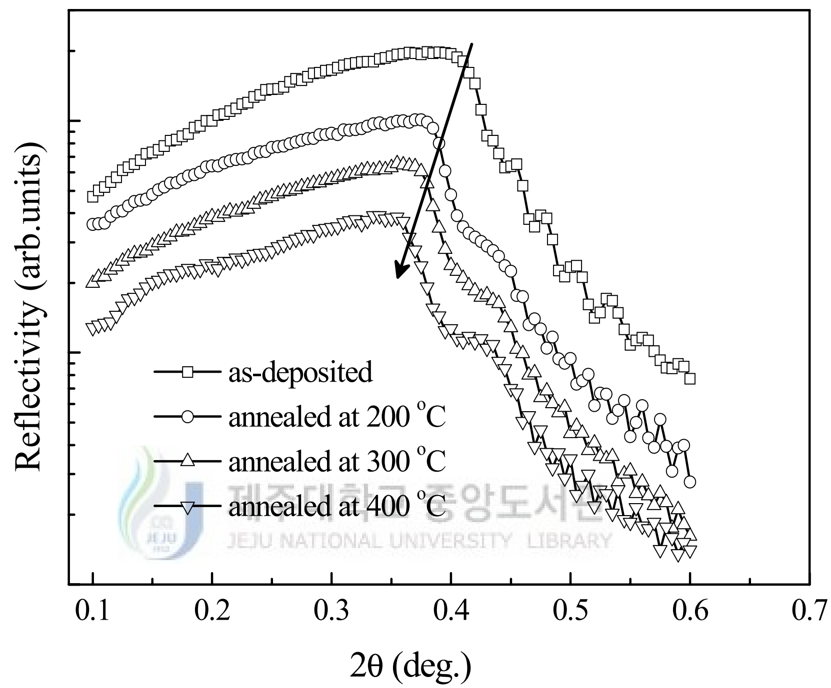

제주대학교 중앙도서관
JEJU NATIONAL UNIVERSITY LIBRARY

Fig. 49. The experimental reflectivity for SiOC(-H) thin films of as-deposited and annealed samples at 200, 300 and 400 ℃ with a flow rate ratio of 85 %.

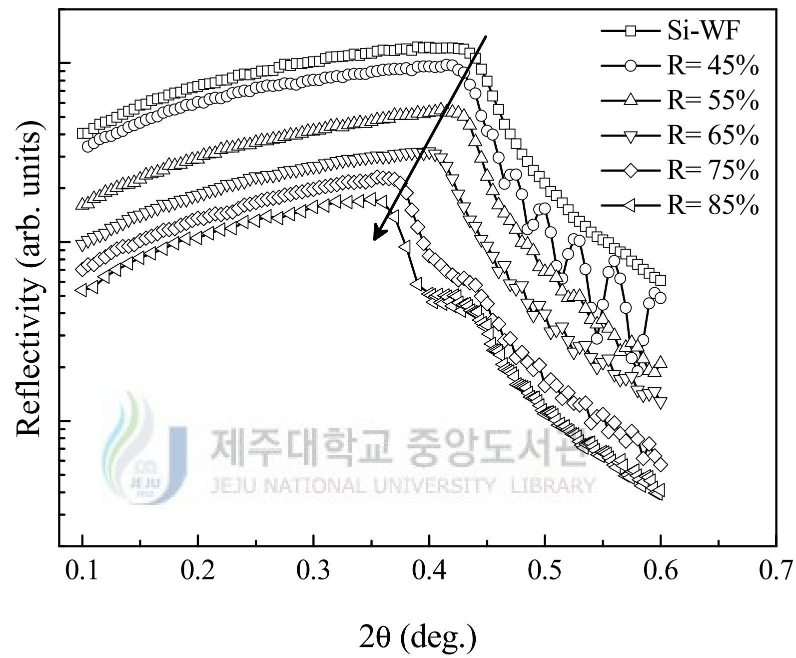

제주대학교 중앙도서관
JEJU NATIONAL UNIVERSITY LIBRARY

Fig. 50. The X-ray reflectivity for SiOC(-H) films annealed at 400 ℃ deposited with various BTMSM/(O_2+BTMSM) flow rate ratio.

Table 7. The critical angle and the average electron density for SiOC(-H) films of as-deposited, annealed samples at 200, 300 and 400 ℃ with a flow rate ratio of 85 %.

R (%)	Annealed temp. (℃)	Critical angle (degree)	Average electron density (nm^{-3})
85	RT	0.207	613
	200	0.194	539
	300	0.190	517
	400	0.185	490

제주대학교 중앙도서관 JEJU NATIONAL UNIVERSITY LIBRARY

Table 8. The critical angle and the average electron density for SiOC(-H) films annealed at 400 ℃ deposited with the flow rate ratios of 45 to 85 %.

R (%)	Annealed temp. (℃)	Critical angle (degree)	Average electron density (nm^{-3})
45	400	0.215	661
55		0.218	680
65		0.209	625
75		0.190	517
85		0.185	490

4) Porosity of SiOC(-H) films

We already determined the effect of porosity on dielectric constants using the Bruggeman effective medium approximation as in Fig. 15. We calculated the film porosities (%) using the Bruggeman effective medium approximation, based on the assumption that thermal oxide has no porosity. Figure. 51 shows the porosity of as-deposited and SiOC(-H) films annealed at 200, 300 and 400 ℃ with various BTMSM/(O_2+BTMSM) flow rate ratios. Porosities of the as-deposited and films annealed at 400 ℃ with a BTMSM/(O_2+BTMSM) flow rate ratio of 45 % increased, and the porosity (%) ranged from 37.0 to 44.8. When the BTMSM/(O_2+BTMSM) flow rate ratio was 85 %, the porosity increased from 46.0 to 49.7. Table 9 shows the porosity and dielectric constant of as-deposited and SiOC(-H) films annealed at 200, 300 and 400 ℃ with BTMSM/(O_2 +BTMSM) flow rate ratios. From these results, we can infer that the porosity of SiOC(-H) composite films depends on the relative carbon content and the dielectric constant.

제주대학교 중앙도서관
JEJU NATIONAL UNIVERSITY LIBRARY

We can see the relationship between porosity and various factors in Fig. 51 and the ring-link concentration of Si-O-C asymmetric stretching mode from Fig. 25. The porosity increase is due to the increased relative content of Si-O-C ring-link mode, in which the carbon atoms are incorporated into the Si-O-Si bonds. The porosity increases linearly from 44.8 to 49.7 % and the Si-O-C ring link concentration also increases linearly from 16.1 to 29.2 % when the flow rate ratio increases from 45 to 85 % in as-deposited films. When annealed at 400 ℃, the porosity increases from 37.1 to 46.0 % and the Si-O-C ring-link concentration also increases from 19.1 to 31.8 %. We can see the direct proportionality between the porosity and the Si-O-C

ring-link concentration. Hence, many voids are created in the film, which results in enhanced porosity. The reduction of nano-pore size may be due more to carbon incorporation in the film. The pore generation mechanism during the deposition process seems to resemble that of open-linked substructures changing to ring-linked substructures, which may be related to the reduction in OH groups and to the incorporation of carbon atoms in the Si-O-Si network.

제주대학교 중앙도서관
JEJU NATIONAL UNIVERSITY LIBRARY

Table 9. The porosity and dielectric constant of SiOC(-H) composite films, as-deposited and annealed at 200, 300 and 400 ℃ with various BTMSM/(O_2+BTMSM) flow rate ratios.

R (%)	RT		200 ℃		300 ℃		400 ℃	
	Porosity	*k*	Porosity	*k*	Porosity	*k*	Porosity	*k*
45	37.10	2.60	40.00	2.50	42.37	2.42	44.77	2.34
55	40.00	2.50	42.07	2.43	42.96	2.40	45.99	2.30
65	42.96	2.40	44.47	2.35	45.07	2.33	46.60	2.28
75	45.07	2.33	45.68	2.31	46.30	2.29	47.53	2.25
85	45.99	2.30	46.91	2.27	48.46	2.22	49.72	2.18

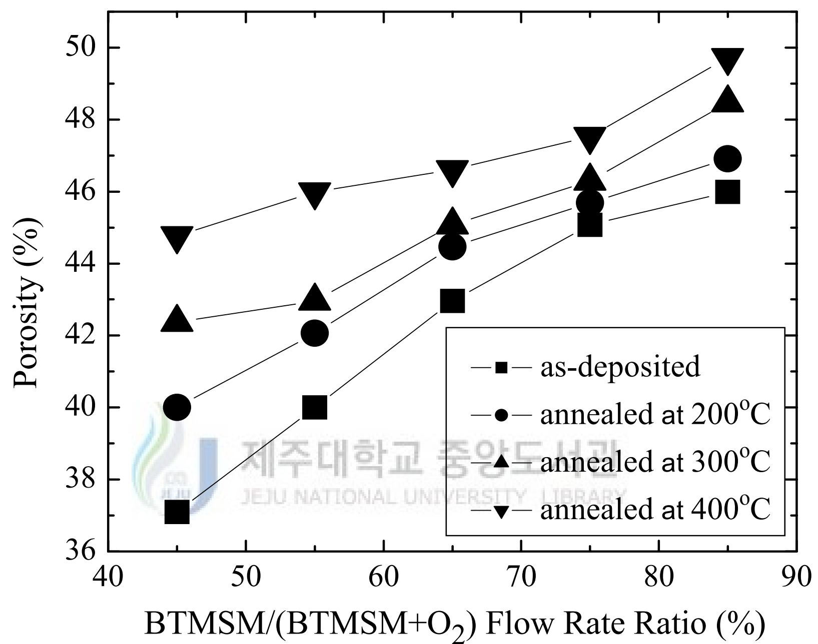

제주대학교 중앙도서관
JEJU NATIONAL UNIVERSITY LIBRARY

Fig. 51. The porosity of SiOC(-H) composite films, as-deposited and annealed at 200, 300 and 400 ℃ with various BTMSM/(O_2+BTMSM) flow rate ratios.

5) Film density and composition

The SiOC(-H) film composition was determined by TOF-ERD analysis. Determining the content and depth profiles of the light elements are the major aims of this analysis. This analysis is similar to Rutherford back-scattering spectroscopy, in which the time of flight with the energy of recoil particle are measured, from which a two-dimensional plot between energy and time are obtained which is nothing more than the masses of the constituent elements in the film. Figure 52 shows the ERD-TOF scatter plot of SiOC(-H) films annealed at 400 ℃ with BTMEM/(O_2+BTMSM) flow rate ratios of (a) 45 %, (b) 55 %, (c) 65 %, (d) 75 % and (e) 85 %. In this experiment, $^{35}Cl^{5+}$ ions accelerated to 9.628 MeV were employed as the incident beam. The time of flight elastic recoil and energy are detected at the same time and converted into mass and energy data. The same mass of the atoms appear on one line of the scatter plot. The short line at the top of the scatter plot corresponds to the signal from hydrogen as shown in Fig. 52. Hydrogen appears to exist with the same intensity for all cases of the flow rate ratio. Fig. 52 shows the scattering energy versus time of flight for various constituent atoms such as hydrogen, oxygen, carbon, silicon and chlorine. Here chlorine is taken as a reference material, which is used as the incident beam. Our interest focuses on the constituent materials of SiOC(-H) film and in determining the depth profile. In Fig. 52 each atom's time of flight is clearly separated and mentioned. Since hydrogen has a lower atomic weight, it has the largest time of flight. The next three lines of the scatter

제주대학교 중앙도서관
JEJU NATIONAL UNIVERSITY LIBRARY

plot are those of carbon, oxygen and silicon and the last line of the scatter plot is that of chlorine in response to the incident ion beam. The lines corresponding to each atom illustrate their intensity with respect to flow rate ratios of the SiOC(-H) film. As the flow rate ratio increases from 45 % to 85 % the carbon content in the film increases, which is directly observed in Fig. 53 (a) to (e). At the same time, the intensity of oxygen is observed to be decreasing with the increase in the flow rate ratio. Therefore by doing the TOF-ERD analysis, the existence of individual atomic concentrations in the SiOC(-H) film is clearly demonstrated. This is direct evidence of measuring the atomic concentration in SiOC(-H) films. This experimental result also is in good agreement with the FTIR analysis.

Moreover, the RBS spectra of SiOC(-H) films annealed at 400 ℃ with BTMSM/(O_2+BTMSM) flow rate ratios of (a) carbon, (b) oxygen (c) hydrogen and (d) silicon are shown in Fig. 52. From Fig. 52 it is observed that the total counts of each atom corresponding to the energy is increased with flow rate ratio for hydrogen and carbon. And for oxygen, the counts amount is decreased as the flow rate ratio is increased from 45 % to 85 %. In the case of silicon atoms as the scatter energy increases the count rate decreases when the energy attains the value of 225 MeV the counts remains constant for further rise in the scatter energy that shows the interface of film and substrate.

제주대학교 중앙도서관
JEJU NATIONAL UNIVERSITY LIBRARY

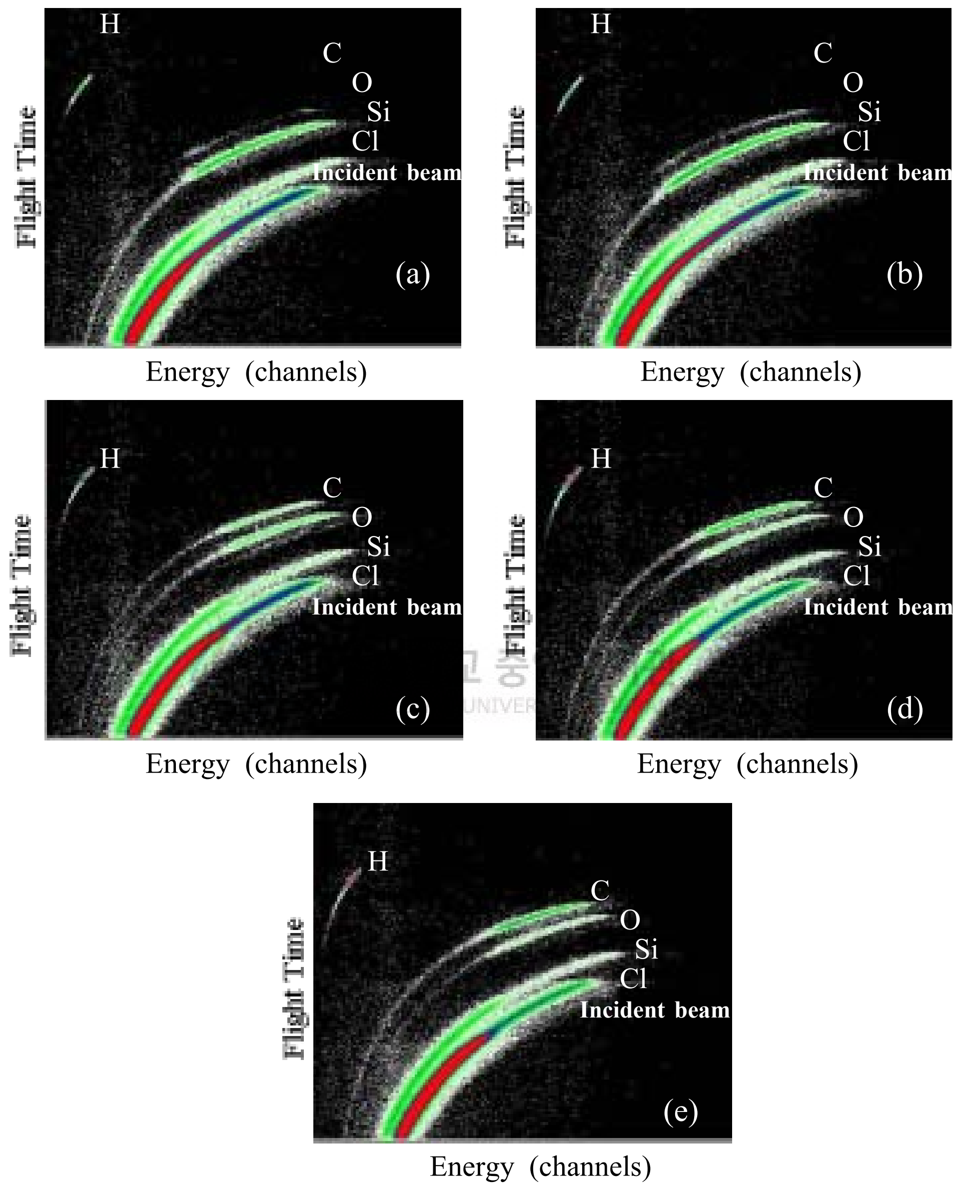

Fig. 52. Flight time versus energy scatter plot of annealed SiOC(-H) film at 400 ℃ with various BTMSM/(O_2+BTMSM) flow rate ratios of (a) 45 %, (b) 55 %, (c) 65 %, (d) 75 % and (e) 85 %.

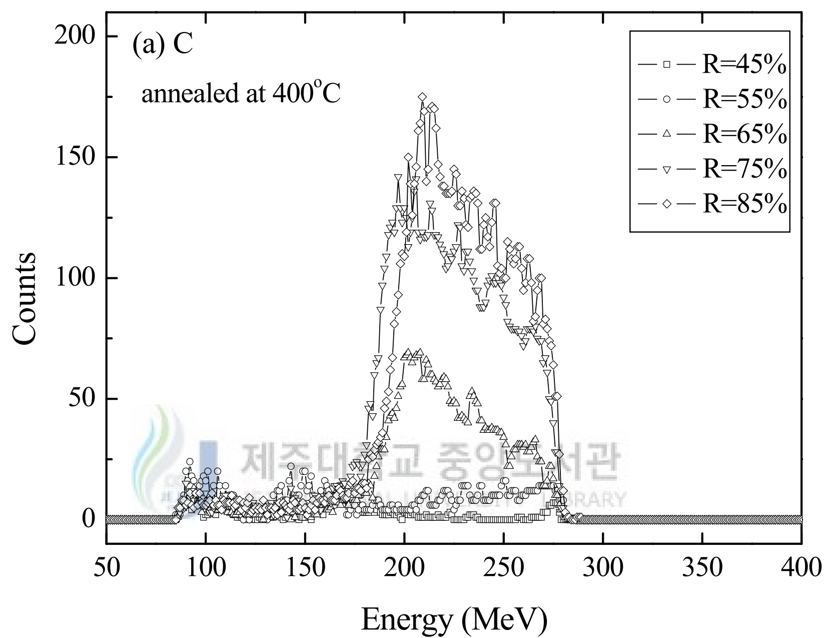

Fig. 53. RBS spectra of SiOC(-H) annealed films at 400 ℃ with BTMSM/(O_2+BTMSM) flow rate ratios. (a) carbon, (b) oxygen, (c) hydrogen and (d) silicon

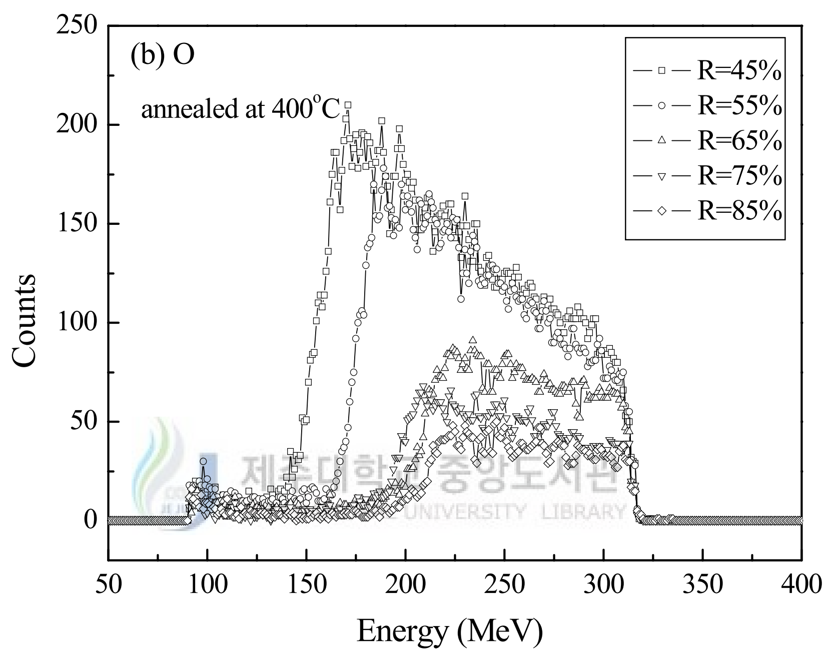

제주대학교 중앙도서관
UNIVERSITY LIBRARY

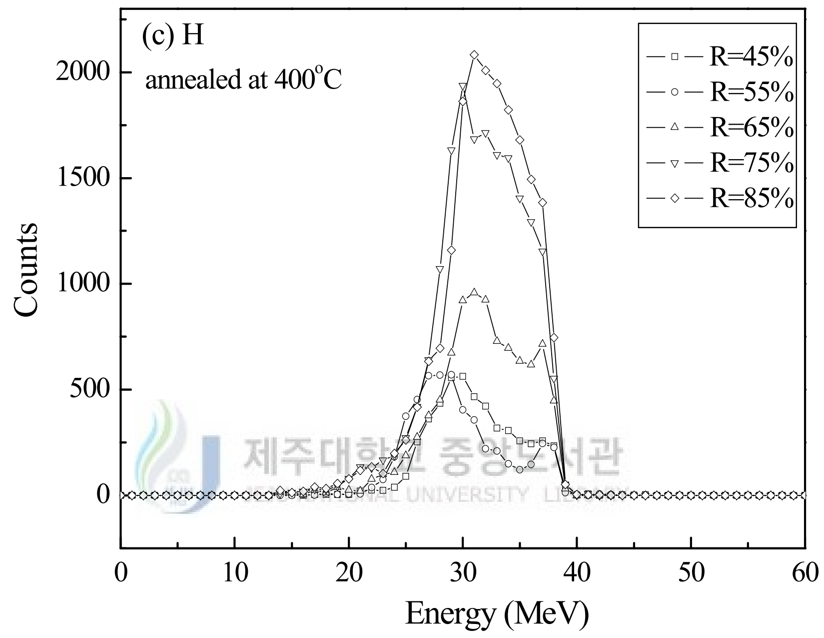

제주대학교 중앙도서관
JEJU NATIONAL UNIVERSITY LIBRARY

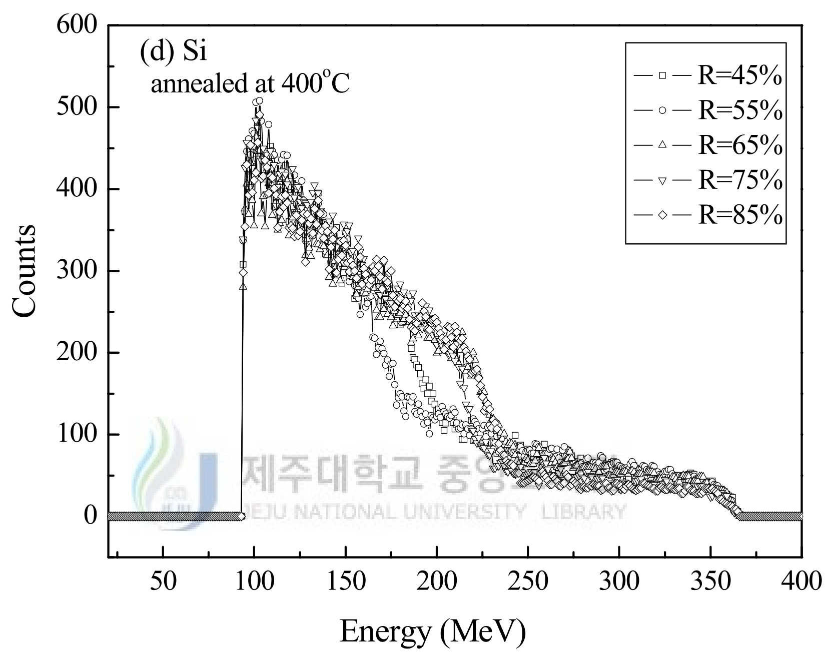

제주대학교 중앙도서관
JEJU NATIONAL UNIVERSITY LIBRARY

Figure 54 shows the time of flight versus the energy scatter plot of SiOC(-H) films with a BTMSM/(O_2+BTMSM) flow rate ratio of 85 % for as-deposited and SiOC(-H) films annealed at 200, 300 and 400 ℃. The corresponding depth profile of RBS spectra for films with 85 % flow rate annealed at 200, 300 and 400 ℃ for each of the atoms carbon, oxygen, hydrogen and silicon are shown in Fig. 55.

제주대학교 중앙도서관
JEJU NATIONAL UNIVERSITY LIBRARY

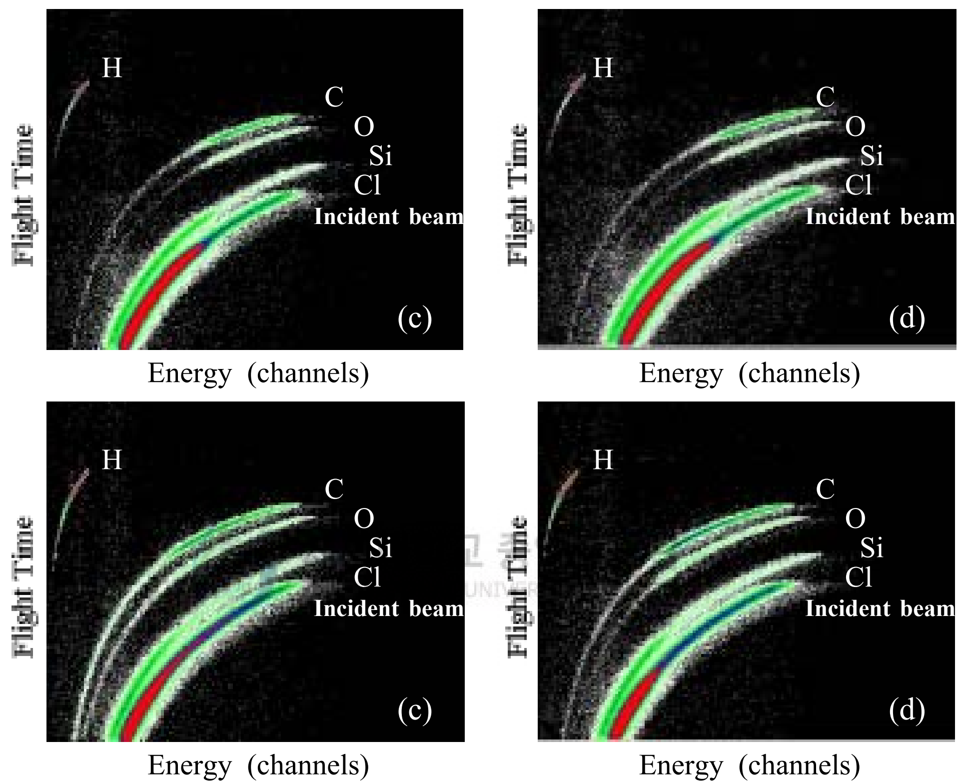

Fig. 54. Flight time versus energy scatter plot of SiOC(-H) film with BTMSM/(O_2+BTMSM) flow rate ratios of 85 % at (a) as-deposited and annealed at (b) 200 ℃, (c) 300 ℃ and (d) 400 ℃.

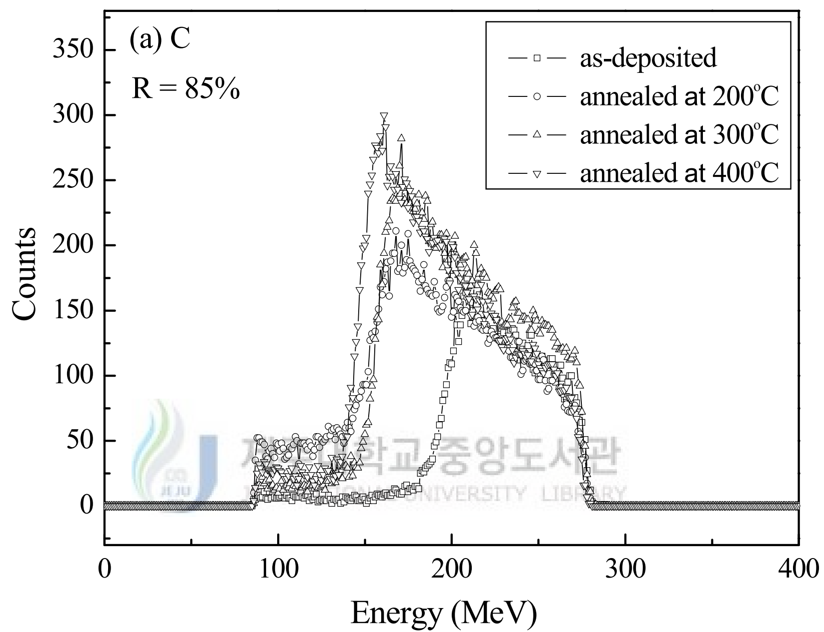

Fig. 55. RBS spectra of SiOC(-H) annealed film at 400℃ with BTMSM/(O_2+BTMSM) flow rate ratio of 85 % of as-deposited and annealed films at 200, 300 and 400 ℃, (a) carbon, (b) oxygen, (c) hydrogen and (d) silicon.

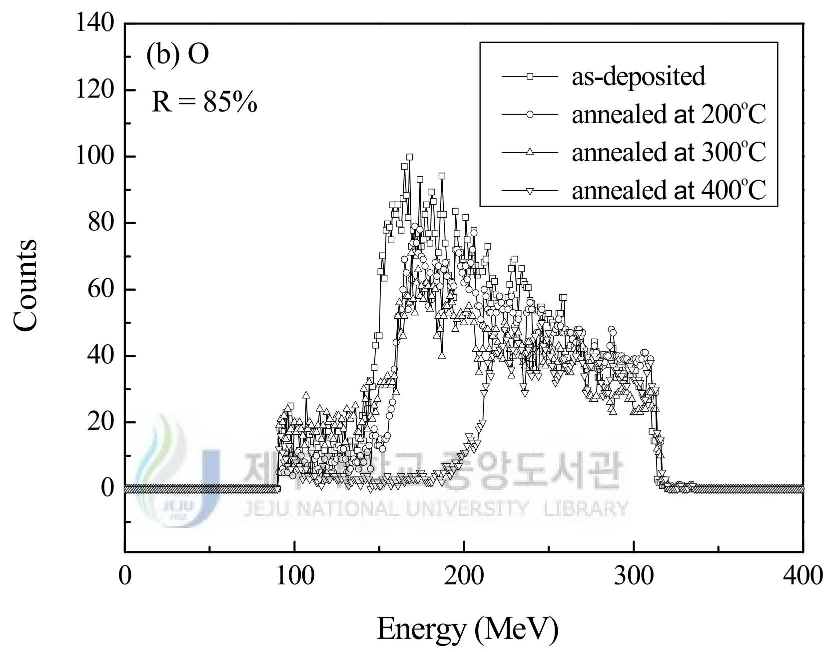

제주대학교 중앙도서관
JEJU NATIONAL UNIVERSITY LIBRARY

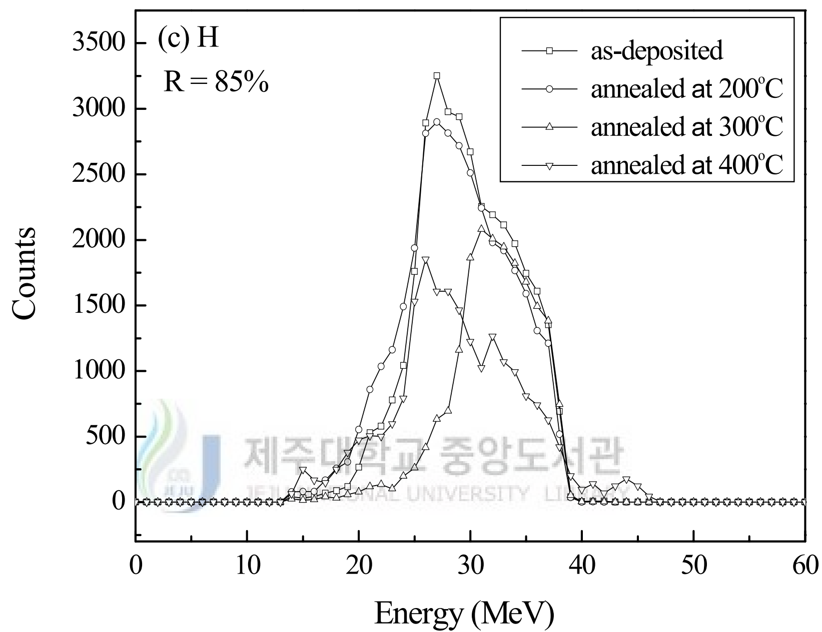

제주대학교 중앙도서관
JEJU NATIONAL UNIVERSITY LIBRARY

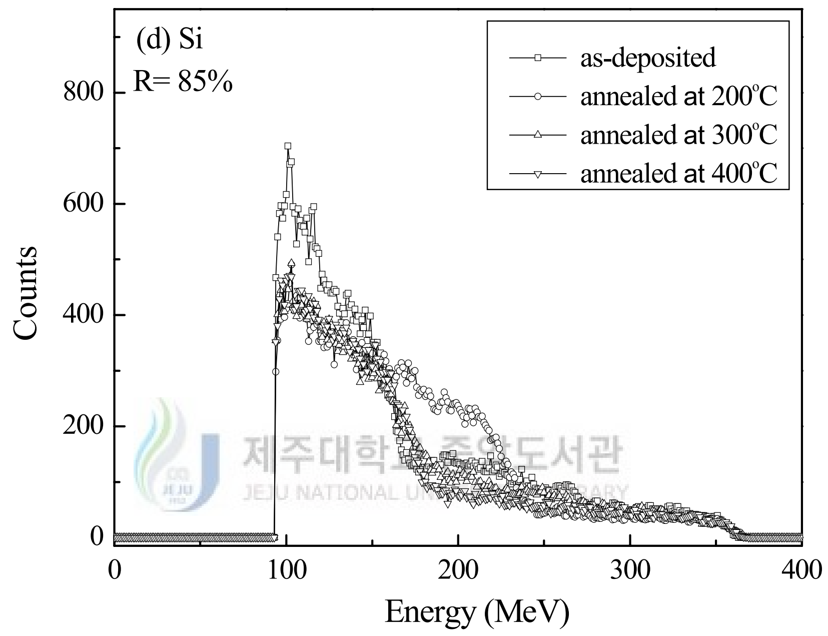

제주대학교 중앙도서관
JEJU NATIONAL UNIVERSITY LIBRARY

The atomic concentration and density of SiOC(-H) films was determined by ERD-TOF analysis. Figure 56 shows the atomic concentration of as-deposited and films annealed at 200, 300 and 400 ℃ measured by ERD-TOF in the bulk range (about 1400×10^{15} atoms/cm^2) with a BTMSM/(O_2+ BTMSM) flow rate ratio of 85 %. The hydrogen concentration of the sample annealed at 400 ℃decreased 1.5 % more than that of the as-deposited sample. The hydrogen, oxygen and silicon concentrations of samples annealed at 400 ℃ decreased slightly more than that of as-deposited samples, 1.5, 1.5 and 0.9 %, respectively. The carbon content increased by 4 % after annealing the SiOC(-H) film. From these results, we can infer that after the annealing treatment, the oxygen concentration decreases because some HO_2 is removed from the bulk of the film [16, 17].

Figure 57 shows the atomic concentrations of films annealed at 400 ℃ measured by ERD-TOF in the bulk range (about 1400×10^{15}atoms/cm^2) with BTMSM/(O_2+ BTMSM) flow rate ratios of 45, 55, 65, 75 and 85 %. The hydrogen concentration at a flow rate ratio of 85 % increased 20 % more than that of the sample with a flow rate ratio of 45 %. The oxygen and silicon concentrations of the sample having a flow rate ratio of 85 % decreased more than that of samples having a flow rate ratio of 45 %, with the flow rate ratio of 85 % samples registering a 48.4 % and 14.4 %. decline, respectively. The carbon concentration of SiOC(-H) films with flow rate ratios of 45 and 55 % increased slightly by 4.1 %, from 2.9 to 7.0 %. The carbon concentration of SiOC(-H) films with flow rate ratios of 65, 75 and 85 % suddenly increased to 21.4, 38.2 and 45.3 %, respectively.

제주대학교 중앙도서관
JEJU NATIONAL UNIVERSITY LIBRARY

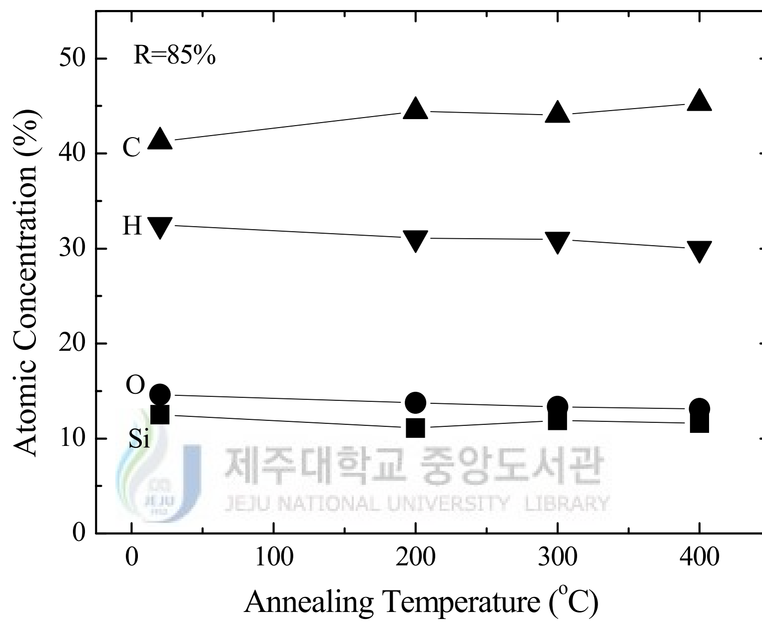

제주대학교 중앙도서관
JEJU NATIONAL UNIVERSITY LIBRARY

Fig. 56. The atomic concentration of as-deposited and annealed films at 200, 300 and 400 ℃ measured by ERD-TOF with BTMSM/(O_2+BTMSM) flow rate ratio of 85 %.

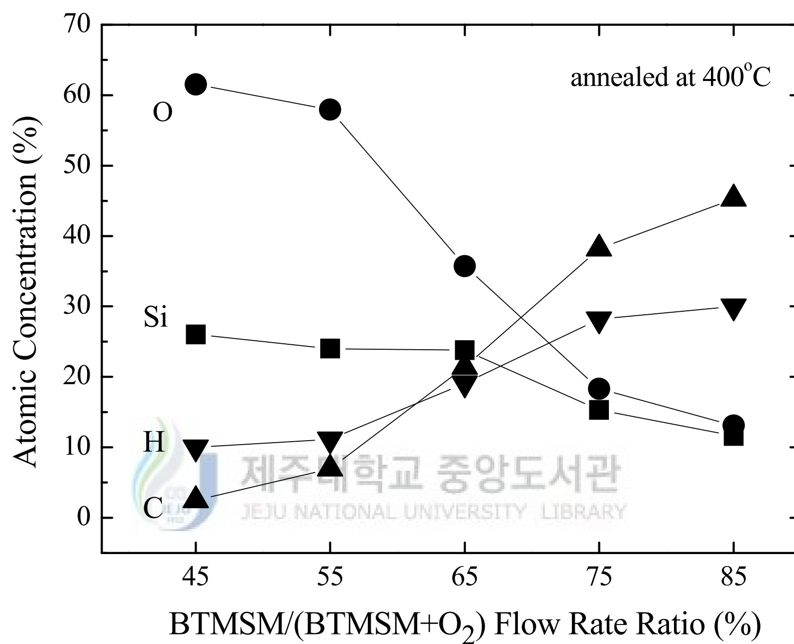

제주대학교 중앙도서관
JEJU NATIONAL UNIVERSITY LIBRARY

Fig. 57. The atomic concentration of annealed films at 400 ℃ measured by ERD-TOF with BTMSM/(O_2+BTMSM) flow rate ratios of 45, 55, 65, 70 and 85 %.

The density of SiOC(-H) film is calculated by dividing the value of the atomic density per unit area by the film thickness. Fig. 58 and Table 10 show the density of as-deposited and SiOC(-H) films annealed at 200, 300 and 400℃ with various BTMSM/(O_2+BTMSM) flow rate ratios. Overall, the density of SiOC(-H) films decreased as the flow rate ratio increased. The density of as-deposited SiOC(-H) films decreased from 2.42 to 1.21 g/cm^3 as flow rate ratios increased from 45 % to 85 %. The density of 400 ℃ annealed SiOC(-H) films was calculated as 2.10, 1.75, 1.32 1.04 and 0.98 g/cm^3, respectively, for BTMSM/(BTMSM+O_2) flow rate ratios of 45, 55, 65, 75 and 85 %. It means that the decrease in the film density is due to void formation in the film.

The density of SiOC(-H) films annealed at 400 ℃ were calculated as 1.21, 1.09, 1.08 and 0.98 g/cm^3, respectively, for a BTMSM/(BTMSM+O_2) flow rate ratio of 85 %. This means that the decrease of the film density is due to void formation in the film. The decrease in density after annealing indicates that a rearrangement of bonding structure in the film results in the formation or enhancement of pre-existing atomic-scale nano-pores in the film. From these results we can surmise that after annealing treatment, the oxygen concentration decreases because some H-O groups or H_2O is removed from the bulk of the film [18, 74].

제주대학교 중앙도서관
JEJU NATIONAL UNIVERSITY LIBRARY

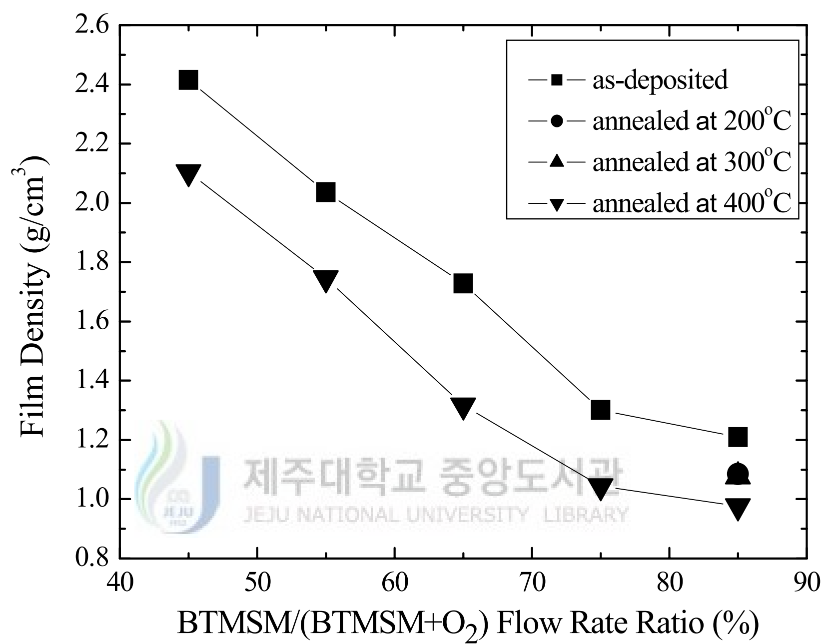

제주대학교 중앙도서관
JEJU NATIONAL UNIVERSITY LIBRARY

Fig. 58. The density of as-deposited and annealed SiOC(-H) films at 200, 300 and 400 ℃ with various BTMSM/(O_2+BTMSM) flow rate ratios.

Table 10. The density (g/cm^3) of as-deposited, annealed SiOC(-H) films at 200, 300 and 400 ℃ with BTMSM/(O_2+BTMSM) flow rate ratios.

Flow rate ratios R (%)	Film density (g/cm^3) of annealing condition			
	As-deposited	200 ℃	300 ℃	400 ℃
45	2.42	-	-	2.10
55	2.04	-	-	1.75
65	1.73	-	-	1.32
75	1.30	-	-	1.04
85	1.21	1.09	1.08	0.98

제주대학교 중앙도서관
JEJU NATIONAL UNIVERSITY LIBRARY

6) TEM images

Fig. 59 shows the cross-sectional transmission electron microscopy (TEM) images of as-deposited and annealed SiOC(-H) samples with a flow rate ratio of 85 %. In the as-deposited sample, nano-sized pores were formed locally within the film and were not uniform as shown Fig. 59(a). A thin layer is clearly seen at the Si-O-C/Si interface of the sample annealed at 400 ℃ and is a native oxide (see Fig. 59(b)). The annealed sample had more nano-sized pores distributed regularly from the interface of the Si-O-C/Si(100) structure to the surface of the SiOC(-H) film, and the pore diameter was 1~2 nm. This result agrees well with the result of SANS measurement. The nano-sized pores in the SiOC(-H) film deposited using BTMSM/O_2 precursors are formed partly by the deposition itself and by the annealing process. In our as-deposited sample, we can see the nano-sized pores within the film, and they can be interpreted as arising from the formation of voids due to deposition temperature generated by the heating of the substrate by plasma during the deposition process. We also know that this TEM image agrees with the FTIR results. Therefore, the dielectric constant of post-annealed films is expected to decrease to a value lower than that of as-deposited films. The measured dielectric constant was decreased from 2.30 to 2.18 by the annealing process.

제주대학교 중앙도서관
JEJU NATIONAL UNIVERSITY LIBRARY

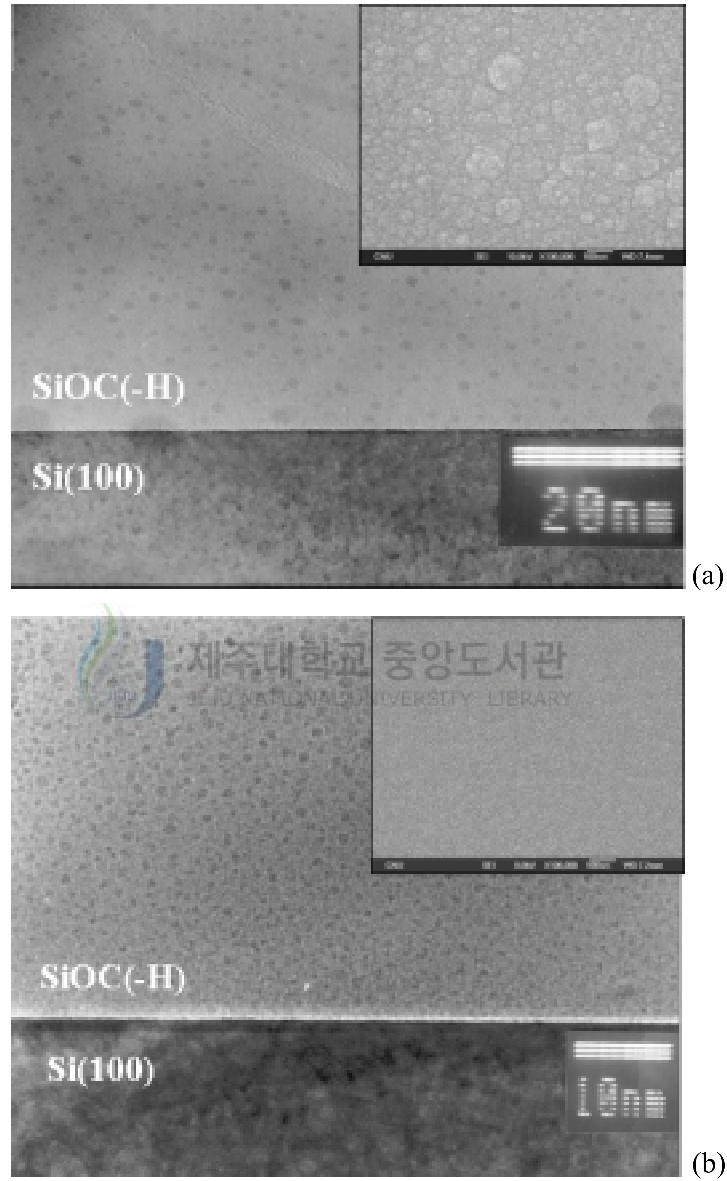

제주대학교 중앙도서관
JEJU NATIONAL UNIVERSITY LIBRARY

Fig. 59. The Cross-sectional TEM images of (a)as-deposited and (b)annealed SiOC(-H) films at 400 ℃.

3. Mechanical and electrical properties

1) Mechanical hardness and elastic modulus

Mechanical properties such as hardness and elastic modulus of the film are investigated by the nano-indentation method. Figure 60 shows the variation of the hardness value as a function of the indentation depth for as-deposited and SiOC(-H) films annealed at 200, 300 and 400℃ with various flow rate ratios. The hardness invariability observed for indentation depths of above 20.0 nm indicates that there is no influence of the substrate on the measured hardness value. The maximum indentation depth used in thin-film hardness measurements should not exceed 10 % of the film thickness. The obtained hardness values of as-deposited and annealed films decreases when the BTMSM/(O_2+BTMSM) flow rate ratio increases. The hardness values of as-deposited films range from 2.6 to 1.6 GPa, while that of annealed films varies by temperature: films annealed at 200 ℃ had hardness values ranging from 2.3 to 1.3 GPa, while that of films annealed at 300℃ had hardness values ranging from 2.1 to 0.8 GPa, Finally, films annealed at 400 ℃ had hardness values ranging from 2.0 to 0.7 GPa. These values are lower than the hardness values of TEOS-SiO_2 film (8.0~10.0 GPa), but much higher than SiLK film (0.1~0.2 GPa) in Table 8 [68, 20]. The increase of BTMSM precursors tends to decrease hardness because porosity increases, and the density of film decreases with increasing carbon content [72]. Therefore, the void formed in the annealed SiOC(-H) films is responsible for low dielectric constants and also decreases the hardness of the films.

Figure 61 shows the elastic modulus of SiOC(-H) as-deposited and annealed

제주대학교 중앙도서관 JEJU NATIONAL UNIVERSITY LIBRARY

films as a function of the indention depth for various flow rate ratios. The obtained elastic modulus values of as-deposited and annealed films decreased as a function of the BTMSM/(O_2+BTMSM) flow rate ratios. Elastic modulus values of as-deposited films ranged from 26 to 14 GPa, while these values depended on the temperature for annealed films. For films annealed at 200 ℃ the value ranged from 23 to 11 GPa, for films annealed at 300 ℃, values ranged from 21 to 7 GPa, and for films annealed at 400 ℃, elastic modulus values ranged from 20 to 7 GPa. These values are lower than those for TEOS SiO_2 film (70~90 GPa) but much higher than those of SiLK film (3~4 GPa) in Table 11 [63]. Typically, MSQ-based materials of 1 ㎛, engineered with subtractive techniques to achieve around 45~50 % porosity, have an elastic modulus of around 2 GPa or below and hardness values of around 0.13~0.57 GPa [45]. Coral and carbon-doped oxide or oganosilcate glass low-k materials of 1 ㎛ made by the Novellus Sequel PECVD method have a dielectric constant of 2.9~3.0 and modulus of 9 and 15 GPa, respectively [83]. The increase of BTMSM precursors tends to decrease the elastic modulus. Therefore, the void formed in the annealed SiOC(-H) films affects the decrease in hardness and elastic modulus. From the results of Fig. 60 and Fig. 61, we can infer that there are two reasons for SiOC(-H) films having the lowest elastic modulus and hardness [18]. One reason is that the density is the lowest. The porous ceramic represents the limiting case of two-phase materials, in which one phase has zero stiffness. Also, the elastic modulus decreases with increasing porosity. The second reason is based on carbon incorporation in the film. Since the incorporation of carbon in SiOC(-H) film softens the oxide to make it more like polymer, SiOC(-H) film is more plastic than other

제주대학교 중앙도서관
JEJU NATIONAL UNIVERSITY LIBRARY

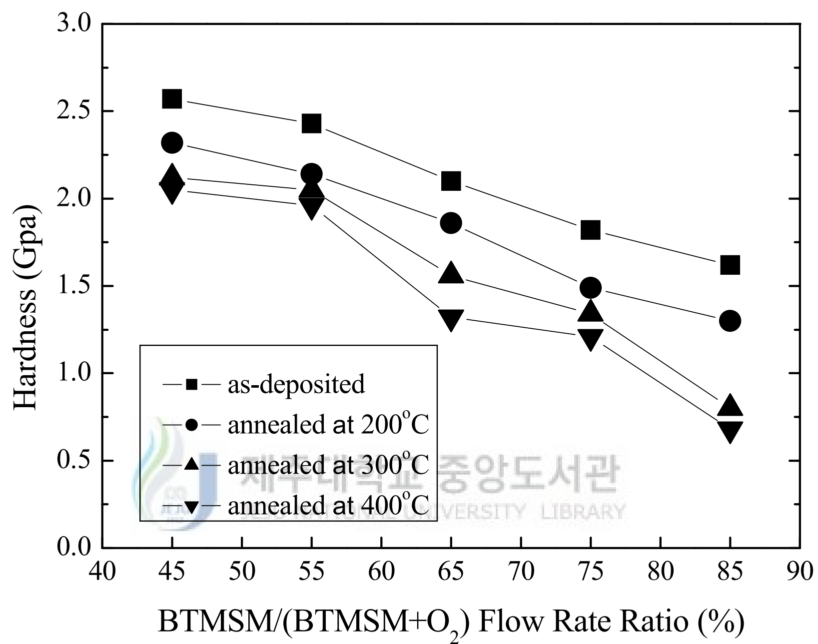

Fig. 60. Variation of the hardness (H) values of as-deposited and the annealed SiOC(-H) films as a function of BTMSM/(BTMSM+O_2) flow rate ratios.

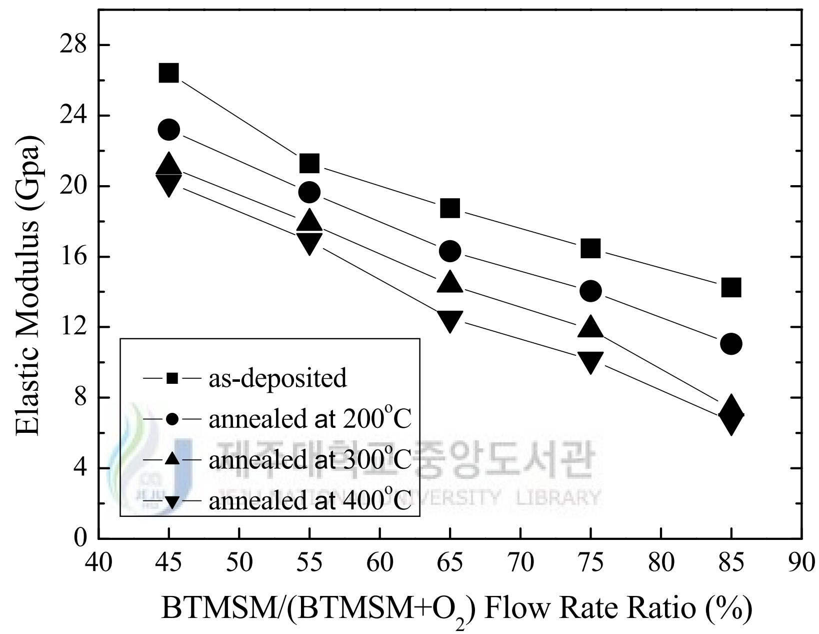

제주대학교 중앙도서관

Fig. 61. The elastic modulus (E) of as-deposited and annealed SiOC(-H) films as a function of BTMSM/(BTMSM+O_2) flow rate ratios.

Table 11. Mechanical properties of Low-k films.

	PECVD TEOS SiO_2	Zirkon	SiLK	Porous SiLK	XLK	SiCOH	SiOC(-H) Flow rate ratio & annealed					
							45 %		65 %		85 %	
							RT	400℃	RT	400℃	RT	400℃
Hardness(GPa)	**8.00**	**0.45**	**0.20**	**0.16**	**0.20**	**0.25**	**2.57**	**2.05**	**2.10**	**1.32**	**1.62**	**0.68**
Modulus(GPa)	**71.7**	**3.1**	**3.2**	**2.5**	**2.0**	**3.2**	**26.4**	**20.2**	**18.7**	**12.5**	**14.3**	**6.7**

films. Because SiOC(-H) film is more porous and softer than other films, the elastic modulus and the hardness of SiOC(-H) films is less than that of other films.

SiOC(-H) containing alkyl groups has attracted more attention for its higher thermal and mechanical stability compared to many organic materials. The spatial hindrance of alkyl groups may produce abundant nano-size voids in the film and decrease the dielectric constant. From the above results, it is reasonable to expect that the elastic modulus and the hardness decrease with the increase in carbon content of SiOC(-H) film. Numerous researchers have proposed equations to relate the elastic modulus to the amount of porosity and most of these have been summarized by Wachman. The equations are in the form

$$E=E_0(1-f_1+f_2p_2) \qquad (4\text{-}4)$$

where E_0 is the modulus for fully dense material, f_1 and f_2 are constants, and p_2 is the fraction porosity [68].

제주대학교 중앙도서관

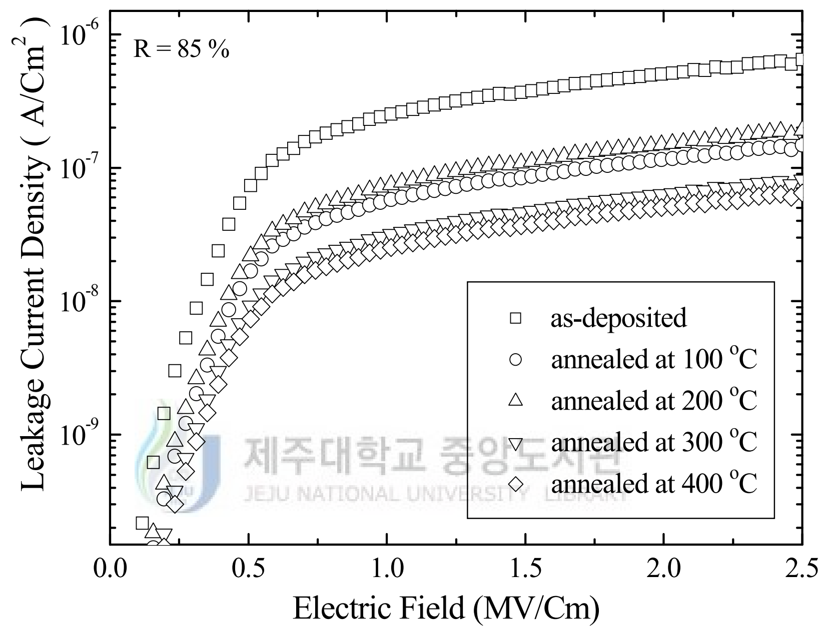

제주대학교 중앙도서관
JEJU NATIONAL UNIVERSITY LIBRARY

Fig. 62. The leakage current density as a function of the electrical field strength for SiOC(-H) films of as-deposited and annealed 100, 200, 300 and 400 ℃ with BTMSM/(O_2+BTMSM) flow rate ratio of 85 %.

2) Current-voltage (I-V) characteristics

Electrical leakage currents for the SiOC(-H) films are measured using a metal-insulator-semiconductor (MIS) structure. Figure 62 shows the leakage current density of as-deposited and SiOC(-H) films annealed at 100, 200, 300 and 400 ℃ with a BTMSM/(O_2+BTMSM) flow rate ratio of 85 % as a function of the electrical field strength. The leakage current density increases with increases in annealing treatment. It is observed from the I-V characteristics that the leakage current density at 1 MV/cm increased from 2×10^{-7} to 2.2×10^{-8} A/cm^2 for both as-deposited and samples annealed at 400 ℃.

$\ln J$ versus the square root of electric field E is characterized as a function of measurement temperature for BTMSM/(O_2+BTMSM) flow rate ratios of 45 and 85%, respectively. Figure 63 and 64 show the characteristics for as-deposited and films annealed at 400 ℃ with a flow rate ratio of 45 %. It is found that the $\ln J$ value linearly increases with the square root of the electric field. Further, it is noted that the temperature is influenced by the film resulting in an increase in the electric field upon an increase in temperature. In contrast, for the sample annealed at 400 ℃ the value $\ln J$ increases steeply for the electric field value of 0.1 $(MV/cm)^{1/2}$. In the case of films with a BTMSM/(O_2+BTMSM) flow rate ratio of 85%, $\ln J$ linearly increases with the electric field for both as-deposited and samples annealed at 400 ℃ as shown in Fig. 65 and 66.

제주대학교 중앙도서관
JEJU NATIONAL UNIVERSITY LIBRARY

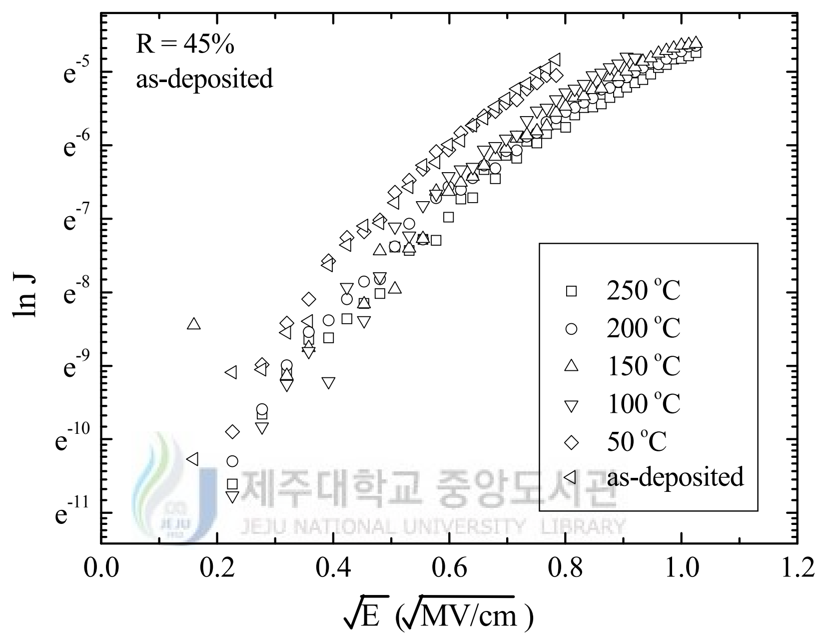

제주대학교 중앙도서관
JEJU NATIONAL UNIVERSITY LIBRARY

Fig. 63. " $\ln J$" versus electric field $\sqrt{E}$: characteristics as a function of measurement temperature with a BTMSM/(O_2+BTMSM) flow rate ratio of 45 %.

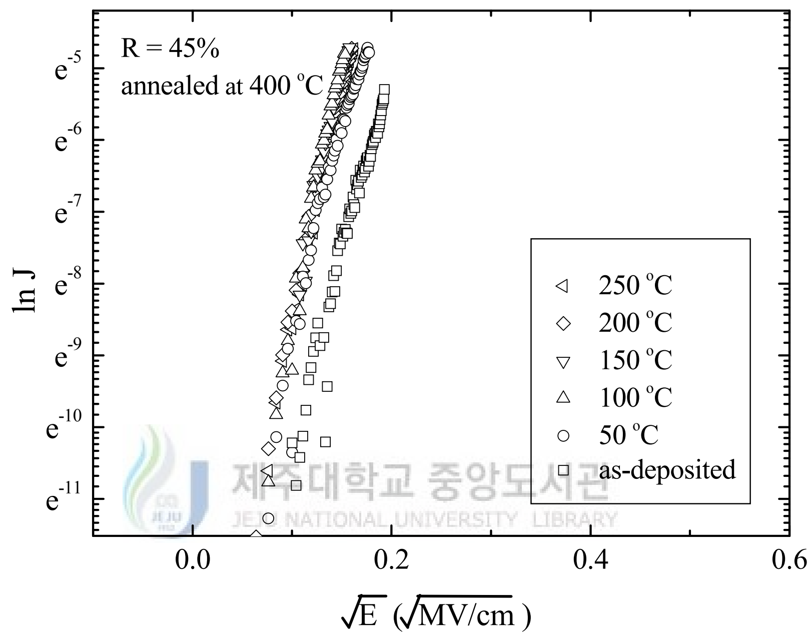

제주대학교 중앙도서관
JEJU NATIONAL UNIVERSITY LIBRARY

Fig. 64. "$\ln J$" versus electric field $\sqrt{E}$: characteristics as a function of measurement temperature for annealed films at 400 ℃ with BTMSM/(O_2+BTMSM) flow rate ratio of 45 %.

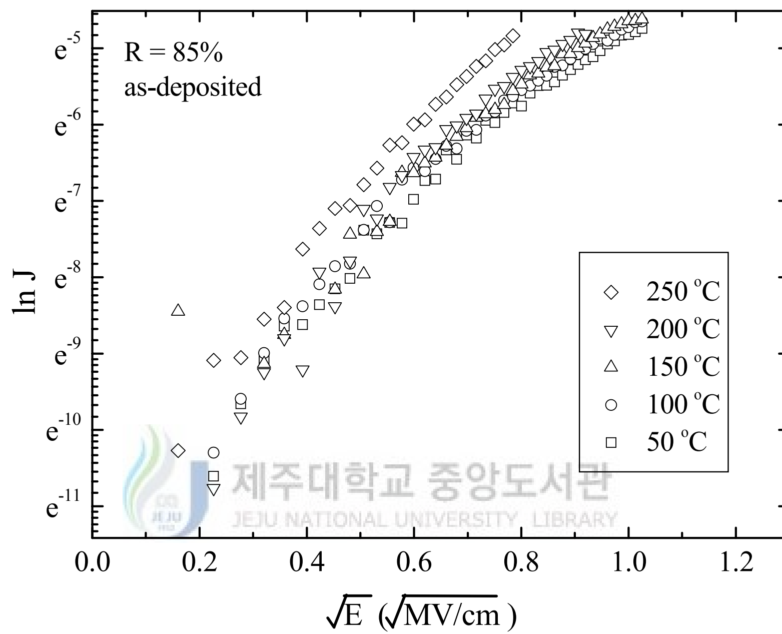

제주대학교 중앙도서관
JEJU NATIONAL UNIVERSITY LIBRARY

Fig. 65. " $\ln J$" versus electric field $\sqrt{E}$: characteristics as a function of measurement temperature with a BTMSM/(O_2+BTMSM) flow rate ratio of 85 %.

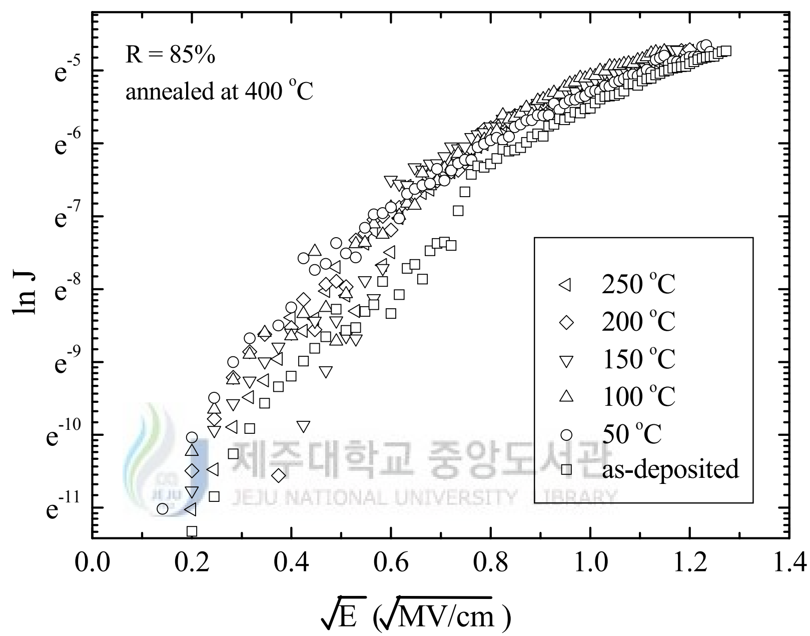

제주대학교 중앙도서관
JEJU NATIONAL UNIVERSITY LIBRARY

Fig. 66. "$\ln J$" versus electric field $\sqrt{E}$: characteristics as a function of measurement temperature for annealed films at 400 ℃ with a BTMSM/(O_2+BTMSM) flow rate ratio of 85 %.

4. Dielectric properties

Dielectric properties of SiOC(-H) films such as bonding angle, dipole moment, and polarizability for different BTMSM/(O_2+BTMSM) flow rate rations have been calculated. The dipole moment can be calculated from charge and bonding length, as expressed in equation

$$\mu = Qd = \delta ed \tag{4-5}$$

where μ is dipole moment, Q is charge, d is bonding length, δ is ionic percent and e is elementary quantum of electricity. In order to investigate the dipole moment of the Si-O-C chain structure as a function of the bonding angle between Si-O and Si-C bonds, we used the following expression,

제주대학교 중앙도서관
JEJU NATIONAL UNIVERSITY LIBRARY

$$\mu_{Si-O-C} = \mu_{Si-O} + \mu_{Si-C} \tag{4-6}$$

Where μ_{Si-O} and μ_{Si-C} are the induced dipole moments of the Si-O and Si-C bonding molecules. The bonding lengths of Si-O of SiO_2 structure and Si-C bonds of SiC structure are 1.60 Å [75]. In carbon incorporated SiOC structure, the bonding length of Si-O bond increased to average 1.90 Å, the bonding length of Si-C bond decreased to average 1.85 Å. The ionic percent of Si-O and Si-C bonds are 0.08 and 0.07, respectively [76]. And then, the dipole moment of Si-O and Si-C bonds are 2.5×10^{-30} Cm and 2.0×10^{-30} Cm, respectively. The dipole moment usually reflects the difference between the electronegativities of the carbon and the oxygen atoms because the dipole moment of Si-O bond is large than that of Si-C bond. The bonding angle

can be calculated from Eq. 4-2.

$$\bar{\nu} = \bar{\nu}_0 \sin\left(\frac{\theta}{2}\right) \tag{4-2}$$

Where θ is the bonding angle between the Si-O and the Si-C bonds. The determined values are summarized in the Table 12. Figure 67 shows the dipole moment as a function of BTMSM/(O_2+BTMSM) flow rate ratio for as-deposited and annealed films at 200, 300 and 400 ℃. It is clearly observed that as the annealing temperature and carbon concentration increased the dipole moment is also increased. It is also observed that the dipole moment of Si-O-C bonding structure is linearly decreased from 1.16 to 1.06×10^{-30} Cm as the flow rate ratio increased from 45 to 85 %. The dipole moment of Si-O-C bonding structure for annealed sample at 400 ℃ is calculated to be 0.97×10^{-30} Cm. The dipole moment of SiOC(-H) film was

제주대학교 중앙도서관

Table 12. The dipole moment of the Si-O-C and chain structure and the bonding angle between Si-O and Si-C bonds.

R (%)	O-Si-C Bonding angle θ (°)				Si-O-C Dipole moment (10^{-30} Cm)			
	RT	200℃	300℃	400℃	RT	200℃	300℃	400℃
45	152.9	153.4	152.9	153.4	1.16	1.14	1.16	1.14
55	153.8	153.8	153.8	154.3	1.13	1.13	1.13	1.11
65	154.3	154.3	154.8	155.3	1.11	1.11	1.10	1.08
75	155.3	155.3	155.8	156.8	1.08	1.08	1.06	1.03
85	155.8	156.3	156.8	159.0	1.06	1.05	1.03	0.96

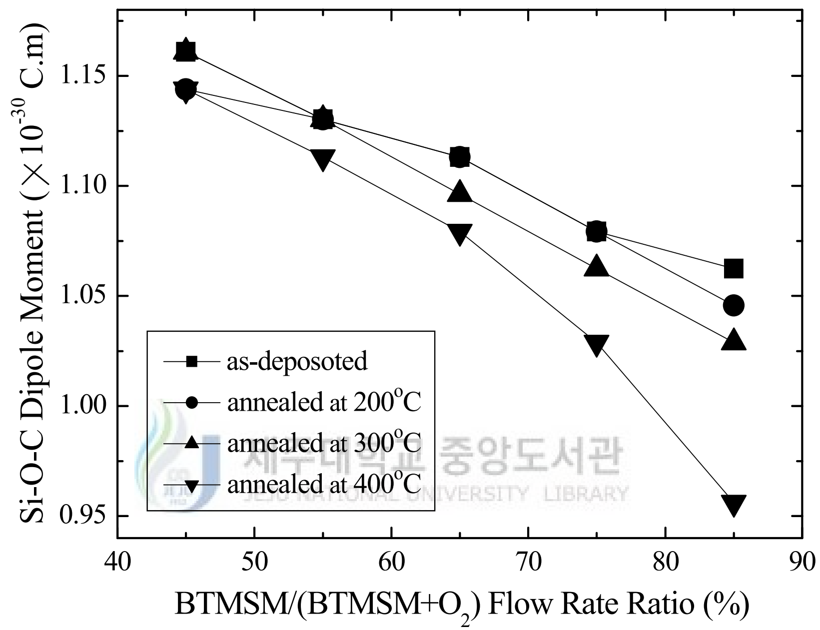

Fig. 67. The dipole moment as a function of BTMSM/(O_2+BTMSM) flow rate ratio for as-deposited and annealed films at 200, 300 and 400 ℃.

제주대학교 중앙도서관
JEJU NATIONAL UNIVERSITY LIBRARY

smaller than that of SiO_2 film and gradually decreased with increasing carbon content incorporated in the film. Because the dipole moment of polyatomic molecules is the vector sum of bond moments, high-symmetry molecules can have a zero dipole moment because the vector sum of their bond moment is zero, even though they have very polar bonds (Si-O bonds). Since the structure of SiO_2 film and [SiO_4] tetrahedron is nearly symmetrical, its dipole moment was about zero. If one of oxygen atom in the [SiO_4] tetrahedral molecule is replaced by carbon, the vector sum of the bond moments will then be non-zero. This is because the dipole moment of SiOC is larger than that of SiO_2. However, the dipole moment of the [SiO_2C_2] tetrahedral molecule, which is formed by the substitution of two carbon atoms for two oxygen atoms in [SiO_4] tetrahedral molecule, is lower than that of the [SiO_3C] tetrahedral molecule. This result is explained by the difference in bond moments. Since the bond moment usually reflects the difference between the electronegativities of the two atoms, the bond moment of Si-O is larger than that of Si-CH_n. The increased number of Si-O bond replacements for Si-C bonds results in the reduction of the sum of bond moments in the molecular unit. Therefore, the drastic decrease in the dipolar polarization of SiOC(-H) with increasing carbon content is attributed to the reduction of the molar dipole moment as well as the dipole density.

Figure 68 shows the function of number density versus the BTMSM/(O_2 +BTMSM) flow rate ratio. It is seen from Fig. 68 that as the annealing temperature increases the number density decreases gradually, thus leading to

a decrease in film density. This result is also clearly evidenced by the reduction of dielectric constant values upon annealing of SiOC(-H) films. It is also noted that as the BTMSM/(O_2+BTMSM) flow rate ratio increases from 45 to 85 % the density of the film correspondingly decreased from 0.84×10^{29} atoms/m^3 to 0.60×10^{29} atoms/m^3. The density of the film for samples annealed at 400 ℃ is calculated to be 0.71×10^{29} atoms/m^3 to 0.48×10^{29} atoms/m^3 as the flow rate ratio increased from 45 to 85 %.

From Fig. 69 it can be seen that the dipolar polarizability gradually decreased when the BTMSM/(O_2+BTMSM) flow rate ratio increased from 45 to 85 %. Also the dipolar polarizability value was found to be more for annealed samples than for as-deposited films. D. shamiryan *et al.* reported that materials with chemical bonds of lower polarizability than Si-O or lower density materials could be combined to get even lower *k* values, where some silica Si-O bonds have been replaced with less polar Si-C bonds [84]. A more fundamental reduction can be achieved by using virtually all nonpolar bonds, such as C-C or C-H, for example, in materials like organic polymers. The addition of CH_3 not only introduces less polar bonds, but also creates additional free volume. Therefore if SiOC(-H) films are constitutively porous, the dielectric constant will decrease.

제주대학교 중앙도서관
JEJU NATIONAL UNIVERSITY LIBRARY

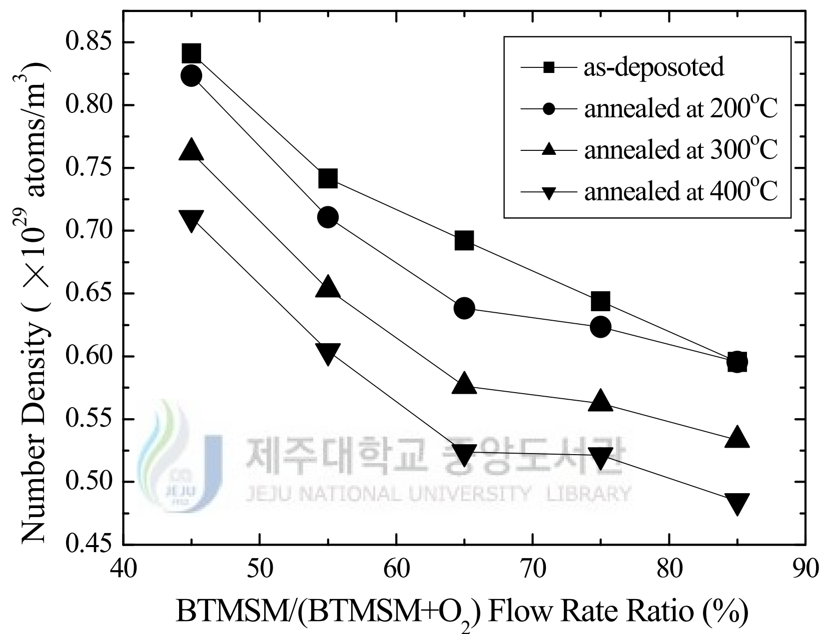

제주대학교 중앙도서관
JEJU NATIONAL UNIVERSITY LIBRARY

Fig. 68. The function of number density to the BTMSM/(O_2+BTMSM) flow rate ratios.

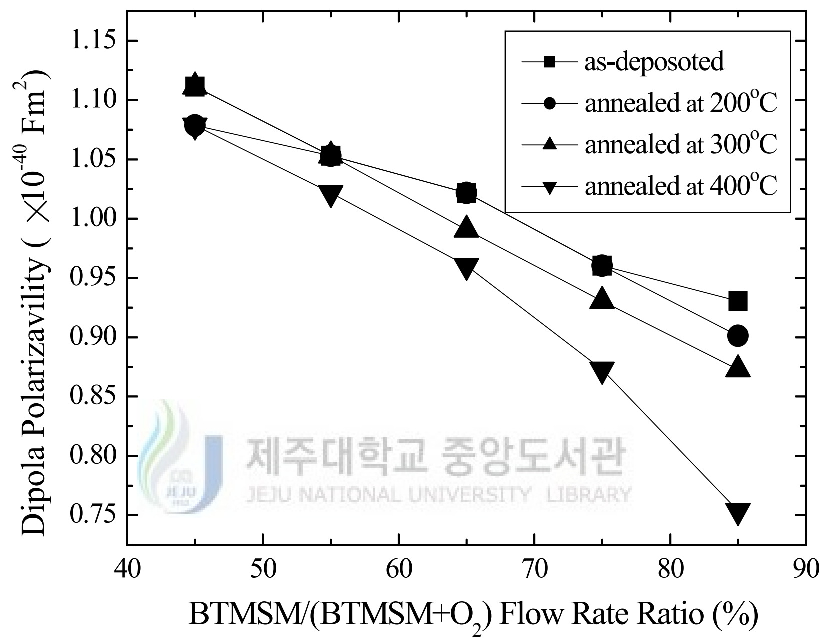

Fig. 69. The calculated the dipolar polarizability as a function of the BTMSM/(O_2+BTMSM) flow rate ratios.

The dielectric constant is a frequency-dependent, intrinsic material property. It is well-known that the dielectric constant is composed of electronic, ionic and dipolar components. The total dielectric constants have been calculated at 1 MHz and the electronic dielectric constant can be obtained from the squares of the refractive indices at 632.8 nm. The dipolar dielectric constants have also been calculated from dipolar polarizability and ionic dielectric constants can be obtained from the total dielectric constant. Figure 70 shows the dielectric constant measured at 1 MHz versus BTMSM/(O_2+BTMSM) flow rate ratios from 45 to 85 %. The dielectric constant of as-deposited SiOC(-H) film is found to be 2.60 for a flow rate ratio of 45%. As the flow rate ratio increases the dielectric constant decreases, and for as-deposited film with an 85 % flow rate ratio the dielectric constant is about 2.30. In the case of samples annealed at 200, 300 and 400 ℃ the dielectric constant decreases gradually when the flow rate ratio increases from 45 to 85 %. The lowest relative dielectric constant of the annealed film with a BTMSM/(O_2+BTMSM) flow rate of 85 % is about 2.18. Thus the flow rate ratio of the SiOC(-H) films strongly influences the dielectric properties of the films. From these results, we can infer that the dielectric constant of the SiOC(-H) composite film depends on the relative carbon content and the pore density. The pore density of the SiOC(-H) film is closely related to the film density. The decrease of the dielectric constant after annealing indicates that a rearrangement of bonding structure in the film results in the formation or enhancement of pre-existing atomic scale nano-pores in the film [21].

제주대학교 중앙도서관
JEJU NATIONAL UNIVERSITY LIBRARY

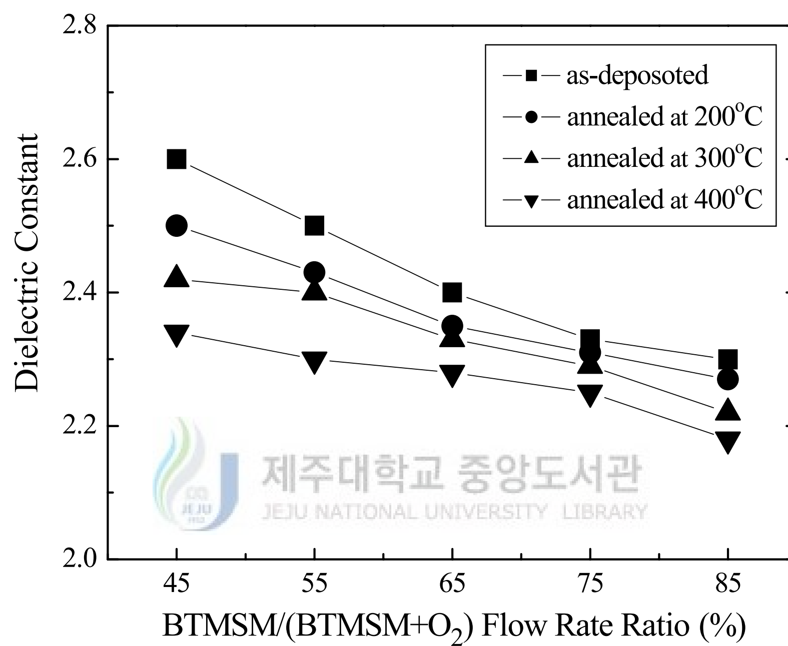

제주대학교 중앙도서관
JEJU NATIONAL UNIVERSITY LIBRARY

Fig. 70. The dielectric constants of as-deposited and annealed SiOC(-H) films with various BTMSM/(O_2+BTMSM) flow rate ratios.

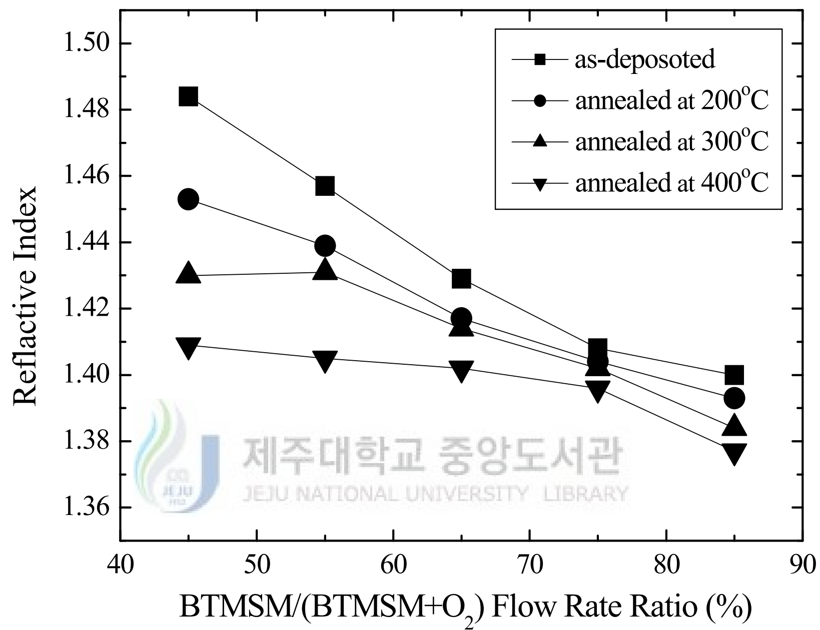

제주대학교 중앙도서관
JEJU NATIONAL UNIVERSITY LIBRARY

Fig. 71. The relationship between the refractive index of as-deposited and annealed SiOC(-H) film with the BTMSM/(O_2+BTMSM) flow rate ratios from 45 to 85 % of SiOC(-H) film.

Fig 71 shows the relationship between the refractive index measured at 632.8 nm with BTMSM/(O_2+BTMSM) flow rate ratios of 45 to 85 % in SiOC(-H) film. It is observed from the experimental results that the refractive index decreases from 1.48 to 1.40 with the increase in the flow rate ratio. It is also seen that the refractive index of annealed films is less than that of as-deposited films. The refractive index of annealed films decreases from 1.41 to 1.38 when the flow rate ratio increases.

Figures 72, 73 and 74 show the dielectric constants affected by electronic, ionic and dipolar componenst of SiOC(-H) films as a function of BTMSM/(O_2+BTMSM) flow rate ratios from 45 to 85 %. It is observed that the contribution of electronic dielectric constants plays a much greater role than does the ionic component of SiOC(-H) films. It is also seen that the electronic dielectric constant is more for as-deposited than for annealed films. The decrease of the electronic polarization in SiOC(-H) films with increasing carbon contents is attributed to the reduction of the dipole moment as well as the film density. However, the reduced electronic contribution has a large influence on reducing the overall dielectric constant because the electronic dielectric constant was responsible for more than 90 % of the total dielectric constant.

제주대학교 중앙도서관
JEJU NATIONAL UNIVERSITY LIBRARY

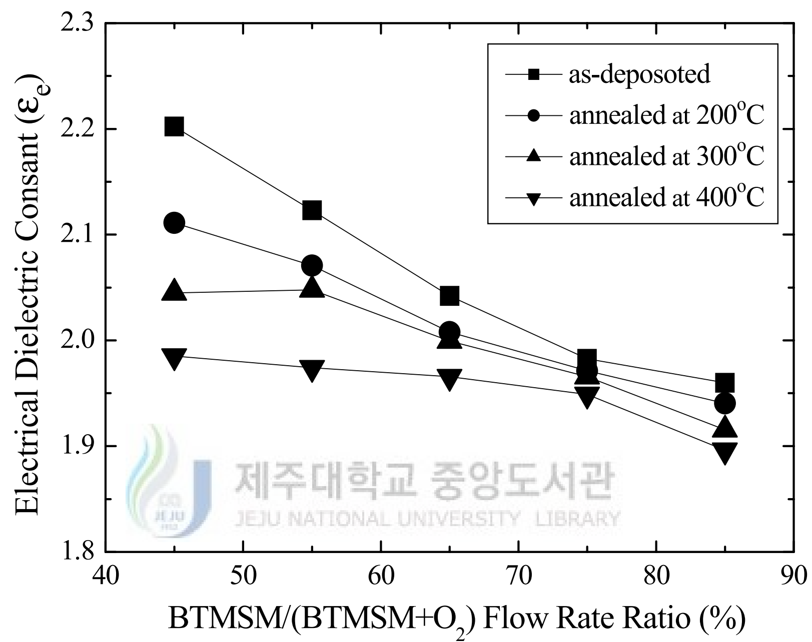

제주대학교 중앙도서관
JEJU NATIONAL UNIVERSITY LIBRARY

Fig. 72. Electronic dielectric constants of as-deposited and annealed SiOC(-H) films as a function of BTMSM/(O_2+BTMSM) flow rate ratios from 45 to 85 %.

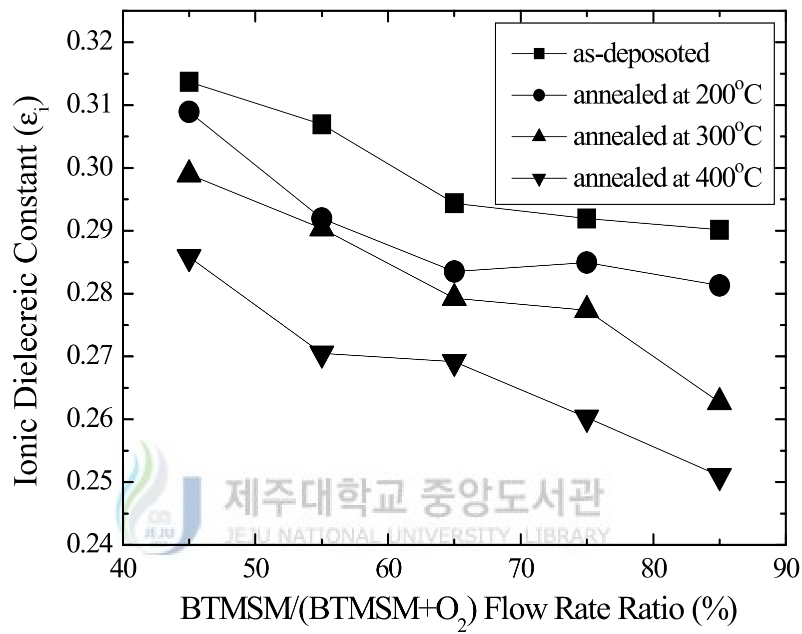

제주대학교 중앙도서관
JEJU NATIONAL UNIVERSITY LIBRARY

Fig. 73. Ionic dielectric constants of as-deposited and annealed SiOC(-H) films as a function of BTMSM/(O_2+BTMSM) flow rate ratios from 45 to 85 %.

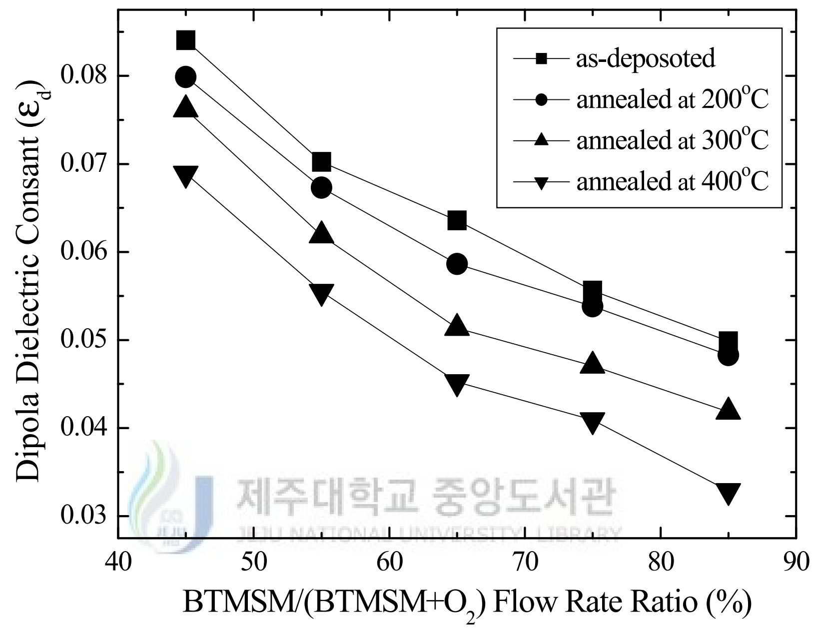

제주대학교 중앙도서관
JEJU NATIONAL UNIVERSITY LIBRARY

Fig. 74. Dipolar dielectric constants of as-deposited and annealed SiOC(-H) films as a function of BTMSM/(O_2+BTMSM) flow rate ratios from 45 to 85 %.

Each dielectric constant value have been listed in Table 13. From these results, we can infer that the dielectric constant of SiOC(-H) film depends on the relative carbon content and pore density. The pore density of SiOC(-H) film is closely related to the film density. The decrease of the dielectric constant after annealing indicates that a rearrangement of bonding structure in the film results in the formation or enhancement of pre-existing atomic scale nano-pores in the film.

Table 13. The dielectric constant arise from electronic, ionic, dipolar and total component of the SiOC(-H) films as a function of the BTMSM/ (O_2+BTMSM) flow rate ratios from 45 to 85 %.

Deposition condition		ε_{total}	$\varepsilon_{electric}$	ε_{ionic}	$\varepsilon_{dipolar}$
45 %	RT	2.600	2.202	0.314	0.084
	200 ℃	2.500	2.111	0.309	0.080
	300 ℃	2.420	2.050	0.299	0.076
	400 ℃	2.340	1.985	0.286	0.069
55 %	RT	2.500	2.123	0.307	0.070
	200 ℃	2.430	2.071	0.292	0.067
	300 ℃	2.400	2.048	0.290	0.062
	400 ℃	2.300	1.974	0.270	0.056
65 %	RT	2.400	2.042	0.294	0.064
	200 ℃	2.350	2.008	0.283	0.059
	300 ℃	2.330	1.999	0.279	0.051
	400 ℃	2.280	1.966	0.269	0.045
75 %	RT	2.330	1.982	0.292	0.056
	200 ℃	2.310	1.971	0.285	0.054
	300 ℃	2.290	1.966	0.277	0.047
	400 ℃	2.250	1.949	0.260	0.041
85 %	RT	2.300	1.960	0.290	0.050
	200 ℃	2.270	1.940	0.281	0.048
	300 ℃	2.220	1.915	0.263	0.042
	400 ℃	2.180	1.896	0.251	0.033

제주대학교 중앙도서관
JEJU NATIONAL UNIVERSITY LIBRARY

Ⅵ. Conclusions

Low-*k* SiOC(-H) films with nano-pore structure were deposited on *p*-type Si(100) substrates using PECVD with a mixture of oxygen gas and bis-trimethylsilylmethane (BTMSM: H_9C_3-Si-CH_2-Si-C_3H_9). FTIR spectroscopy performed in absorbance mode was used to determine the related Si-O and Si-CH_3 bonding configuration in the film, and the bonding structure of the Si-O-C composite films was analyzed using XPS. The mechanical properties such as hardness (H) and elastic modulus (E) were measured by the nano-indentation method. The thickness and refractive index of the deposited Si-O-C composite films were measured by an ellipsometer. The characteristics of nano-pore structure in the SiOC(-H) films were investigated by SANS and GISAXS, and the dielectric constant of the films at 1 MHz was investigated with a metal insulator semiconductor (MIS, Al/SiOC(-H) film/*p*-Si) structure. The concluding remarks are summarized as follows:

제주대학교 중앙도서관
JEJU NATIONAL UNIVERSITY LIBRARY

1) The spectra of the Si-O-Si asymmetric stretching mode for clearly separated Si-O-Si and Si-O-C bonds indicates the existence of a caged Si-C bond, and this is a reflection of the enhanced porosity in the film. Carbon atoms could be incorporated in the SiOC(-H) films during deposition by -CH_3 groups attached to Si atoms in Si-O-Si networks, and the Si-O-C substructure. Some types of CH_n were removed from the bulk of the film due to the annealing process, and some of the Si-O-Si bonds changed into Si-O-C bonds including ring, open and cage links in which C atoms had been incorporated. The bonding structure of the SiOC(-H) film changed

due to the post-annealing and flow rate ratio increases, which could have transformed the substructure from open-linked to ring-linked. The bonding angle between the Si-O and the Si-C bonds increased as the flow rate ratio and the annealing temperature increased. The incorporation of CH_3 groups broke the continuity of Si-O-Si networks and caused nano-pores to be formed due to the aloof force between the CH_3 group and other parts of Si-O-Si links.

2) The chain structure of the SiOC(-H) film consists of Si-O_4, C-Si-O_3, C-H, C-Si and -C-O bonds. The C-Si-O_3 bond increased as a function of flow rate ratio increases and C-Si bonds were chemically shifted towards the lower binding energy side while that of the -C-O bond was also shifted to the lower binding energy side. From these results, we could surmise that some bonds such as Si-O_4 broke and that parts of O atoms were being replaced by C and H atoms, or were being removed from the film, resulting in those atoms appearing in different chemical states and causing some voids to form in the film.

Also, the porosity increase was due to the increasing relative content of Si-O-C ring link forms, in which the CH_3 groups were incorporated in the Si-O-Si bonds. Nano-pores formed due to the aloof force between the CH_3 group and other parts of Si-O-Si bond. The pore generation mechanism during the deposition process seems to come about when the open-linked substructure changes to a ring-linked one, which may be related to the reduction in OH groups and the Si-O-CH_3 groups.

3) The diameter size of pores was distributed from 2.0±0.5 nm, with the average diameter of the most populated pore distributions about 3.0 nm. The average radius of gyration was about 7.0 nm and a relatively narrow size

제주대학교 중앙도서관
JEJU NATIONAL UNIVERSITY LIBRARY

distribution (σ) was about 0.5. The peak pore size increased about 12 % by annealing, but the average size of the pore was almost unchanged. Porosity values of the as-deposited and films annealed at 400℃ with BTMSM/(O_2 +BTMSM) flow rate ratios of 45 and 85 % increased from 37.0 % to 44.8 % and from 46.0 % to 49.7 %, respectively.

4) The hydrogen, oxygen and silicon concentrations of the samples annealed at 400℃decreased less than that of as-deposited samples, 1.5, 1.5 and 0.9 %, respectively. The carbon contents in the film increased 4 % after the SiOC(-H) film was annealed at 400℃. From these results, after annealing treatment, the oxygen concentration decreased because some H_2O was removed from the bulk of the film. The density of as-deposited SiOC(-H) films decreased from 2.42 g/cm^3 to 1.21 g/cm^3 as the flow rate ratios increased from 45 % to 85 %. The density of SiOC(-H) films annealed at 400 ℃ was also calculated as 2.10, 1.75, 1.32 1.04 and 0.98 g/cm^3, respectively, for BTMSM/(BTMSM+O_2) flow rate ratios of 45, 55, 65, 75 and 85 %. It means that the decrease of the film density is due to formation of voids in the film. The decrease in density after annealing indicates that a rearrangement of the bonding structure in the film results in the formation or enhancement of pre-existing atomic scale nano-pores in the film.

5) The hardness values of as-deposited films were 2.6 to 1.6 GPa and those of 400℃annealed films ranged from 2.0 to 0.7 GPa. These values are lower than the hardness values of TEOS-SiO_2 film (8.0~10.0 GPa), but much higher than SiLK film (0.1~0.2 GPa). The increase of BTMSM precursor tends to decrease the hardness because the porosity increases, and the density of the film decreases with

제주대학교 중앙도서관
JEJU NATIONAL UNIVERSITY LIBRARY

increasing carbon content. The obtained elastic modulus values of as-deposited and annealed films decreased as a function of BTMSM/(O_2+BTMSM) flow rate ratios. Elastic modulus values ranged from 26 to 14 GPa for as-deposited films and from 20 to 7 GPa for the films annealed at 400 ℃. These figures are lower than TEOS SiO_2 film (70~90 GPa) but much higher than SiLK film (3~4 GPa). The increase of BTMSM precursor tends to decrease the elastic modulus.

6) The dipole moment of the Si-O-C bonding structure increased in response to increases in annealing temperature as well as the flow rate ratio from 45 to 85%. The dipole moment of the Si-O-C bonding structure for annealed films at 400 ℃ was calculated to be 3.64×10^{-29} Cm. The magnitude of the dipolar polarizability was a very small number on the order of 10^{-40} Fm^2, a negligible value when compared to other dipolar moments. The dipolar polarizability gradually increases as the BTMSM/(O_2+BTMSM) flow rate ratio increases from 45 to 85%. Also the dipolar polarizability value was found to be higher for annealed samples than it was for as-deposited films.

7) The dielectric constants of SiOC(-H) films were calculated for as-deposited and annealed samples. The dielectric constant of as-deposited SiOC(-H) film was found to be 2.60 with a flow rate ratio 45 %. As the flow rate ratio increases the dielectric constant decreases, which explains the lower dielectric constant of 2.30 for as-deposited film with an 85 % flow rate ratio. In the case of annealed samples at 200, 300 and 400℃ the dielectric constant decreases gradually as the flow rate ratioo increases from 45 to 85 %. The lowest relative dielectric constant of the annealed film with

제주대학교 중앙도서관
JEJU NATIONAL UNIVERSITY LIBRARY

a BTMSM/(O_2+BTMSM) flow rate of 85 % was about 2.18. The experimental results show that the refractive index decreased to 1.37 from 1.50 when the flow rate ratio was increased. It was also seen that the refractive index of annealed films decreased to 1.31 from 1.40 when the flow rate ratio was increased. The dielectric constants arise due to electronic and ionic components of SiOC(-H) films in which electronic dielectric constants play a much larger role than that of the ionic components of SiOC(-H) films. When the BTMSM/(O_2+BTMSM) flow rate ratio was increased from 45 to 85%. The electronic dielectric constant was also found to be greater for as-deposited films than for annealed films.

From these results, we can infer that the dielectric constant of SiOC(-H) films depends on relative carbon content and porosity, and that the porosity of SiOC(-H) films is closely related to the film density. The decrease in the dielectric constant after annealing indicates that a rearrangement of bonding structure in the film results in the formation or enhancement of pre-existing atomic scale nano-pores in the film. The SiOC(-H) composited films deposited by the ICPCVD method satisfied the requirement for intermetal dielectric materials for the next generation of ULSI devices. Therefore, a SiOC(-H) composite film deposited using a BTMSM precursor is a very promising low-*k* material due to its excellent thermal stability as well as electrical and mechanical properties.

제주대학교 중앙도서관
JEJU NATIONAL UNIVERSITY LIBRARY

References

[1] M. Morgen, E. Todd, J. H. J. H. Zhao, C. Hu, T. Cho, P. S. Ho, Annu. Rev. Mater. Sci., **30**. 651 (2000).

[2] J. H. Kim, S. H. Seo, S. M. Yun, H. Y. Chang, K. M. Lee and C. K. Choi, Appl. Phys. Lett., **68**, 1507, (1996).

[3] K. Endo, K. Shinoda and T. Tatsumi, J. Appl. Phys., **86**, 2739, (1999).

[4] A. Grill and V. Patel, J. Appl. Phys., **85**, 3314 (1999).

[5] I. Banerjee, M. Harker, L. Wong, P. A. Coon and K. K. Gleason, J. Electrochem. Soc., **146**, 2, 219 (1999).

[6] J. Y. Kim, M. S. Hwang, Y. H. Kim, H. J. Kim and Y. Lee, J. Appl. Phys., **90**, 2469 (2001).

[7] N. P. Hacker, MRS. Bulletin, **22**, 33 (1997).

[8] A. Nara and H. Itoh, Jpn. J. Appl. Phys., **36**, 1477 (1997).

[9] M. J. Lobada, Microelectronic Engineering, **50**, 15 (2000).

[10] C. T. Lin, F. Li and T. D. Manrei, J. Vac. Sci. Technol., **A17(3)**, 735 (1999).

[11] T. H. Kim, M. S. Hwang, J. Y. Kim, and Y. Lee, J. Appl. Phys., **90(7)**, 3367 (2001).

[12] G. Maier, Prog. Polym. Sci., **26**, 3-65 (2001).

[13] A. L. S. Loke, "*Process Integration Issues of Low-Permittivity Dielectrics with Copper for High-Performance Interconnects*", Ph. D. Dissertation, Stanford, (1999).

제주대학교 중앙도서관
JEJU NATIONAL UNIVERSITY LIBRARY

[14] T. Ohba, J. FUJITSU Sci. Tech., **38**, 17 (June 2002).

[15] C. L. Borst, V. Korthuis, G. B. Shinn, J. D. Luttmer, R. J. Gutmann, W. N. Gill, Thin Soil Films, **385**, 281 (2001).

[16] L. Peters, Semiconductor International, **21**(10), 64 (1998).

[17] R. H. Havemann, A. Hutchby, proceedings of the IEEE, **89**, 586 (2001).

[18] Y. H. Kim, "*Deposition and Characterization of Low-Dielectric-Constant SiOC Thin Fims for Interlayer Dielectrics of Multilevel Interconnection*", Ph. D. Dissertation, Seoul National University, (2002).

[19] M. Gotuaco, P. W. Lee, L. Q. Xiz and E. Yieh, Applied Materials, Semiconductor Fabtech, 179.

[20] K. H. Block, H. L. Rayle, *Semiconductor International*, 118 (2002).

[21] N. Aoi et al., "*Interconnect*", in *International Technology Roadmap for Semiconductors*, For updated information, (2004).

[22] N. Aoi et al., "*Interconnect*", in *International Technology Roadmap for Semiconductors*, 2003 Edition.

[23] R. Ho and Horowitz, *International Technology Roadmap for Semiconductors*, 165 (1999).

[24] L. Peters, *Semiconductor International*, **23** (6), 6108 (2000).

[25] N. P. Hacker, MRS Bullentin, **22** (10), 33 (1997).

[26] P. R. Resnick, Polymer Preprints, Division of Polymer Chemistry, American Chemical Society, **31**, 312 (1990).

[27] E. I. du Pont de Nemoues and Company, DuPont Teflon Amorphous Fluropolymer, product data sheet (2002).

제주대학교 중앙도서관
JEJU NATIONAL UNIVERSITY LIBRARY

[28] G. Mwssner, I. Turnik, J. W. Balde, and P. Garrou, editors, "*Thin Film Multichip Modules*", A Technical Monograph of the International Society for Hybrid Microelectronics, (1992).

[29] Dow Chemical Company, Benzocyclobutene Technical data sheet, Midland, MI 48642.

[30] L. Peters, *Semiconductor International*, **21** (10), 64 (1998).

[31] N. H. Hendricks, K. S. Lau, A. R. Smith, and W. B. Wan, Materials Research Society Proceedings, **381**, 59 (1995).

[32] J. H. Golden, C. J. Hawker, and P. S. Ho, *Semiconductor International*, **24** (5), 79 (2001).

[33] P. Singer, *Semiconductor International*, **23** (5), 44 (2000).

[34] A. F. Braun, *Semiconductor International*, **23** (6), 128 (2000).

[35] C. Jin, J. D. Luttmer, D. M. Snith, and T. Ramos, MRS Bulletin, **22** (10), 39 (1997).

[36] H. S. Nalwa, editor, *Handbook of Low and high Dielectric Constant Materials and Their Applications: Materials and Processing*, Academic Press, Inc., San Diego, 1999.

[37] E. D. Birdsell and R. A. Gerhardt, in *Low Dielectric Constant Materials Ⅳ*, C. Chiang, P. S. Ho, T. M. Lu, and J. T. Wetzel, Materials Research Society Symposium, Warrendale, PA, **511**, 111 (1998).

[38] S. Nitta, A. Jain, V. Pisupatti, W. Gill, P. Wayner, and J. L. Plawsky, in *Low Sielectric Constant Materials Ⅳ*, C. Chiang, P. S. Ho, T. M. Lu, and J. T. Wetzel, editor, Materials Research Society Symposium,

제주대학교 중앙도서관
JEJU NATIONAL UNIVERSITY LIBRARY

Warrendale, PA, **511**, 99 (1998).

[39] Honeywell Advanced Microelectronic Materials, Nanoglass, product bulletin (2000).

[40] T. Ramos, K. Rhoderick, R. Roth, L. Brungardt, S. Wallace, J. Drage, J. Dunne, D. Wndisch, R. Katsanes, N. Viernes, and D. M. Smith, in *Low Dielectric Constant Materials Ⅳ*, C. Chiang, P. S. Ho, T. M. Lu, and J. T. Wetzel, Materials Research Society Symposium, Warrendale, PA, **511**, 105 (1998).

[41] C. C. Cho, D. M. Smith, and J. Anderson, Materials Chemistry and Physics, **42**, 91 (1995).

[42] C. Jin and J. Wetzel, *Proceeding of the International Interconnect Technology Conference*, San Francisco, CA, (June 2000).

[43] Q. Han, W. Chen, C. Waldfried, O. Escorica, N. M. Sbrokey, T. J. Bridgwater, E. S. Moyer, and I. Berry, *Proceedings of the International Interconnect Technology Conference*, IEEE Electron Devices Society, 171 (2001).

[44] A. Gill and D. A. Neumayer, J. Appl. Phys., **94**, 6697 (2003).

[45] K. Max, M. R. Barklanov, D. Shamiryan, F. Iacopi, S. H. Brongersma, Z. S. Yanovitskaya, J. Appl. Phys., 93, 8793 (2003).

[46] J. D. Livingston, *Electronic Properties of Engineering Materials* (Wiley, New York, 1999), Chapter 4.

[47] P. W. Atkins, *Physical Chemistry*, 5th ed. (Oxford University Press, New York, 1994).

제주대학교 중앙도서관
JEJU NATIONAL UNIVERSITY LIBRARY

[48] R. P. Feynman, R. B. Leighton, and M. Sands, in *The Feynman Lectures on Physics* (Adison Wesley, Reading, PA, 1996), Chapter 11.

[49] P. W. Atkins and R. S. Friedman, *Molecular Quantum Mechanics*, 3rd ed. (Oxford University Press, New York, 1997), Chapter 16.

[50] L. W. Hrubesh, L. E. Keene, and V. R. Latorre, J. Mater, Res, 8, 1736 (1993).

[51] C. M. Sim, "*Cu diffusion characteristics of low-k dielctrics deposited by PECVD*", Ph. D. Dissertation, SungKyunKwan University, chapter 1 (2002).

[52] W. D. Kingery, H. K. Bowen, and D. R. Uhlmann, *Introduction to Ceramics 2nd edition*, Chapter 1 and 18 (1960).

[53] S. M. Han and E. S. Aydil, J. Appl. Phys., **83**, 2172 (1998).

[54] W. C. Oliver, G. M. Pharr, J. Mater. Res. **7**(6), 1564(1992).

[55] I. N. Sneddon, Int. J. Engng. Sci. **3**, 47 (1965).

[56] R. B. King, Int. J. Solids Structures, **23**(12), 1657 (1987).

[57] J. C. Hay, A. Bolshakov, G. M. Pharr, J. Mater. Res. **14**(6), 2296 (1999).

[58] J. L. Hay, *Proceedings of the SEM IX International Congress on Experimental Mechanics*, Society for Experimental Mechanics, Bethel, CT, 665 (2000).

[59] M. R. VaLandingham, J. S. Villarrubia, W. F. Guthrie, and G. F. Meyers, Macromol. Symp., **167**, 15 (2001).

[60] Y. S. Kim, H. J. Woo, Application and Status of Ion Beam Analysis,

제주대학교 중앙도서관
JEJU NATIONAL UNIVERSITY LIBRARY

(2000).

[61] W. Hong, "*A Study on the Development of A High-Energy Heavy-Ion TOF-ERD and Its Application to Advanced Materials*" Ph. D. Dissertation, Seoul National University, (1997).

[62] Y. Fan, H. R. Bentley, K. R. Karthan, P. Clem, Y. F. Lu, and C. J. Brinker, J. Non-Cryst. Solids, **285**, 79 (2001).

[63] C. J. Brinker, R. Selgal, S. L. Hietala, R. Deshpande, D. M. Smith, D. Loy and C. S. Ashley, J. Member. Sci. **94**, 85 (1994).

[64] S. M. Sze, *Physics of Semiconductor Devices 2nd Edition*, Wiley Inter. Science, chapter 7.

[65] P. N. Sen and M. F. Thrope, Phys. Rev., **B15**, 4030 (1997).

[66] G. Lucovsky, Philos. Mag., **B39**, 513 (1979).

[67] E. J. Shin, B. S. Seong, Y. S. Han, K. P. Hong, C. H. Lee and H. Kang, J. Appl. Cryst., **36**, 624 (2003).

[68] S. Y. Jing, H. J. Lee and C. K. Choi, J Korean Phys. Soc., 41, (2002).

[69] C. S. Yang, Y. H. Yu, K. M. Lee, H. J. Lee and C. K. Choi, Thin Solid Films, **435**, 166 (2003).

[70] P. N. Sen and M. F. Thorpe, Phys. Rev., **B15**, 4030 (1997).

[71] G. Lucovsky, Philos. Mag., **B39**, 513, (1979).

[72] A. Grill and V. Patel, Appl. Phys. Lett., **79**, 803, (2001).

[73] Y. H. Kim, S. K. Lee and H. J. Kim, J. Vac. Sci. Technol., A, **18**, 1216 (2000).

[74] S. Y. Jing, C. K. Choi and H. J. Lee, JKPS, **39**, S302, (2001).

제주대학교 중앙도서관
JEJU NATIONAL UNIVERSITY LIBRARY

[75] H. Kitoh, M. Muroyama, M. Sasaki, M. Iwasawa and H. Kimura, Jap. J. Appl. Phys., **35**, 1464 (1996).

[76] Y. Uchida, K. Taguchi, T. Nagai, S. Sugahara. and M. Matsumura, Jap. J. Appl. Phys., **37**, 6396 (1998).

[77] E. J. Shin, B. S. Seong, Y. S. Han, K. P, Hong, C. H. Lee and H. J. Kang, J. Appl. Cryst., **36**, 624 (2003).

[78] Q. Wang, C. G. Pantano, and J. F. Annett, Phys. Stat. Sol., (b) **216**, 909, (1999).

[79] B. D. Lee, J. H. Yoon, W. T. Oh, Y. T. Hwang, K. Y. Heo, K. S. Jin, K. W. Kim and M. H. Lee, Macromolecules, **38**, 3395 (2005).

[80] R. J. Abraham, G. H. Grant, J. Computational Chemistry, **9**, 7, 709 (2004).

[81] R. K. Laxman, N. H. Hendricks, B. Arkles, T. A. Tabler, Semiconductor International, 23 (2000).

[82] A. Gill, V. Patel, K. P. Rodbell, E. Huang, M. R. Baklanov, K. P. Mogilnikov, M. Toney and H. C, Kim, J. of Appl. Phys., **94**, 3427 (2003).

[83] M. Gostein, A. Mazurenko, A. Mazenev, M. T. Schulberg, micro magazine, (2004).

[84] D. Shamiryan, T. Abell, F. Iacopi, and K. Max, materials today, 34 (2004).

제주대학교 중앙도서관
JEJU NATIONAL UNIVERSITY LIBRARY

List of related publications

1. Publications-International

1) **Kyoung Suk Oh**, Chi Kyu Choi and Heon-Ju Lee, Nano Pore Structure of Low-k SiOC(-H) Films Measured by Small Angle Neutron Scattering, J. of the Korean Physical Society, **45**, 855 (2004).

2) Teresa OH, **Kyung Suk Oh**, Kwang-Man Lee, and Chi Kyu Choi, Correlation between the dielectric constant and X-ray diffraction pattern of Si-O-C thin films with hydrogen bond, Thin solid films, **468**, 316 (2004).

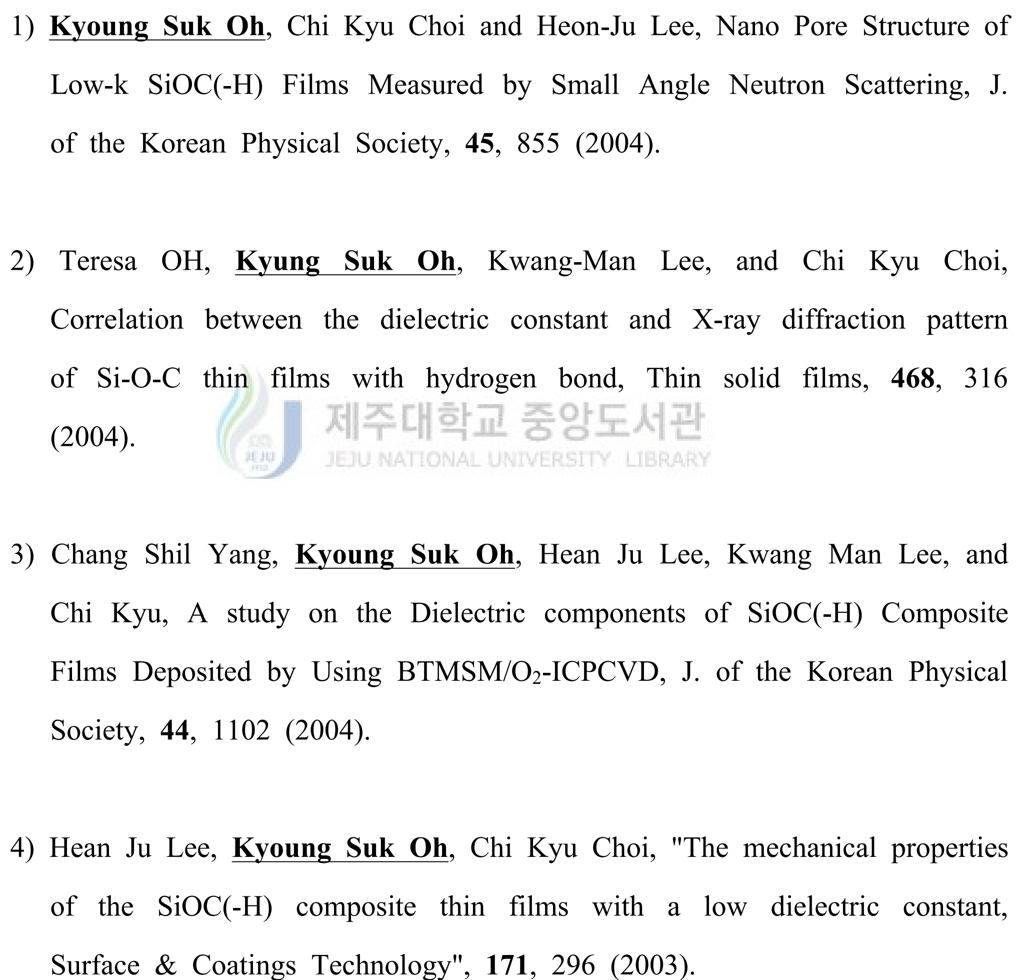
제주대학교 중앙도서관
JEJU NATIONAL UNIVERSITY LIBRARY

3) Chang Shil Yang, **Kyoung Suk Oh**, Hean Ju Lee, Kwang Man Lee, and Chi Kyu, A study on the Dielectric components of SiOC(-H) Composite Films Deposited by Using BTMSM/O_2-ICPCVD, J. of the Korean Physical Society, **44**, 1102 (2004).

4) Hean Ju Lee, **Kyoung Suk Oh**, Chi Kyu Choi, "The mechanical properties of the SiOC(-H) composite thin films with a low dielectric constant, Surface & Coatings Technology", **171**, 296 (2003).

5) **Kyoung Suk Oh**, Shou-Yong Jing and Chi Kyu Choi, Kwang Man Lee, Heon-Ju Lee, Formation and Characteristics of Fluorinated Amorphous Carbon Films Deposited by CF_4/CH_4 ICPCVD, Journal of Korean Physical Society, **39**, 291 (2001).

6) Chang Shil Yang, **Kyoung Suk Oh**, Jai Yon Ryu, Doo Chul Kim, Jing Shou-Yong, Chi Kyu Choi, Heon-Ju Lee, Se Hun Um, Hong Yong Chang, A study on the formation and characteristics of the Si-O-C-H composite thin films with low dielectric constant for advanced semiconductor devices, Thin Solid Films, Elsevier, **390**, 113 (2001).

7) S. M. Yun, H. Y. Chang, **K. S. Oh**, C. K. Choi, Low-Dielectric constant Film deposition with various Gases in a helicon plasma Reactor, Jap. J. of Appl. Phys., **38**, 4531 (1999).

8) **Kyoung Suk. Oh**, M .S. Kang, K .M. Lee, D. S .Kim, C. K. Choi, Formation and characterization of the fluorocarbonated-SiO_2 films by O_2/FTES-helicon plasma chemical vapor deposition, Thin Solid Films, **345**, 45 (1999).

제주대학교 중앙도서관
JEJU NATIONAL UNIVERSITY LIBRARY

2. Conference presentation - International

1) **Kyoung Suk Oh** and Chi Kyu Choi, A Study on the SiOC(-H) Films with Nano-pore Structure Deposited by ICPCVD, International Symposium on Dry Process, 5-12, Ramada Plasza Jeju Hotel, Jeju, Korea, (2005).

2) **Kyoung Suk Oh** and Chi Kyu Choi, Post-Annealing Effect on the SiOC(-H) Conposite Film Deposited by Plasma Enhanced Chemical Vapor Deposition, The 4th International Conference on Advanced Materials and Devices, PLS-P03, Ramada Plasza Jeju Hotel, Jeju, Korea, (2005).

3) K. Meera, **K. S. Oh**, C. S. Yang, H. J. Ko and C. K. Choi, Study of the Bonding Structure due to Post Annealing of Nano-pore SiOC(-H) Films Deposited by UV-Source Assisted PECVD, cTeresa Oh, Kwang Man Lee and Chi Kyu Choi, Hydrogen Bonding of Low-k Materials Deposited by ICPCVD, The 12th Seoul International Symposium on the Physics of Semiconductors and Applications-2004, The Korean Physical Society, Hotel Hyundai, Gyeongju, Korea, (2004).

제주대학교 중앙도서관
JEJU NATIONAL UNIVERSITY LIBRARY

4) **K. S. Oh**, H. J. Lee and C. K. Lee, Structural Properties of Nano-pore Si-O-C-(-H) Composite films by ICPCVD Method, The 12th Seoul International Symposium on the Physics of Semiconductors and Applications-2004, The Korean Physical Society , Hotel Hyundai,

Gyeongju, Korea, (2004).

5) **Kyoung Suk Oh**, Heon Ju and Chi Kyu Chopi, A Study on the Carbon Doped Silicon Oxide Films with Nano-pore Structure Deposited by ICPCVD, 3rd International Sympsium on Practical Sur4face Analysis, and 5th Korea-Japan International Symposium on Surface Analysis,The Surface Analysis Society of Japan and The Korean Vacuum Society, Seogwipo Kal Hotel, Jeju, (2004).

6) **Kyoung Suk Oh**, Chang Sil Yang, Heon Ju Lee and Chi Kyu Choi, The mechanical properties of the SiOC(-H) composite thin films as annealing process, ISPP-2004 Proceedings of the 5th International Symposium on Pulsed Power and Plasma Applications, Korea Electrotechnology Research Institute(KERI), p396-400, Chang-Won, KOREA, (2004).

7) **Kyoung Suk Oh**, Heon-Ju Lee and Chi Kyu Choi, A Study on the Carbon Doped Silicon Oxide Films with Nano-pore Structure Deposited by ICPCVD, 3rd International Symposium on Practical Surface Analysis and 5th Korea-Japan International Symposium on Surface Anlysis, The Surface Analysis Society of Japan and The Korean Vacuum Society, P-50, Seogwipo KAL Hotel, Jeju, Korea, (2004).

8) **K. S. Oh** and C. K. Choi, Electrical Stability of the Organic-Inorganic

제주대학교 중앙도서관
JEJU NATIONAL UNIVERSITY LIBRARY

Material with Low-k Dielectric Constant Deposited by ICPCVD Method, The 30th International Conference on Plasma Science, IEEE, 6PB12, Lotte Hotel, Jeju, Korea (2003).

9) **Kyoung Suk Oh**, Young Hun Yu, Kwang Man Lee, Heon Ju Lee and Chi Kyu Choi, The Effects of Plasma Treatment on Si-O-C(-H) Composite Films with Nano-pore Structure, The 4th Asian-European International Conference on Plasma Surface Engineering(AEPSE 2003), Korea Vacuum Society, Japan Institute of Applied Physics, Ramada Plaza Jeju Hotel, Jeju, Korea, 133 (2003).

10) **Kyoung Suk Oh** and Chi Kyu Choi, Electrical and Thermal Stability of the Low-k Material, 11th Asia-Pacific Conference on Non-Destructive Testing 2003, The Korean Society for Nondestructive Testing, Lotte Hotel Jeju, Korea, 53 (2003).

11) **Kyoung Suk Oh**, Chang Sil Yang, Chi Kyu Choi, A Study on the Formation and Characteristics of the Si-O-C Films with Nano-pore Structure by High Density Plasma Chemical Vapor Deposition, 12th Gaseous Electronics Meeting, Batemans Bay, NSW, Murramarang Resort, The Australian National University, Australia, (2002).

12) Chang Shil, **Kyoung Suk Oh** and Chi Kyu Choi, The chemical bond

제주대학교 중앙도서관
JEJU NATIONAL UNIVERSITY LIBRARY

structure investigation on the Si-O-C composite films with low dielectric constant deposited by high density plasma chemical vapor deposition, 2002 IEEE international Conference on Plasma Science, Banff, Alberta, Canada, (2002).

13) H. J. Lee, **Kyoung Suk Oh** and C. K. Choi, The mechanical properties of the Si-O-C(-H) composite low dielectric constant thin films, Joint International Plasma Symposium of 6th APCPST, 15thSPSM, OS2002 & 11th KAPRA, Jeju Korea, (2002).

14) Teresa Oh, **Kyoung Suk Oh**, Young Hun Yu, Kwang Man Lee, Chi Kyu Choi, A study on the structure of Si-O-C(-H) Thin Film with Nano-size pore by ICPCVD, The 3rd International Mesostructured Materials Symposium, Kal Hotel, Jeju, Korea, (2002).

15) **Kyoung Suk Oh**, Shou-Yong Jing and Chi Kyu Choi, Kwang Man Lee, Heon-Ju Lee, Formation and Characteristics of Fluorinated Amorphous Carbon Films Deposited by CF_4/CH_4 ICPCVD, Journal of Korean Physical Society, Korea, **39**, 291 (2001).

16) Chang Shil Yang, **Kyoung Suk Oh**, Jai Yon Ryu, Doo Chul Kim, Jing Shou-Yong, Chi Kyu Choi, Heon-Ju Lee, Se Hun Um, Hong Yong Chang, A study on the formation and characteristics of the Si-O-C-H

제주대학교 중앙도서관
JEJU NATIONAL UNIVERSITY LIBRARY

composite thin films with low dielectric constant for advanced semiconductor devices, Thin Solid Films, Korea, **390**, 113 (2001).

17) **Kyoung Suk Oh**, Chang Sil Yang, Gun Sam Kang, Chi Kyu Choi, Low-k Organic-Inorganic materials Composite Films deposited by Inductively Coupled Plasma Chemical Vapor Deposition, The 1st international Symposium on Advanced Plasma Surface technology, CAPST, KVC, KMRS, Korea, (2001).

18) **Kyoung Suk Oh**, Chang Sil Yang, Heon Ju Lee, Chi Kyu Choi, Low-Dielectric constant films as an IMD by CF_4/CH_4-ICPCVD, The 2nd International Symposium on Pulsed Power and Plasma Applications, Korea Electrotechnology Research Institute, Korea, 363 (2001).

19) Kwang-Man Lee, **Kyoung, Suk Oh**, Chi Kyu Choi, A Study on the Formation and Characteristics of Low Dielectric Materials for Advanced Semiconductor Devices, 2001 Korean-Japan Joint Workshop on Advanced Semiconductor Processes and Equipments, KPS, KMRS, Korea, (2001).

20) **Kyoung Suk Oh**, Kwang-Man, Chi Kyu Choi, A Formation and Characteristics of the Fluorinated amorphous Carbon Films with Low Dielectric Constant by HDPCVD, 2001 ASIA-PACIFIC Workshop on Fundamental and Application of Advanced Semiconductor devices, The

제주대학교 중앙도서관
JEJU NATIONAL UNIVERSITY LIBRARY

Institute of Electronics Engineers of Korea(IEEK), The Institute of Electronics, Information and Communication Engineers(IEICE) of Japan, IEEE Electron Device Society Korea and Tokyo, 85 (2001).

21) C. K. Choi, **K. S. Oh**, S-Y Jing, H. Y. Chang, Formation and Characteristics of the Si-O-C-H composite Films with low dielectric constant deposited by O_2/BTMSM ICPCVD, Pulsed Power Plasma Science(PPPS) 2001, The 28th IEEE International Conference on Plasma Science and the 13th IEEE International Pulsed Power Conference, IEEE, Jeju, Korea, 297 (2001).

22) S. Y. Jing, **K. S. Oh**, C. S. Yang, C. K. Choi, A Study on the Formation of the Low Dielectric constant Materials by High Density Plasma CVD method, The 3rd International Symposium on the Advanced Functional Materials in the North-East Region(AFMNER) Atomic-Scale Surface Research Center, Korea Science and Engineering Foundation, Korea, National natural Science Foundation of China, China, (2000).

23) Jai, Yon Ryu, Doo Chul Kim, **Kyoung Suk Oh**, Min Sung Kang, Chang Shil Yang, Shou Yong Jing, Chi Kyu Choi, Se Hun Um, Hong Young Chang, Study on the Formation and Characteristics of the Black-diamond Thin Film with loww dielectric constant by BTMSM/O_2-ICPCVD, The 5th Asia-Pacific Conference on Plasma Science & Technology(APCPST),

제주대학교 중앙도서관
JEJU NATIONAL UNIVERSITY LIBRARY

The 13th Symposium on Plasma Science for Materials, APCPST, Dalian, China, (2000).

24) **<u>Kyoung Suk Oh</u>**, Min Sung Kang, Chang Shil Yang, Shou Yong Jing, Heon Ju Lee, Chi Kyu Choi, Se Hun Um, Hong Young Chang, Invited Talk, A Study on the Formation and Characteristics of the Fluorinated amorphous Carbon Film deposited by CF_4/CH_4-ICPCVD, 5th Asia-Pacific Conference on Plasma Science & Technology(APCPST), 13th Symposium on Plasma Science for Materials, APCPST, Dalian, China, (2000).

25) Shou Yong Jing, **<u>Kyoung Suk Oh</u>**, Chang Shil Yang, Chi Kyu Choi, A Study on the Formation and Characteristics of the Organic-inorganic material with low-k dielectric constant deposited by High Density Plasma Chemical Vapor, The 10th Seoul International Symposium on the Physics of Semiconductors and Applications-2000(ISPSA 2000), The Korean Physical Society, The Office of Naval Research, Jeju, Korea, 137 (2000).

26) **<u>Kyoung Suk Oh</u>**, Chang Shil Yang, Shou Yong Jing, Min Sung Kang, Heon Ju Lee, Chi Kyu Choi, Se Hun Um, Hong Young Chang, Thermal Stability of Fluorinated amorphous carbon Films with a Low-Dielectric Constant deposited by CF_4/CH_4-ICPCVD, The 10th Seoul International Symposium on the Physics of Semiconductors and Applications-200(ISPSA 200), The Korean Physical Society, The Office of Naval Research, Jeju,

제주대학교 중앙도서관
JEJU NATIONAL UNIVERSITY LIBRARY

Korea, 186, (2000).

27) **Kyoung Suk Oh**, Chang Shil Yang, Chi Kyu Choi, A Study on the Formation and Characteristics of Low Dielectric Materials for Advanced Semiconductor Devices, The Sino-Korean International Symposium on Thin film Materials: Emerging Technologies for Thin Film materials, Dalian, Natural Science Foundation of China, Korea Science and Engineering Foundation, China, 7 (2000).

28) Min Sung Kang, **Kyoung Suk Oh**, Chi Kyu Choi, Se Hun Um, Hong Young Chang, A Study on the Formation and Characteristics of a-Fluorinated Carbon Film by CF_4/CH_4-ICPCVD, 197th Society meeting, Fifth international symposium on low and high dielectric constant materials : materials science, processing, and reliability issues, The Electrochemical Society, Canada, Toronto, 90 (2000).

29) **K. S. Oh**, C. S. Yang, C. K. Choi, A Study on the Formation of the Low Dielectric Materials by High Density Plasma Chemical Vapor Deposition, The meeting of the Int'l. Conf. on Advanced Materials and Devices'99, Seoul Korea, 170 (1999).

30) M. S. Kang, K. S. Oh, C. K. Choi, S. M. Yun, H. Y. Chang, Formation and Characteristics of the C:F-SiO_2 Films by O_2/FTES-ICPCVD", the 195th ECS, Seattle, USA, 164 (1999).

제주대학교 중앙도서관
JEJU NATIONAL UNIVERSITY LIBRARY

3. Conference Presentation - Domestic

1) 김태언, Xu Jun, 오경숙, 고호정, 양창실, 강권삼, 최치규, ICPCVD 방법으로 형성한 저유전 SiOC(H) 박막의 특성에 관한 분석, 한국물리학회, 연세대학교, **21**, 75 (2003).

2) 양창실, Xu Jun, 오경숙, 고호정, 고성범, 강권삼, 김태언, 최치규, A study on the influence of carbon doped silicon oxide films by thermal treatment, 한국물리학회, 연세대학교, **21**, 75 (2003).

3) 오경숙, 김태언, 최치규, Electrical Stability of the Low Dielectric Constant Material by ICPCVD Method, 한국물리학회, 연세대학교, **21**, 250 (2003).

제주대학교 중앙도서관
JEJU NATIONAL UNIVERSITY LIBRARY

4) 오경숙, 양창실, 유영훈, 이헌주, 이광만, 최치규, A Study on the Formation and Characteristics of the Si-O-C Films with Nano-pore Structure by ICPCVD, 한국물리학회, 부산시 컨벤션센터, **20**, 121 (2002).

5) 양창실, 오경숙, 최치규, HDP-CVD 방법으로 증착한 Si-O-C(-H) 박막의 구조분석, 한국진공학회, 성균관 대학교, 128 (2002).

6) 오데레사, 오경숙, 최치규, BTMSM/O_2의 혼합된 precursor를 사용한 nano-pore의 유무기 하이브리드 구조 저유전 박막의 특성분석, 한국진

공학회, 성균관 대학교, 130 (2002).

7) 오경숙, 최치규, 이광만, ICPCVD 방법에 의한 Nano-pore형 저유전 박막의 형성, 첨단기술연구소, 제주대학교 첨단기술연구소 논문집, **12**, 349 (2001).

8) Shou-Yong Jing, 오경숙, 최치규, The chemical bond structure investigation on Si-O-C(-H) composite low dielectric constant thin films, 첨단기술연구소, 제주대학교 첨단기술연구소 논문집, **12**, 31 (2001).

9) 오경숙, 이헌주 최치규, O_2/BTMSM-ICPCVD 방법에 의한 Si-O-C-H 박막의 형성과 특성, 2001 KAPRA &KPS/DPP joint Workshop, Korea Accelerator and Plasma Research Association, Korea Physical Society, Division of Plasma Physics, (2001).

11) 오경숙, 최치규, 이광만, ICPCVD 방법에 의한 유무기 하이브리드 저유전 박막의 형성, 한국통신학회, 한국전자공학회, 대한 전기학회 제주지부, 제주대 첨단기술연구소, 65 (2001).

12) 최치규외 5인, ICP-CVD 방법을 이용한 a-C:F 저유전율 박막형성, Bulletin of Korean Physical Society, **18(1)**, 103 (2000).

13) 최치규외 5인, 알카리토 금속 산화물과 희토류금속 산화물의 화합물로 이루어진 다층구조의 AC-PDP 보호막의 적층효과, Bulletin of Korean Physical Society, **18(1)**, 103, (2000).

제주대학교 중앙도서관
JEJU NATIONAL UNIVERSITY LIBRARY

14) 최치규외 4인, BTMSM precursor를 고밀도플라즈마 CVD에 의한 저유전율 박막형성, Bulletin of Korean Physical Society, **18(1)**, 102 (2000).

15) **Kyoung Suk Oh**, Min Sung Kang, Duk Soo Kim, Kwang Man Lee, Chi Kyu Choi, Seok Min Yun, Hong Young Chaqng, Kun Ho Kim, A Study on the Formation and Characteristics of Low Dielectric Materials for Advanced Semiconductor Devices, The 6th Joint Symposium of Cheju national University and Nagasaki University on Science and Technology, Cheju National University, 40 (2000).

16) 최치규, 강민성, 오경숙, 이유성, 오대현, 황찬용, 손종원, 이정용, 김건호, 고밀도플라즈마 CVD 방법에 의한 TiN barrier metal 형성과 특성, 한국재료학회지, **9**, 825 (1999).

17) 오대현, 강민성, 오경숙, 이광만, 변종철, 황찬용, 손정원, 최치규, 고밀도 플라즈마 CVD 방법에 의한 TiN barrier metal 형성과 특성, 한국진공학회, 성균관대, 105 (1999).

18) 오경숙, 강민성, 최치규, 이광만, 김건호, O_2/FTES-ICPCVD 방법에 의한 Fluorocarbonated-SiO_2 박막형성, 한국진공학회, 제주대, 105 (1999).

19) 오대현, 강민성, 오경숙, 양창실, 양두훈, 이광만, 변종철, 최치규, 김건호, ICP-CVD 방법에 의한 TiN Diffusion Barrier Thin Film 형성, 한국진공학회, 제주대, 119 (1999).

제주대학교 중앙도서관
JEJU NATIONAL UNIVERSITY LIBRARY

초 록

차세대 ULSI 소자의 Cu/Low-k 층간 절연막으로 적용될 저유전 물질로 SiOC(-H) 박막을 BTMSM (H_9C_3-Si-CH_2-Si-C_3H_9) precursor와 O_2 가스를 사용하여 *p*-type Si(100)위에 PECVD 방법으로 형성하여 박막의 화학적, 물리적, 전기적, 기계적 특성 등을 조사하고 분석하였다. Si-O와 Si-O-C, Si-CH_3의 결합구조분석은 FTIR spectroscopy, XPS를 이용하였으며, 기계적 특성 hardness, elastic modulus를 조사하기 위해 nano-indentation 방법을 사용하였다. 두께 및 굴절률은 TEM, SEM, ellipsometer를 이용하였으며, SiOC(-H) 박막의 nano-pore 구조 분석을 위해 SANS, GISAXS, TEM을 이용하였고, 박막의 조성비와 밀도를 TOF-ERD를 이용하여 측정하였다. 전기적 특성은 Al/SiOC(-H) film/*p*-Si의 MIS 구조를 형성하여 C-V, I-V meter로 조사하였다. 200, 300, 400 ℃로 열처리 하여 nano-pore와 저유전 상수를 갖는 SiOC(-H) 박막의 열처리 전후의 화학적 구조 규명하였으며, 열처리 전후의 SiOC(-H) 박막의 기계적 전기적 특성과 유전상수의 특성 조사하였다.

본 연구에서 형성된 모든 SiOC(-H) 박막은 950~1250 cm^{-1} 영역에서 Si-O-Si(C), Si-CH_3, CH_x(x=1, 2, 3), OH related bonds를 전체적으로 관찰할 수 있었으며, 950~1250 cm^{-1} 영역의 Si-O-Si와 Si-O-C bonds를 분석하였을 때 ring, open그리고 cage Si-O-C bond로 나눌 수 있었다. 또한 700~950 cm^{-1} 영역에서 Si-O-Si, Si-C, Si-C, Si-CH_3, Si-O, Si-CH_x, SiOCH_3, H-Si-O bond가 관찰 되었다. 이렇게 형성된 SiOC(-H) 박막은 Si-O-Si networks에 -CH_3 groups

제주대학교 중앙도서관
JEJU NATIONAL UNIVERSITY LIBRARY

에 의해 Si-O-C 구조 형성하는데 CH_3 groups이 Si-O-Si networks을 깨고 형성된 상호간의 반발력으로 nano-pores가 형성하는 것으로 보인다. 또한 XPS 스펙트럼에서 Si 2p 궤도전자 스펙트럼을 통해 $Si-O_4$ bond, $C-Si-O_3$ bond를 확인 할 수 있었으며, 유량증가에 따라 더 많은 carbon과 hydrogen으로 인해 $Si-O_4$ bond 감소하고, $C-Si-O_3$ bond는 증가하였다. C 1s 전자궤도 스펙트럼에서는 C-H, C-Si 그리고 -C-O bonds가 관찰되었으며, Si-O links에 carbon 원자 함유되어 Si-O-C links 형성하였다. 이로서 carbon의 함량이 증가함에 따라 SiO_3C 구조를 형성하게 되고, oxygon의 전기 음성도 3.5보다 낮은 전기음성도 2.5를 갖는 carbon으로 인해 Si-O와 Si-O 사이의 반발력보다 Si-O와 Si-C 사이의 반발력이 더 커지게 되고 유전상수를 낮추는 효과가 있다. 또한 열처리 전후 박막의 구조적 변화는 open link가 ring link로 변함에 따라 박막내의 안정적인 pore를 형성하게 된다.

측정된 pore의 크기는 2.0±0.5 nm에 가장 많이 분포하였고, 평균 크기는 3 nm 이었다. SiOC(-H) 박막의 porosity 증가는 carbon의 함량 증가와 유전상수의 감소, Si-O-C ring link mode의 증가는 밀접한 관계 구조를 이루고 있다. SiOC(-H) 박막의 400 ℃ 열처리 전후 porosity는 R= 45 % 일 때 37~44.8 %, R= 85 % 일 때 46~49.7 % 이며, SiOC(-H) 박막의 R=45~85 % 열처리 전 박막의 밀도는 2.42~1.21 g/cm^3, R = 85 % 400 ℃열처리 후 박막의 밀도는 0.98 g/cm^3 이었다. 이는 박막내의 pore의 형성으로 박막의 density가 감소하는 것으로 보인다.

SiOC(-H) 박막의 기계적 특성 중 Hardness는 R=45~85 % 열처리 전 2.6~1.6 GPa, 400 ℃ 열처리 전후는 2.0~0.7 GPa의 값을 얻었다. 이는 carbon과 porosity가 증가하고, density가 감소함에 따라 modulus 감소하는 경향을 나타내었으며, TEOS-SiO_2 film의 8~10 GPa의 값보다는 현저히 작은 값을 보이지만, 유사한

제주대학교 중앙도서관
JEJU NATIONAL UNIVERSITY LIBRARY

porous 박막 SiLK 박막의 0.1~0.2 GPa, 그리고 MSQ-based 물질의porosity = 45~50 %에서의hardness 0.13~0.57 GPa에 비해 우수한 특성을 보였다. 또한 Elastic modulus도 SiOC(-H) 박막의 경우 R=45~85 % 열처리 전 26~14 GPa, 400 ℃ 열처리 후 20~7 GPa 이었으며, TEOS SiO_2 박막의 70~90 GPa 보다는 동일하게 낮았으나, SiLK 박막의 3~4 GPa, MSQ-based 물질의 porosity = 45~50 %일 때의 modulus 2 GPa 보다는 우수한 특성을 보였다. 이로서 SiOC(-H) 박막에 많은 alkyl groups이 열적 기계적 안정성을 높여주고, nano size-pore를 형성하여 유전상수 값을 낮춤을 알 수 있었다. 박막의 유전상수 특성을 조사하기 위해 C-V 방법 및 Ellipsometry를 이용한 굴절률 및 여러 공식을 통해 측정 및 계산하였다. 유량에 따른 bonding angle, dipole moment, 그리고 polarizability 계산에서 Si-O-C의 dipole moment는 유량과 열처리 온도가 증가할수록 감소하였으며, 400 ℃ 열처리 전후에 3.635×10^{-29} Cm의 값을 얻었고, dipolar polarizability는 유량과 열처리 온도가 증가할수록 $\sim10^{-40}$ Fm^2로 감소하였다. 유전상수 특성은 전자에 의한 유전상수가 가장 크게 영향을 미치며 이온에 의한 유전상수, 그리고 dipole에 의한 유전상수 순으로 그 영향력을 끼치고 있음을 확인할 수 있었다. 유전상수는 R=85 %에서 열처리 전 2.3, 400℃열처리 후 2.18의 값을 가졌으며, 굴절률은 R=45~85 % 일 때 열처리 전 1.50~1.37, 400℃ 열처리 후에는 1.4~1.3의 값을 얻었다.

이상의 연구를 통하여 차세대 ULSI 소자의 Cu/Low-k 층간 절연막으로 적용될 저유전 물질로 ICPCVD 방법에 의해 형성된 SiOC(-H) 박막에 대한 결합 및 결정구조와 박막의 기계적·전기적 특성 등의 다양한 연구를 통해 우수한 저유전 특성의 박막임을 보였다.

제주대학교 중앙도서관
JEJU NATIONAL UNIVERSITY LIBRARY

감사의 글

“사람이 마음으로 자기의 길을 계획할지라도 그 걸음을 인도하는 자는 여호와시니라.” - 잠언 16:9 -

저를 높이기도 하시고 낮추기도 하시는 여호와 하나님께 감사드립니다. 하나님은 낮음에서 겸손과 인내를 배우게 하시고 높이심의 때에 더욱 겸손함과 감사함으로 서게 하시어 변함없는 신실함으로 인도하십니다. 지난 8년이라는 긴 시간 중에 때때로 낮은 가운데 거하게 하시어 나의 모든 계획과 걸음을 멈춰 서서 하나님과 나 그리고 세상을 보게 하셨습니다. 철저히 혼자 서는 시간을 통해 많은 도움의 손길을 보여주시며 세상은 홀로 서되 혼자의 힘과 의지로 살아가는 것이 아님을 알게 하셨습니다. 감기도 잘 걸리지 않던 제가 가볍게 넘겼던 교통사고로 인해 3년 이상의 시간을 작고 큰 병으로 긴 고통과 함께 긴 침묵의 시간을 지나며 인생의 지각생이 되었지만 너무나 소중하고 귀한 것을 얻은듯합니다.

아버지와 같은 사랑으로 인자하시면서도 과학자의 치밀함과 섬세함으로 가르치며 이끌어주신 최치규 교수님께는 평생을 두고 갚아드려야 할 은혜가 너무 많은듯합니다. 이 논문을 꼼꼼히 살펴주시며 심사해주신 김두철 교수님, 이희우 교수님, 홍진표 교수님, 고정대 교수님, 그리고 많은 지도와 도움을 주신 한국과학기술원의 장홍영 교수님과 서울대학교 김형준 교수님께도 감사의 마음을 전합니다. 학부시절부터 지도와 격려로 이끌어주신 홍성락 교수님, 현남규 교수님, 김용주 교수님, 유영훈 교수님, 그리고 지금은 고인이 되신 오상식 교수님과 류재연 교수님께도 깊은 감사의 마음을 전합니다.

선배라는 든든한 의지와 힘이 되어주신 부성은 선배님과 많은 시간을 함께하며 많은 걸 가르쳐주셨던 강민성 선배님께 감사드립니다. 그간 연구하며 함께 우

제주대학교 중앙도서관

정과 열정을 같이하며 많은 도움을 주었던 호정, 유성, 창실, 두훈, 권삼, 태언, 그리고 이제 이 연구실을 멋지게 꾸려갈 든든한 후배 용준, 승현, 안수, 그리고 하나님이 붙여주셨던 우현에게도 고마운 마음을 전합니다.

기초과학 지원연구소, 한국 자원연구소, 한국 원자력 연구소, 한국 표준과학 연구소, 포항공대 가속기 연구팀과 한국과학기술원 플라즈마 연구실팀원들 모두에게 감사의 마음을 전합니다.

늘 기도해주심으로 힘이 되어주신 아름다운교회 이종한 목사님과 조숙 사모님, 힘들 때 마다 어깨를 도닥이시며 기도해 주신 권인숙 집사님, 황종임 집사님, 강성언 집사님, 주치의가 되어 치료해주신 이호근 집사님과 은선언니, 사랑으로 세상을 다시 보게 하신 최창호 목사님과 오성숙 사모님께 깊은 감사의 마음을 전합니다. 또 나의 사인방이자 삶의 동역자인 동현오빠, 정국이, 은주가 있어 외롭지 않았고, 나의 사랑하는 동생 경은, 나의 사랑하는 광석오빠와 올케 은정씨에게도 감사의 마음과 사랑을 전합니다.

많은 분들의 도움과 사랑이 있었기에 다시 일어설 수 있었고, 앞으로도 해쳐 나갈 수 있음에 진심으로 고개 숙여 감사를 표합니다. 많은 분들에게 걱정을 끼쳐드려 죄송하면서도 묵묵히 격려해주신 모든 분들께 한 분 한 분 다 말씀드리지 못할지라도 마음 깊이 감사함을 전합니다.

마지막으로, 안타까움과 조급함에도 드러내지 않으시고 사랑과 믿음으로 묵묵히 지켜봐주신 세상에서 가장 사랑하고 존경하는 어머니와 아버지께 깊이 감사드리며, 이 논문을 사랑하는 두 분께 드립니다.

2006년 1월 제주대학에서 **오경숙**

제주대학교 중앙도서관